Graphene Mechanical Resonators Coupled to Superconducting Microwave Cavities

Thesis by
Peter Weber

September 2016

Universitat Politècnica de Catalunya (UPC)
ICFO - The Institute of Photonic Sciences

Supervisor: Prof. Dr. Adrian Bachtold

Thesis committee:
Prof. Dr. Ignacio Wilson-Rae
Prof. Dr. Hugues de Riedmatten
Dr. Hans-Gregor Hübl

ICFO
The Institute of Photonic Sciences

UPC
UNIVERSITAT POLITÈCNICA DE CATALUNYA

Abstract

In recent years, mechanical resonators based on graphene have attracted considerable interest as nanoelectromechanical systems (NEMS). Graphene NEMSs allow for exceptional properties such as high mechanical strength, high frequencies and quality factors, tunable mechanical properties, and ultra-low mass. As a consequence, these systems are promising to investigate motion in the quantum regime, probe rich nonlinear phenomena, sense minuscule masses and forces, and study surface science.

However, a central challenge in graphene NEMS research is the coupling of the mechanical vibrations to external systems for efficient read out and manipulation. In this dissertation, we report on a novel approach, in which we employ a cavity optomechanical scheme to investigate few-layer and multilayer graphene mechanical resonators at cryogenic temperatures ($T = 15\,\mathrm{mK}$). The capacitive coupling between graphene mechanical systems and the microwave photons of a superconducting microwave cavity allows for investigation of the mechanical properties with unprecedented accuracy and control.

In a first experiment, the coupling of circular, high-Q graphene mechanical resonators ($Q_\mathrm{m} \sim 10^5$) to a nearby cavity counter electrode results in a single-photon optomechanical coupling of $\sim 10\,\mathrm{Hz}$. The initial devices exhibit electrostatic tunability of the graphene equilibrium position, strong tunability of the mechanical resonance frequency, and the possibility to control the sign and magnitude of the observed Duffing nonlinearity. Compared to optomechanical systems fabricated from bulk materials, the strong tunability of the mechanical properties of graphene NEMS is unique.

In a second experiment, we quantitatively investigate the sideband cooling and force sensing performance of multilayer graphene optomechanical systems. The strong coupling to the microwave photons allows to achieve a mechanical displacement sensitivity of $1.3\,\mathrm{fm\,Hz^{-1/2}}$ and to cool the mechanical motion to an average phonon occupation of 7.2. In terms of force sensing performance, we find that the force sensitivity is limited by the imprecision in the measurement of the vibrations, the fluctuations of the mechanical resonant frequency, and the heating induced by the measurement. Our best force sensitivity, $390\,\mathrm{zN\,Hz^{-1/2}}$, is achieved by balancing measurement imprecision, optomechanical damping, and Joule heating. These results hold promise for studying the quantum capacitance of graphene, its magnetization, and the electron and nuclear spins of molecules adsorbed on its surface.

In a third experiment, we implement energy decay measurements to study mechanical dissipation processes in multilayer graphene mechanical resonators. We study the energy decay in two regimes. In the low-amplitude regime, the mechanical quality factor surpasses $Q_\mathrm{m} = 10^6$. This quality factor is larger than that obtained with spectral measurements, because energy decay measurements are immune from dephasing. In the

high-amplitude regime, the motion of atomically-thin mechanical resonators is radically different from what has been observed in other resonators thus far. Instead of a smooth exponential decay, energy decays discontinuously, that is, the dissipation rate increases step like above a certain threshold amplitude. We attribute these phenomena to nonlinear decay processes. These findings offer new opportunities for manipulating vibrational states.

Abstracto

Durante los últimos años resonadores mecánicos basados en grafeno han atraído un considerable interés cómo sistemas nanoelectromecánicos (NEMS). Los NEMS de grafeno permiten excepcionales propiedades como una gran estabilidad mecánica, altas frecuencias de resonancia y factores de calidad, propiedades mecánicas ajustables y masas muy pequeñas. Como consecuencia, estos sistemas son buenos candidatos para investigar el movimiento mecánico en el régimen cuántico, indagar varios fenómenos no lineales, medir minúsculas masas o fuerzas y estudiar los efectos de superficie.

Sin embargo, el mayor reto en la investigación de los NEMS de grafeno es el acoplamiento de las vibraciones mecánicas con sistemas externos con el objetivo de hacer una manipulación y lectura eficiente. En esta tesis, presentamos un nuevo enfoque en el cuál aprovechamos la interacción de la presión de radiación optomecánica para investigar resonadores mecánicos de grafeno compuesto de pocas capas y multicapas en temperaturas criogénicas ($T = 15\,\mathrm{mK}$). El acoplamiento capacitivo entre el sistema mecánico de grafeno y los fotones de microondas de una cavidad superconductora permite la investigación de las propiedades mecánicas con una precisión y control sin precedentes.

En un primer experimento el acoplamiento de un resonador circular de grafeno con un alto factor Q con un electrodo de la cavidad da como resultado un gran acoplamiento optomecánico de 10 Hz. Los dispositivos iniciales muestran un ajustamiento electrostático de la posición de equilibrio del grafeno, una fuerte variabilidad de la frecuencia de resonancia mecánica y la posibilidad de controlar el signo y magnitud de la no linearidad de tipo Duffing. Comparado con otros sistemas optomecánicos fabricados de materiales bulk, la gran variabilidad de las propiedades mecánicas son únicas en los NEMS de grafeno.

En un segundo experimento investigamos cuantitativamente el enfriamiento fuera de banda y sensibilidad de fuerzas usando un sistema optomecánico basado en grafeno multicapa. El fuerte acoplamiento a los fotones de microondas nos permite conseguir una sensibilidad del desplazamiento mecánico de $1.3\,\mathrm{fm\ Hz^{-1/2}}$ y también enfriar el movimiento mecánico hasta una ocupación media de 7.2 fonones. En términos de sensor de fuerzas, encontramos que la sensibilidad de fuerzas está limitada por la imprecisión en la medida de las vibraciones, las fluctuaciones de la frecuencia de resonancia mecánica y en el calentamiento inducido por la medida. Nuestra mejor sensibilidad de fuerzas $390\,\mathrm{zN\ Hz^{-1/2}}$ se consigue ajustando la imprecisión de la medida, el decaimiento optomecánico y el calentamiento Joule. Estos resultados son prometedores para el estudio de las capacidades cuánticas del grafeno, su magnetización y los espines nucleares y electrónicos de moléculas adsorbidas en la superficie del grafeno.

En un tercer experimento implementamos medidas del decaimiento de energía para estudiar los procesos de disipación mecánica en resonadores de grafeno en multicapas.

Estudiamos el decaimiento energético en dos regímenes. El primero, a baja amplitud de movimiento donde el factor de calidad sobrepasa $Q = 10^6$. Este factor de calidad es mayor que el obtenido con medidas espectrales, porque las medidas del decaimiento energético son inmunes al desfase. En el segundo régimen, a altas amplitudes, el movimiento de los resonadores que son solo de un átomo de grosor es radicalmente diferente de lo que se ha observado en otros resonadores hasta ahora. En lugar de un decaimiento exponencial, la energía se disipa discontinuamente, es decir, el ratio de disipación aumenta por pasos sobre un cierto límite de amplitud. Atribuimos este fenómeno a procesos de decaimiento no lineales. Estos descubrimientos ofrecen nuevas oportunidades en la manipulación de estados vibracionales.

Acknowledgements

First, I want to thank **Ignacio Wilson-Rae**, **Hugues de Riedmatten** and **Hans Gregor Hübl** to serve as experts in my thesis committee and as well **Maria Jose Esplandiu** and **Romain Quidant** for agreeing to serve as substitute members.

This PhD Thesis would not have been possible without the effort and encouragement of many people, to whom I am very grateful.

I would like to thank my thesis advisor **Adrian Bachtold** to give me the opportunity to pursue a PhD on optomechanics in his group. He gave me the amazing possibility to be part of a team that successfully designed and developed a sophisticated experiment from scratch and he provided me with the necessary support and enthusiasm. His scientific instinct and close guidance were indispensable to my doctoral studies.

I want to thank **Johannes Güttinger** with whom I closely worked together for about 4 years of my PhD. His guidance and motivation have immensely contributed to my professional development and his optimism and positive attitude have, moreover, made it possible to overcome difficult moments and setbacks in the lab. I am grateful both to **Adrian** and **Johannes** for always having had an open ear and time to discuss approaches and difficulties, which was key to the results we have achieved.

I am also thankful to **Adrien Noury**, who joined the team during a very stressful period. He was an enrichment to the team and he immensely helped in conducting the experiment and in the data analysis process.

Further, I enjoyed the time working with the highly motivated master/semester students **Santiago Cartamil, Camille Lagoin and Jorge Vergara** on our common project. I also acknowledge **Ioannis Tsioutsios**, **Kevin Schädler**, **Joel Moser**, **Maria Jose Esplandiu**, **Johann Osmond**, **Luis Enrique**, **Alexander Eichler**, **Alexandros Tavernarakis**, **Antoine Reserbat**, **Mark Dykman** and **Pierre Verlot** for experimental support and/or fruitful discussions. I thank the PhD students **Ioannis Tsioutsios**, **Nicolas Morell**, **Sergio de Bonis**, **Jil Schwender** and **Jorge Vergara** for the relaxed, fun and youth atmosphere they have created in the lab. I also thank past and current members of the group **Simon Hurand**, **Marianna Sledzinska** and **Ali Afshar** for having created a nice, social environment.

I want to thank **Gabriel Puebla**, **Christopher Eichler**, **Andreas Isacsson**, **Martin Eriksson**, **Sara Hellmüller** and **Andreas Wallraff** for helpful discussions. I also acknowledge **Gustavo Ceballos** and the ICFO mechanical and electronic workshop for support.

I gratefully acknowledge funding from the European Union through the RODIN-FP7 project, the ERC starting grant 279278 (CarbonNEMS) and the Graphene Flagship (grant agreement 604391). I acknowledge the Spanish state (MAT2012-31338), the Catalan

government (AGAUR, SGR), MINECO and the Fondo Europeo de Desarrollo Regional (FEDER) through grant MAT2012-31338, the Fundació Privada Cellex, and the Severo Ochoa Excellence Grant.

Contents

Chapter 1

Introduction

1.1 Plenty of room at the bottom

This quote is the title of a talk of Richard Feynman, in which he first envisioned nanotechnology more than 50 years ago [1]. Nowadays, nanotechnology encompasses many different areas of science and technology that share one common definition: understanding, controlling, and manipulating matter on length scales down to the nanoscale. With technologies like the scanning tunneling microscope, the atomic force microscope (AFM), and the scanning electron microscope imaging single atoms or molecules is day-to-day business in many laboratories around the world. Manipulation of matter on molecular length scales also became a standard discipline involving technologies like electron-beam and ion-beam lithography, atomic-layer deposition, and molecular-beam epitaxy. With this improved level of control, almost every major field of science employs and exploits nanotechnology in order to fit functional and more complex structures into smaller and smaller spaces. The key example of this miniaturization process is the computer chip. Due to steady improvement of fabrication capabilities, the predictions of Moore's law [2] have prevailed for over 40 years leading to computer chips with billions of transistors on spaces as small as a few millimeters (see Fig. 1.1(a)).

Nanoelectronics is certainly the field of nanotechnology that had the largest impact on human lives and on world economy. The ability to produce smaller, faster and cheaper devices came along with the possibility to gather, store and process information in cheaper and more efficient ways. The results of this revolution of information technology are concepts like the 'Internet of things' or 'Big data', which most likely will govern the world economy for the next decade. Another important outcome of recent technological developments are sensing applications such as 'Robotics' and 'Analytics' (biology/medicine). The successful realization of these concepts and applications require a huge diversity of different sensors that may detect any type of information on humans or their environment, devices with better energy efficiency, faster computers, and higher data transmission rates. Holding up with the constant desire for higher performance and more functionality, however, requires new device concepts pushing existing boundaries. In this sense, integrating nanoscale devices not only with electronic, but also with optical (nanophotonics) or mechanical (nanomechanics) functionality is a promising route to go (see Fig. 1.1(b,c)).

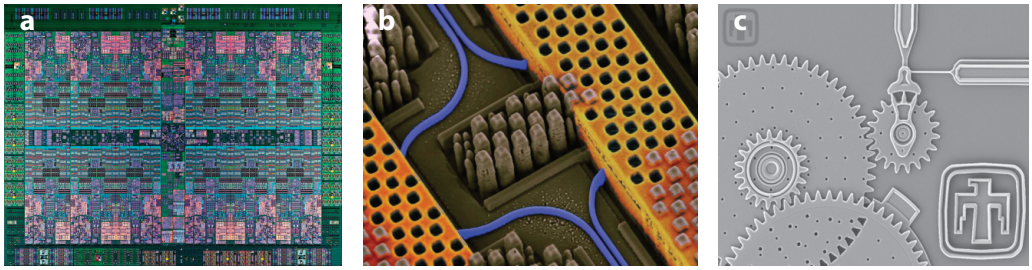

Figure 1.1: **Example devices from different fields of nanotechnology.** (**a**) IBM Power8 processor. The chip consists of 4.5 billion transistors on an area of 650 mm^2. (**b**) Scanning electron micrograph of IBM chip that transmits high-speed optical signals using waveguides (blue) and high-speed electrical signals utlizing copper wires (orange). (**c**) NEMS device of Sandia National Laboratories for multiple gear speed reduction. Panel is adapted from [3]

1.2 Nanoelectromechanical systems

The field of nanomechanics studies the mechanical properties of nanoelectromechanical systems, which have emerged as the natural miniaturization step from microelectromechanical systems (MEMS). These systems feature a broad range of applications in commercial technologies. They are found in gyroscopes or as acceleration sensors in mobile phones and car airbags. In research applications, NEMS become faster and they show extraordinary sensitivity to external forces [4] as they shrink to even smaller dimensions, the AFM being a key application of NEMS. The increased sensitivities allow for single-electron spin detection [5] (Fig. 1.2(a)), and for single-molecule spectroscopy [6] (Fig. 1.2(b,c)), both with applications in medical, biological, and chemical research. Furthermore, the increased frequencies and the possibility to efficiently couple NEMS to quantum systems make them promising candidates for future quantum information processing [7].

Nanoelectromechanical systems are fabricated using either the top-down or the bottom-up approach. The traditional, the top-down approach, is based on lithographic processes to pattern bulk materials into the desired nanoscale structures. While this allows for high control during fabrication and is easily compatible with wafer-scale integration, lithographic processes are reaching their resolution limit. Below a certain size non-crystalline surfaces begin to dominate the material properties. One important figure of merit of NEMS, the mechanical quality factor, in particular, suffers from losses attributed to fabrication induced surface defects [8].

The bottom-up approach utilizes intrinsically nanoscale materials, or molecular self assembly of nanostructures, followed by subsequent integration into functional circuits. This approach allows for the fabrication of smaller and potentially defect-free nanodevices as compared to the top-down approach, which comes at the cost of reduced control over the fabrication process. The carbon allotropes, graphene and carbon nanotubes, are particularly interesting candidates for the integration in NEMS devices. While carbon nanotubes represent the ultimate down scaling limit for NEMS devices, graphene promises to combine the advantages of top-down and bottom-up devices. It is intrinsically nanoscale, but can be grown over large areas [9] and patterned at the wafer scale by lithographic processes.

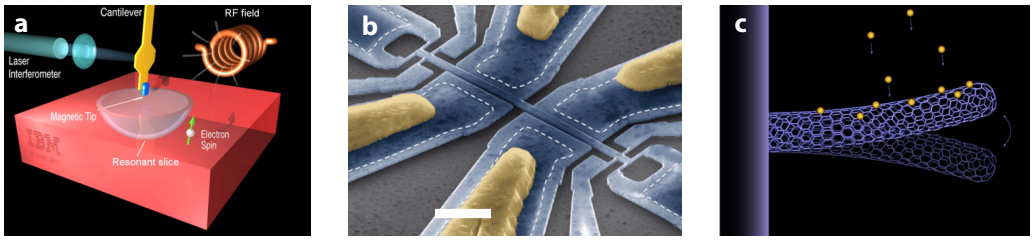

Figure 1.2: **Example devices for mass and spin detection.** (**a**) Magnetic resonance force microscopy of a single electron spin with a NEMS cantilever containing a magnetic tip [5]. (**b**) NEMS-based mass spectrometer with single-molecule resolution [6]. This device is a typical example of the top-down approach. (**c**) An atomic resolution mass sensor consisting of a carbon nanotube [10]. This is an example of a bottom-up device.

1.3 The rise of graphene

Graphene is a two-dimensional, atomic-scale, material with exceptional electronic, mechanical and optical properties [11], which make it suitable for a number of interesting applications. Graphene is regarded as a promising material for high-frequency electronics with working frequencies well above 100 GHz [12] (Fig. 1.3(b)), which stems from its high charge carrier mobilities [13]. Being an excellent conductor but at the same time almost transparent with a wavelength independent light absorption of 2.3% [14], graphene brings transparent electrodes within reach [15]. In optoelectronics, graphene may play a decisive role in next generation photo detectors, in particular, when combined in hybrid devices with other nanoscale materials [16, 17] (Fig. 1.3(a)). Graphene's enormous mechanical strength with a Young's modulus of 1 TPa [18] combined with its ultimately low mass-density portrait graphene as the ideal material for nanoelectromechanical systems both in basic research and in ultra-sensitive mass [19] and force sensing applications [20] (Fig. 1.3(c)).

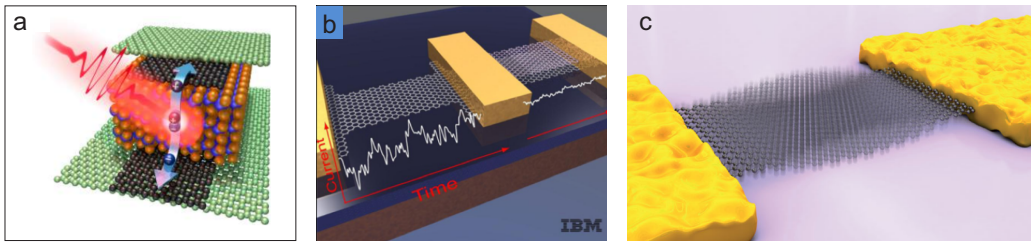

Figure 1.3: **Artistic images of different realizations of graphene devices.** (**a**) Photodetector made of graphene/WSe_2/graphene heterostructures [17]. (**b**) Graphene transistors consisting of single-layer and bilayer graphene [21]. (**c**) Doubly-clamped single-layer graphene mechanical resonator [22].

In recent years, graphene NEMS have demonstrated several interesting properties including mechanical frequencies as high as hundreds of MHz [23], extreme frequency tunability [24], high mechanical quality factors [22] and nonlinear mechanical dissipation [22]. However, the enhanced sensitivity to external perturbations poses difficulties

to study the intrinsic mechanical properties, without perturbing the fragile mechanical state. Therefore, one of the central challenges in graphene NEMS research has been the efficient coupling of the vibrations to external systems in order to transduce the motion into a detectable electrical [24, 25, 26, 22, 23] or optical [27, 25] output signal. Optical transduction utilizes a laser beam that forms a standing wave pattern perpendicular to the suspended graphene membrane. The laser is reflected off from the substrate underneath the graphene, such that the displacement of the graphene modifies the optical absorption. The intensity modulation of the reflected beam encodes the mechanical motion. This technique has been successfully used to gain first photo-thermal control of the graphene vibrations [28]. In electrical transduction schemes, the graphene vibrations are capacitively actuated, and detected by exploiting the dependence of the conductance on applied gate voltage [29]. While this method has been widely applied to low-dimensional materials and is very powerful for carbon nanotubes [30], in general, it has limited capabilities in detecting and controlling mechanical motion. For instance, detection of graphene thermal vibrations has not been accomplished. In the context of larger mechanical systems, the field of optomechanics introduces yet another, very powerful, concept: detection of mechanical motion by parametric coupling of the vibrations to the electromagnetic field of a high-Q cavity resonance.

1.4 Introduction to optomechanics

In the last decades, the field of optomechanics has gained considerable popularity due to the versatility of its potential applications ranging from metrology experiments such as gravitational wave detection to quantum information processing and tests of quantum theory on macroscopic objects. In the optical frequency range the canonical optomechanical system consists of a Fabry-perot cavity with a mechanically compliant mirror [31, 32] (Fig. 1.4(b)). In the microwave frequency range it is an inductor-capacitor (LC) cavity with a mechanically movable capacitor plate [33, 34, 35, 36, 37, 38, 39] (Fig. 1.4(a)). The mechanical element dispersively interacts with the cavity field i.e. the cavity resonance frequency depends on the mechanical displacement. The generality of this parametrical interaction has led to a variety of different realizations of optomechanical systems. Among many others, these include microtoroid resonators that support whispering gallery modes along with circular optical modes [40], photonic crystals that allow for the coexistence of photonic and phononic modes [41], and dielectric objects inside an optical cavity. The dielectric object can be a thin membrane [42], a nanoparticle [43], or an atomic cloud [44].

The dispersive optomechanical interaction has two main purposes. First, it is used to ultra-sensitively monitor the mechanical position through interferometric detection techniques [34]. As these systems approach better sensitivities, the uncertainty in the position readout is fundamentally limited by the Heisenberg uncertainty principle [46, 47, 48]. Squeezing of the mechanical motion allows to circumvent these limits [49], which has been applied in large-scale optomechanical experiments for gravitational wave detection [50] and mechanical quantum state squeezing [51, 49, 52]. Second, the optomechanical interaction allows for the control and manipulation of the mechanical eigenstate through a retardation force of the electromagnetic field. Important milestones building upon this property are cooling of mechanical motion [33, 36, 40] eventually leading to the quantum ground state [38, 41], quantum state transfer [53], generation of non-

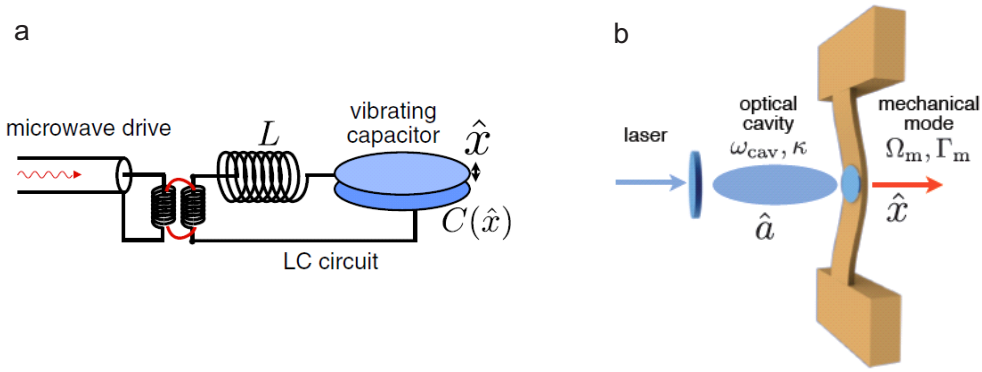

Figure 1.4: **Schematics of cavity optomechanics systems.** (**a**) Microwave optomechanical device consisting of an LC-cavity with a mechanically movable capacitor plate. The mechanical motion modulates the cavity frequency by changing its total capacitance. (**b**) Optical fabry-perot cavity with one mechanically compliant end-mirror. The mechanical motion modulates the cavity frequency by modifying its length. Panel is adapted from [45].

classical states [54, 55], microwave amplification [37], and conversion of microwave to optical light [56, 57].

1.5 Thesis motivation and outline

In this dissertation, we establish optomechanical readout and control of the motion of few-layer graphene mechanical systems by integration into a microwave cavity optomechanics scheme. The low mass density and the two-dimensional nature of graphene are promising for strong capacitive coupling. By implementing this detection scheme we pursue two main goals. First, we want to study mechanical motion of atomically thin membranes and, second, we want to benchmark graphene optomechanical systems. The outline of the thesis is the following:

- Chapter 2 provides a basic introduction of the electronic and mechanical properties of single-layer and few-layer graphene.
- Chapter 3 introduces the linear and nonlinear harmonic oscillator. It further provides a model to quantitatively describe the mechanical properties of circular graphene mechanical resonators under tension.
- Chapter 4 discusses the modeling of the microwave cavities and introduces the optomechanical interaction.
- Chapter 5 describes the fabrication of both the cavities and the suspended graphene mechanical resonators.
- Chapter 6 discusses the first implementation of few-layer graphene mechanical resonators with a superconducting microwave cavity.

- Chapter 7 studies the radiation pressure cooling and force sensing performance of multilayer graphene resonators coupled to microwave cavities.
- Chapter 8 describes the implementation of an energy decay setup to study mechanical dissipation in multilayer graphene mechanical systems.

Chapter 2

Graphene

In this chapter, we will give a brief introduction of the basic properties of graphene. Taking its crystallographic structure as the starting point we introduce the peculiar electronic band structure followed by the mechanical properties of single-layer and multi-layer graphene.

2.1 The structure of graphene

The discovery of graphene in 2004 by the scientists Andre Geim and Konstantin Novoselov has triggered an enormous wave of research activities in graphene [11] and other two-dimensional (2D) materials, and was rewarded by the Nobel prize in 2010. Despite the belief of the scientific community that strictly 2D crystals were thermodynamically unstable [58], the researchers from Manchester were able to isolate free standing graphene by a simple mechanical cleavage technique [59]. In their first experiments they confirmed the exceptionally high crystalline and electronic quality of graphene, which has been known for over 60 years from theoretical studies in graphite [60].

Graphene is a two-dimensional sheet of carbon atoms arranged in a hexagonal lattice and is the central component of most carbon allotropes (see Fig. 2.1). The remarkable electronic, mechanical, thermal and optical properties of graphene find their origin in the electronic structure of the carbon atom [61]. Carbon has four energetically similar valence electrons occupying the 2s, $2p_x$, $2p_y$ and $2p_z$ orbitals. In the graphene lattice, each carbon atom forms 3 in-plane covalent bonds with its neighboring atom by sp2 hybridization of the 2s, $2p_x$ and $2p_y$ orbitals. The bond length is 1.42 Å and its angular spacing 120°. These covalent bonds form the so-called σ-bands, which give graphene its enormous mechanical strength. The remaining $2p_z$ orbital of each atom is orthogonal to the lattice plane and forms the electronic π-bands of the crystal. When stacking sheets of graphene on top of each other one obtains graphite with an interlayer spacing of 3.35 Å. In graphite, the π orbitals between different graphene layers interact via the van-der-Waals interaction. The resulting interlayer coupling is weak.

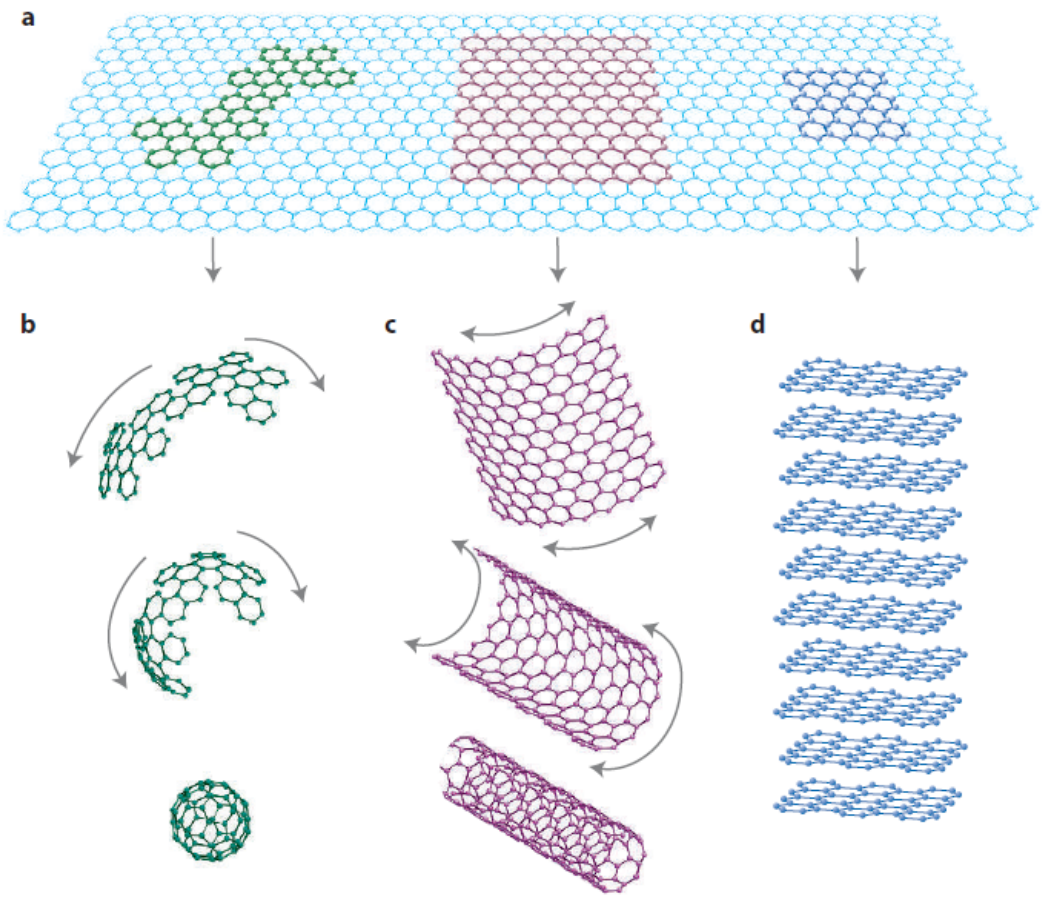

Figure 2.1: **Carbon allotropes of different dimensionality**. (**a**) The 2D graphene lattice is the central building block of several carbon allotropes including 0D buckyballs **b**, 1D carbon nanotubes **c**, and 3D graphite **d**. Panel is adapted from [11].

2.2 Electronic properties of graphene

The first decade of graphene research was marked by an enormous interest in the peculiar electronic properties of graphene, which arise from the crystallographic symmetries of its lattice. The real space and the corresponding reciprocal space lattice of graphene exhibit a hexagonal structure sketched in Figs. 2.2(a) and (b), respectively. In order to fulfill the translational properties of a Bravais lattice with the unit vectors $\vec{a}_1$ and $\vec{a}_2$, graphene has a two atomic basis A and B. This translates into two inequivalent high symmetry points K and K' on the corners of the first Brillouin zone in reciprocal space. While the electrons comprising the σ-bands are strongly bound and therefore have a large energy separation between valence and conduction band, the π-bands form a delocalized electron system that is relevant for electron transport. The low energy band structure is illustrated in Fig. 2.2(c). The valence and the conduction band touch each other at the charge neutrality point, the so called Dirac points K and K', making graphene a zero

band gap semi-conductor.

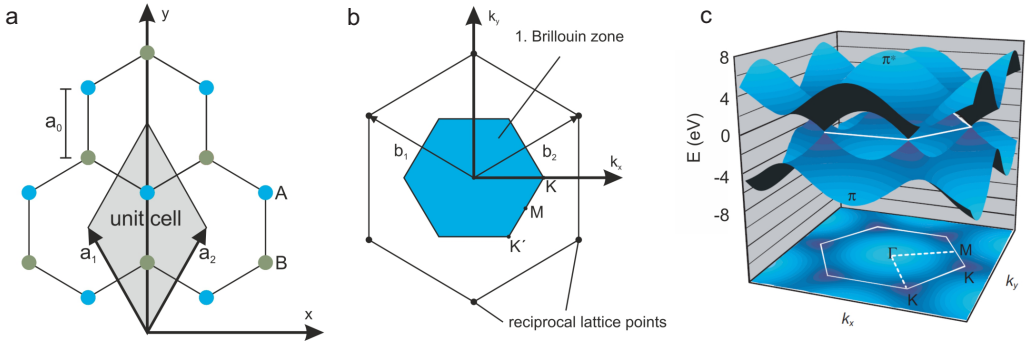

Figure 2.2: **Graphene lattice and electronic band structure**. (**a**) Hexagonal real space lattice of graphene with the two sublattices A and B. The unit cell is formed by the unit vectors $\vec{a_1}$ and $\vec{a_2}$ while the distance between adjacent carbon atoms is a_0. (**b**) Corresponding lattice in reciprocal space with the unit vectors b_1 and b_2. The two inequivalent high symmetry points K and K' located on the corners of the first Brillouin zone are the regions important for transport. (**c**) Low energy band structure of graphene. The bonding π and the antibonding π^*-band touch each other at the corners of the first Brillouin zone, where the fermi energy is zero. Panels **a** and **b** are adapted from [62] and **c** from [63]

As early as in 1947 Wallace calculated the low energy band structure of graphene in a nearest neighbor tight-binding approximation of linear combinations of the $2p_z$-orbitals [60]. Close to the Fermi energy, his calculations yield a linear dispersion relation

$$E(\vec{\kappa}) = \hbar v_F |\vec{\kappa}| \tag{2.1}$$

with a cone like structure at the degeneracy points K, K' where $v_F \approx 10^6\,\mathrm{m/s}$ is the constant Fermi velocity and $\vec{\kappa} = \vec{k} - \vec{K}^{(')}$. An important implication of the linear dispersion relation is the fact that charge carriers in graphene behave like massless Dirac fermions. Further, graphene features high mobilities (up to $10^6\,\mathrm{cm}^2/\mathrm{Vs}$) and ballistic transport at low temperatures over length scales up to $28\,\mu\mathrm{m}$ [13, 64].

When increasing the number of graphene layers the dispersion relation transforms progressively into the semi-metal like dispersion relation of graphite [65]. While bilayer graphene already has a parabolic band dispersion around the K, K' points and a small band overlap on the order of $\approx 1\,\mathrm{mV}$, all consecutively added layers increase the band overlap. For >11 layers the difference to bulk graphite accounts for less than 10%.

2.3 Mechanical properties of graphene

The in-plane strength and the low mass density of graphene establish it as an excellent material for nanoelectromechanical systems [27]. The two-dimensional mass density is

$$\rho_{\mathrm{graphene}} = 7.6 \times 10^{-19}\,\mathrm{kg}/\mu\mathrm{m}^2. \tag{2.2}$$

Graphene is the stiffest material ever measured with a 2D in-plane Young's modulus of $E^{2\mathrm{D}} = 340\,\mathrm{N/m}$. In graphene, the Young's modulus is a 2D material property that relates

in-plane stress σ with in-plane strain ϵ

$$\sigma = E^{2D} \cdot \epsilon. \tag{2.3}$$

The Young's modulus of graphene was first measured in suspended graphene structures by nanoindentation with an AFM [18] and by using graphene as an impermeable membrane for gases [66], respectively. Similar results were obtained by utilizing a scanning electron microscope to monitor the out-of-plane displacement of suspended few-layer graphene sheets subject to an electrostatic force [67]. In order to compare single-layer graphene with multi-layer graphene or bulk graphite, the 2D Young's modulus is divided by the interlayer spacing of graphite leading to $E = 1\,\mathrm{TPa}$. Nanoindentation experiments also revealed that suspended graphene membranes are prestrained with an intrinsic breaking stress of $\sigma_{\mathrm{int}} = 42\,\mathrm{N/m}$ and a maximum strain of $\epsilon_{\mathrm{int}} = 25\%$. These properties lead to a number of interesting consequences when implementing NEMS based on graphene.

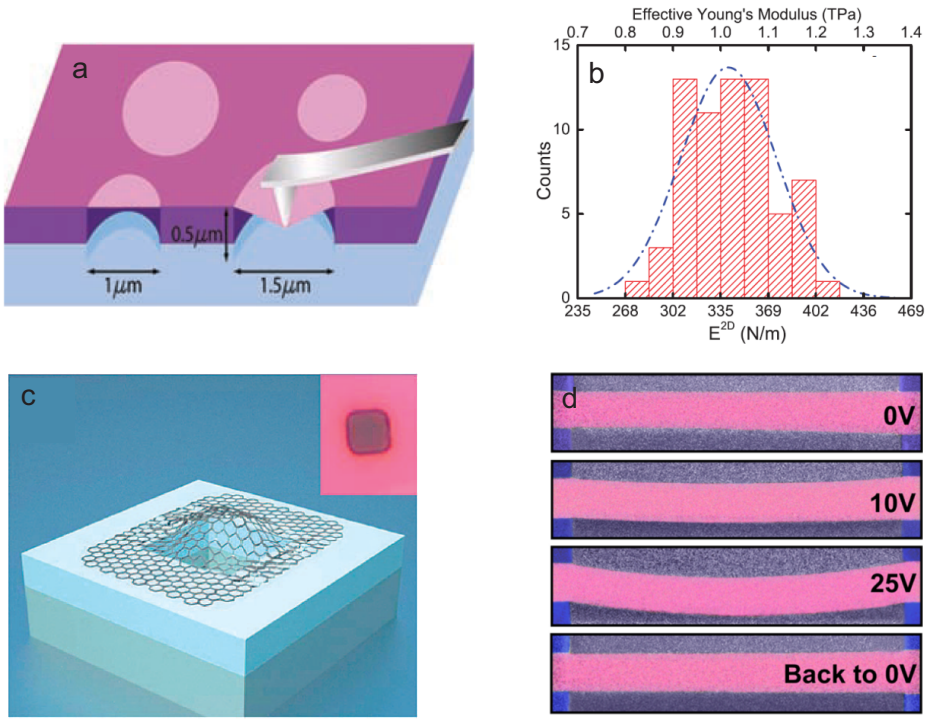

Figure 2.3: **Mechanical properties of graphene.** (**a**) Nanoindentation experiment using a diamond AFM tip to determine intrinsic mechanical properties of graphene [18]. (**b**) Effective Young's modulus of graphene [18]. (**c**) Impermeable graphene membrane used as an atomically thin balloon [66]. (**d**) Scanning electron microscope experiment of doubly-clamped suspended graphene membranes [67]. Here an electrostatic force is applied to study the out-of-plane static deflection.

The intrinsic resonance frequency of graphene mechanical resonators is determined mainly by the tension of the membrane. This is a consequence of the negligible bending rigidity and the prestrain usually found in suspended graphene membranes [27, 18, 68, 22].

The bending rigidity is defined as the amount of energy per unit area that is needed to curve an object [69]. It was shown that even for multi-layer graphene, for given displacements, the energy associated to bending is much smaller than the one associated to stretching [70]. Additionally, graphene can achieve high resonance frequencies that can be tuned by an externally applied force [24, 71]. This makes graphene interesting for a variety of radio-frequency applications [72, 73, 74, 75].

Chapter 3

Nanomechanics

In this chapter, we develop the theory that is necessary to understand the mechanical properties of circular graphene mechanical resonators. We start with the simplest model of the linear harmonic oscillator, followed by modeling of the nonlinear vibrations. In the second part, we derive the formalism of a membrane under tension subject to a static electric field.

3.1 Linear and nonlinear mechanical resonators

3.1.1 The harmonic oscillator with coherent driving

The simplest model that captures the motion of a wide variety of mechanically resonating systems, with arbitrary size and geometry, is the damped harmonic oscillator. A harmonically oscillating system is described by a linear relation between restoring force and displacement. The two important quantities characterizing such a system are the mechanical resonance frequency $f_\mathrm{m} = \omega_\mathrm{m}/2\pi$, where ω_m is the angular frequency, and the quality factor Q_m of the vibration. The mechanical resonance frequency is determined by the elastic properties, the mass, and the boundary conditions of the respective system. The harmonic oscillator is damped by its interaction with the environment and this damping can be characterized by the quality factor. The quality factor is defined as the ratio of the total energy to the energy lost per oscillation cycle

$$Q_\mathrm{m} = 2\pi \frac{E_\mathrm{total}}{\Delta E_\mathrm{cycle}}. \tag{3.1}$$

The equation of motion of the coherently driven damped harmonic oscillator is given by

$$m_\mathrm{eff}\ddot{z}(t) + m_\mathrm{eff}\Gamma_\mathrm{m}\dot{z}(t) + kz(t) = F_\mathrm{d}(t) \tag{3.2}$$

where m_eff is the effective mass, Γ_m the linear damping rate, and k the mechanical spring constant. Assuming a weak sinusoidal drive $F_\mathrm{d}(t) = F_\mathrm{d} \cdot \exp[i\omega_\mathrm{d}t]$, the equation can be solved with the ansatz $z(t) = z_0 \cdot \exp[i(\omega_\mathrm{d}t + \phi)]$ where ϕ is the phase difference between the mechanical motion and the drive. The amplitude as well as the phase response to an

external force depend on the driving frequency

$$z(\omega_{\mathrm{d}}) = \frac{F_{\mathrm{d}}}{m_{\mathrm{eff}}} \frac{1}{\sqrt{(\omega_{\mathrm{m}}^2 - \omega_{\mathrm{d}}^2)^2 + (\Gamma_{\mathrm{m}}\omega_{\mathrm{d}})^2}}. \tag{3.3}$$

$$\phi(\omega_{\mathrm{d}}) = arctan\left(\frac{\Gamma_{\mathrm{m}}\omega_{\mathrm{d}}}{\omega_{\mathrm{m}}^2 - \omega_{\mathrm{d}}^2}\right) \tag{3.4}$$

with

$$\omega_{\mathrm{m}} = \sqrt{\frac{k}{m_{\mathrm{eff}}}} \tag{3.5}$$

the mechanical resonance frequency, in the small damping limit $\Gamma_{\mathrm{m}} << \omega_{\mathrm{m}}$. We plot Eqs. 3.3 and 3.4 in Fig. 3.1. The amplitude response has a maximum at $\omega_{\mathrm{d}} \approx \omega_{\mathrm{m}}$. At this point the mechanical motion and the drive acquire a phase difference of $\phi(\omega_{\mathrm{m}}) = \pi/2$. Importantly, the quality factor simplifies to

$$Q_{\mathrm{m}} = \frac{\omega_{\mathrm{m}}}{\Gamma_{\mathrm{m}}}. \tag{3.6}$$

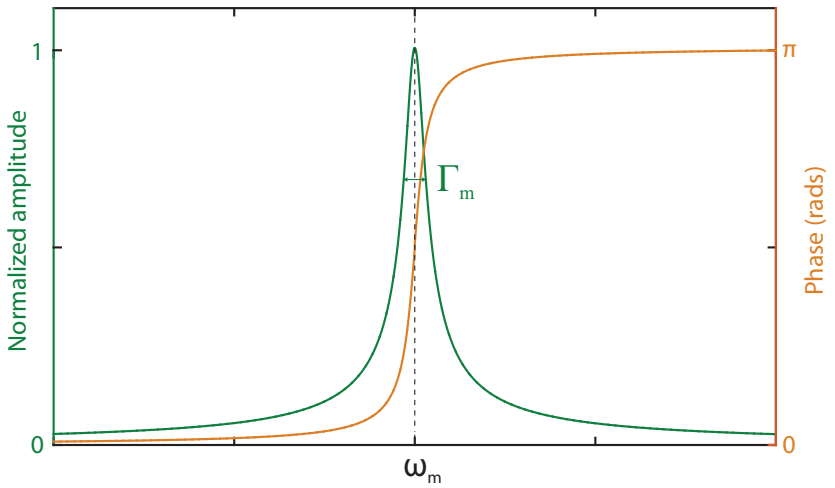

Figure 3.1: **Amplitude and phase response.** Response as a function of drive frequency of the coherently driven, damped, harmonic oscillator. Note that the mechanical dissipation is given by the line width of the spectrum at the point where the squared normalized amplitude equals 1/2. Panel is adapted from [3].

3.1.2 The harmonic oscillator with incoherent driving

The coupling to the thermal bath of the mechanical resonator leads to dissipation of mechanical energy quantified by the mechanical quality factor. However, the coupling also leads to statistical random driving of the resonator with a fluctuating force $\delta F(t)$. This is quantified by the fluctuation-dissipation theorem [76], which relates the fluctuations

of a physical system in thermal equilibrium to the response of the system to external perturbations. To derive the mechanical response to thermal noise, we rewrite the Fourier transform of Eq. 3.2 in frequency space

$$z(\omega) = \chi(\omega) \cdot \delta F(\omega) \tag{3.7}$$

in terms of the mechanical susceptibility

$$\chi(\omega) = \frac{1}{m_{\mathrm{eff}}(\omega_{\mathrm{m}}^2 - \omega^2 - i\Gamma_{\mathrm{m}}\omega)}. \tag{3.8}$$

In contrast to coherent driving, the mechanical energy for a noise driven spectrum is distributed over a frequency window that depends on the mechanical line width. This requires a different approach to get access to the mechanical susceptibility. Experimentally one records the power spectral density (PSD) $S_{aa}(\omega)$ of a signal $a(t)$, which can be related to the mechanical trajectory $z(t)$. This conversion depends on the experimental transduction scheme. We introduce the autocorrelation function of $a(t)$

$$C_{\mathrm{a}}(\tau) = \langle a(t)a^*(t+\tau)\rangle\,. \tag{3.9}$$

Here $\langle ...\rangle$ denotes the statistical average. According to the Wiener-Kinchin theorem, the autocorrelation function of a signal $a(t)$ is the Fourier transform pair of its PSD

$$S_{\mathrm{aa}}(\omega) = \int_{-\infty}^{\infty} d\tau\, \langle a(t)a^*(t+\tau)\rangle\, e^{i\omega\tau}. \tag{3.10}$$

Knowing the Fourier transform[1] of the signal we obtain

$$S_{\mathrm{aa}}(\omega) = \left\langle |a(\omega)|^2 \right\rangle. \tag{3.11}$$

By plugging 3.7 into 3.11 we relate the displacement spectrum to the power spectral density of the force

$$S_{\mathrm{zz}}(\omega) = |\chi(\omega)|^2 S_{\mathrm{FF}}(\omega). \tag{3.12}$$

This result is the equivalent of Eq. 3.7, but expressed in experimentally accessible quantities.

Following linear response theory [77], the fluctuation dissipation theorem, in the classical limit, yields the power spectrum of the single-sided thermal force noise

$$S_{\mathrm{F}}^{\mathrm{th}}(\omega) = -\frac{4k_{\mathrm{B}}T}{\omega} Im\left(\frac{1}{\chi(\omega)}\right). \tag{3.13}$$

Here, k_{B} is the Boltzmann constant and T temperature. For weak damping, this equation can be written as

$$S_{\mathrm{F}}^{\mathrm{th}} = 4k_{\mathrm{B}}T m_{\mathrm{eff}}\Gamma_{\mathrm{m}}. \tag{3.14}$$

The thermal force noise $S_{\mathrm{F}}^{\mathrm{th}}$ is white and depends only on the bath temperature, the mechanical dissipation rate and the effective mass of the mechanical resonator. We finally state the displacement power spectrum by plugging Eq. 3.14 into Eq. 3.12

$$S_{\mathrm{z}} = \frac{4k_{\mathrm{B}}T\Gamma_{\mathrm{m}}}{m_{\mathrm{eff}}[(\omega_{\mathrm{m}}^2 - \omega^2)^2 + \Gamma_{\mathrm{m}}^2\omega^2]}, \tag{3.15}$$

[1] We use the following conventions $a(t) = \frac{1}{2\pi}\int_{-\infty}^{\infty} a(\omega)e^{-i\omega t}$ and $a(\omega) = \int_{-\infty}^{\infty} dt\, a(t)e^{i\omega t}$.

which we use to relate the bath temperature in thermal equilibrium to the variance of the displacement $\langle z_{\mathrm{th}}^2 \rangle$. We know from the equipartition theorem

$$\frac{1}{2} m_{\mathrm{eff}} \langle \dot{z}_{\mathrm{th}}^2 \rangle = \frac{1}{2} k \langle z_{\mathrm{th}}^2 \rangle = \frac{1}{2} k_{\mathrm{B}} T \tag{3.16}$$

and therefore

$$\langle z_{\mathrm{th}}^2 \rangle = \frac{k_{\mathrm{B}} T}{m_{\mathrm{eff}} \omega_{\mathrm{m}}^2}. \tag{3.17}$$

It further can be shown that the variance is the area under the single-sided displacement spectrum, from which we follow

$$\langle z_{\mathrm{th}}^2 \rangle = \int_0^\infty \frac{1}{2\pi} d\omega S_{\mathrm{z}}(\omega) = \frac{k_{\mathrm{B}} T}{m_{\mathrm{eff}} \omega_{\mathrm{m}}^2}. \tag{3.18}$$

This result allows to characterize the temperature of a mechanical mode by integrating over the experimental displacement noise, see Fig. 3.2.

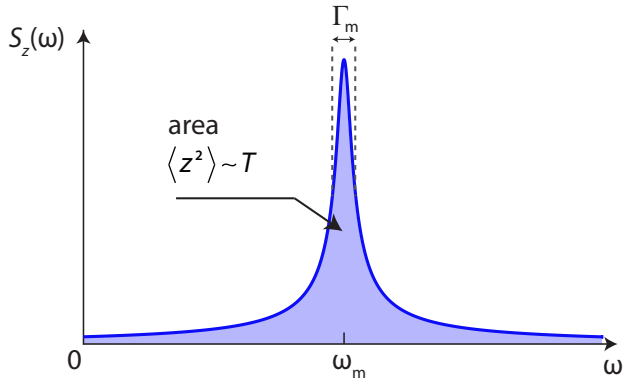

Figure 3.2: **Thermal noise displacement spectrum versus frequency.** The area under the displacement power spectral density is proportional to the temperature of the mechanical mode. Panel is adapted from [3].

3.1.3 The duffing oscillator with linear damping

The harmonic oscillator model is a good approximation for nanomechanical resonators as long as the involved restoring forces scale linearly with the displacement. This is satisfied for small motional displacements. When nanomechanical resonators are driven to larger displacement amplitudes, nonlinear restoring forces become important. These forces find their origin in geometrical nonlinearities or in nonlinear external potentials [78, 79]. Another source of nonlinear behavior is the intrinsic stress strain relationship of the material, but this typically requires much larger oscillation amplitudes.

To model nonlinear behavior, we include the cubic nonlinear force in the driven equation of motion

$$m_{\mathrm{eff}} \ddot{z}(t) + m_{\mathrm{eff}} \Gamma_{\mathrm{m}} \dot{z}(t) + m_{\mathrm{eff}} \omega_m^2 z(t) + \alpha_{\mathrm{eff}} z^3(t) = F_{\mathrm{d}} \cos(\omega_{\mathrm{d}} t) \tag{3.19}$$

with $\alpha_{\rm eff}$ the duffing nonlinear constant. Note that we assume a conservative damping term, and symmetry between z and $-z$, which is accounted for by the absence of a quadratic nonlinear force. Non-linear damping and symmetry breaking are discussed in Secs. 3.1.4 and 6.8, respectively. In analogy to the linear line shape we get for the amplitude of motion

$$z(\omega_{\rm d}) \approx \frac{F_{\rm d}/2m_{\rm eff}\omega_{\rm m}^2}{\sqrt{\left(\frac{\omega_{\rm d}-\omega_{\rm m}}{\omega_{\rm m}} - \frac{3}{8}\frac{\alpha_{\rm eff}}{m_{\rm eff}\omega_{\rm m}^2}z^2\right)^2 + (2Q_{\rm m})^{-2}}} \tag{3.20}$$

in the limit of comparatively small oscillations where $\alpha_{\rm eff}z^3 < kz$ [78]. Due to the appearance of z^2 terms on the right-hand side of the equation, the amplitude response is a cubic polynomial in z^2. As a consequence, one finds that above a critical amplitude the equation has three solutions, of which two are stable. This leads to bistable and hysteretic behavior above a certain vibration amplitude close to the mechanical resonance frequency. The onset of bistability is given by

$$z_{\rm crit} = \sqrt{\frac{8}{3\sqrt{3}}\frac{m_{\rm eff}\omega_m^2}{Q_{\rm m}\alpha_{\rm eff}}} = 1.24\sqrt{\frac{m_{\rm eff}\omega_m^2}{Q_{\rm m}\alpha_{\rm eff}}}. \tag{3.21}$$

Thus, the duffing nonlinearity $\alpha_{\rm eff}$ can be calculated from the critical deflection amplitude $z_{\rm crit}$. Furthermore, the frequency for which the amplitude of vibration is maximum is shifted by

$$\Delta\omega = \frac{3}{8}\frac{\alpha_{\rm eff}}{m_{\rm eff}\omega_{\rm m}}z_{\rm max}^2 \tag{3.22}$$

from the mechanical resonance frequency $\omega_{\rm m}$. The frequency shift is positive (negative) when $\alpha_{\rm eff} > 0$ ($\alpha_{\rm eff} < 0$), which corresponds to a hardening (softening) of the effective mechanical spring constant (see Fig. 3.3).

3.1.4 The duffing oscillator with the dissipative force $F = \eta z^2\dot{z}$

Not only the resonance frequency but also the damping rate can depend on the vibrational amplitude. This has only recently been verified in experiments using nanomechanical and micromechanical resonators. It was observed in graphene and carbon nanotubes [22], in a micromechanical beam [80], and in diamond nanoelectromechanical resonators [79]. Phenomenologically, nonlinear dissipation has been modeled by using a dissipation force $F = \eta z^2\dot{z}$ with η a constant [78]. The resulting equation of motion is given by

$$m_{\rm eff}\ddot{z}(t) + m_{\rm eff}\omega_{\rm m}^2 z(t) + [\Gamma_{\rm m} + \eta z^2(t)]\dot{z}(t) + \alpha_{\rm eff}z^3(t) = F_{\rm d}(t). \tag{3.23}$$

The amplitude response in the frequency domain is of the form

$$z(\omega_{\rm d}) \approx \frac{F_{\rm d}/2m_{\rm eff}\omega_{\rm m}^2}{\sqrt{\left(\frac{\omega_{\rm d}-\omega_{\rm m}}{\omega_{\rm m}} - \frac{3}{8}\frac{\alpha_{\rm eff}}{m_{\rm eff}\omega_{\rm m}^2}z^2\right)^2 + \left(\frac{1}{2}Q_{\rm m}^{-1} + \frac{1}{8}\frac{\eta}{m_{\rm eff}\omega_{\rm m}}z^2\right)^2}}. \tag{3.24}$$

While the duffing constant $\alpha_{\rm eff}$ can be extracted from the frequency shift given by Eq. 3.22, the determination of the nonlinear dissipation constant η is more involved. It is instructive

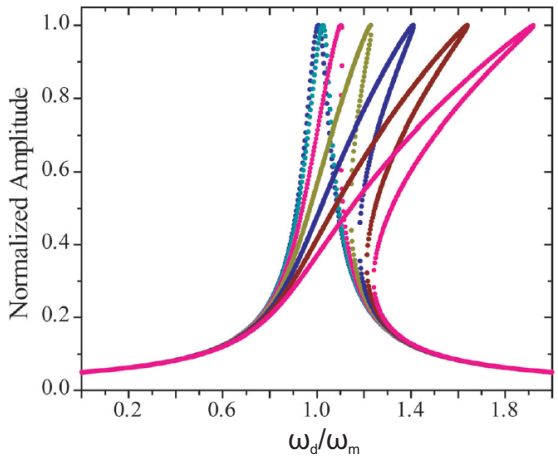

Figure 3.3: **Mechanical line shape of the duffing oscillator.** Normalized mechanical oscillation amplitude as a function of drive frequency ω_d. The driving force increases from blue to purple. For large driving the point of maximum amplitude shifts towards higher frequency, indicating $\alpha_\mathrm{eff} > 0$. Panel is adapted from [79]

to plot the maximum amplitude z_max divided by the driving force F_d as a function of z_max

$$\frac{z_\mathrm{max}}{F_\mathrm{d}} = \left(\frac{\eta \cdot \omega_\mathrm{m} z_\mathrm{max}^2}{4} + \frac{m_\mathrm{eff}\omega_\mathrm{m}^2}{Q_\mathrm{m}} \right)^{-1}. \tag{3.25}$$

Fig. 3.4 shows the theoretically predicted spectra for $\eta > 0$, and reveals that the ratio $z_\mathrm{max}/F_\mathrm{d}$ decreases as the vibrational amplitude and the driving force increase. This is directly linked to the increased damping for larger vibration amplitude, which can be approximated by a displacement dependent dissipation of the form [79]

$$\frac{1}{Q_\mathrm{m}} \approx \frac{1}{Q_0} + \frac{\eta z^2}{4}. \tag{3.26}$$

Here Q_0 is the mechanical quality factor without nonlinear dissipation. However, in the frequency domain, it is nontrivial to quantify the mechanical quality factor since the mechanical line shape can not be approximated by a Lorentzian. It is therefore much more direct to investigate the damping with a decay measurement in the time domain.

3.1.5 Mechanical energy decay

Recording mechanical vibrations in the time domain gives direct access to mechanical energy dissipation processes. Experimentally, this consists of driving the resonator with a capacitive driving force for time $t < 0$. At $t = 0$ the drive is switched off and the vibration amplitude decays freely ($t > 0$) (see Fig. 3.5). The mechanical amplitude can be described by solving the equation of the damped un-driven harmonic oscillator during the ring-down

$$\ddot{z}(t) + \Gamma_\mathrm{m}\dot{z}(t) + \omega_\mathrm{m}^2 z(t) = 0 \tag{3.27}$$

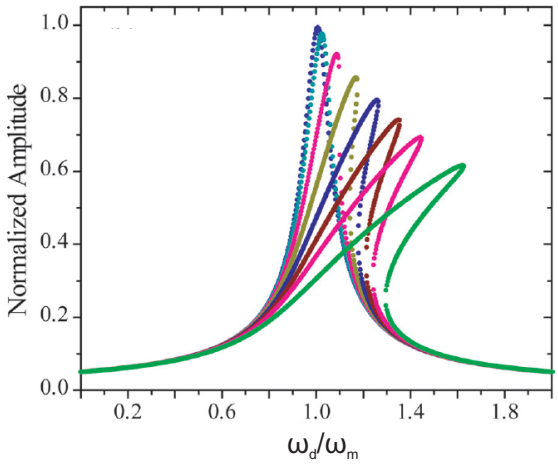

Figure 3.4: **Non-conservative damping for different driving force amplitudes.** Spectra of the vibration amplitude normalized by the driving force for different amplitudes. From blue to green the maximum vibration amplitude and the driving force increase while their ratio decreases. Panel is adapted from [79].

with the initial condition $z(t = 0) = z_0$. A solution in the limit of weak damping $\Gamma_\mathrm{m} << \omega_\mathrm{m}$ is given by

$$z(t) \approx z_0 \exp\left[-\frac{t}{2\tau}\right] cos(\omega t + \phi) \tag{3.28}$$

where $\omega = \sqrt{\omega_\mathrm{m}^2 - \frac{\Gamma_\mathrm{m}^2}{4}} \approx \omega_\mathrm{m}$ and $\tau = 1/\Gamma_\mathrm{m}$. It can be shown that the total mechanical energy $E(t) = \frac{1}{2} m_\mathrm{eff}[\omega_\mathrm{m}^2 z^2(t) + \dot{z}^2(t)]$ can be approximated by

$$E(t) \approx \frac{1}{2} m_\mathrm{eff} \omega_\mathrm{m}^2 z^2(t) \tag{3.29}$$

with

$$z^2(t) = z_0^2 \exp\left[-\frac{t}{\tau}\right]. \tag{3.30}$$

Here we note that this equation is valid for both the harmonic oscillator and the duffing oscillator with linear damping. The case of the dissipative damping force $F = \eta z^2 \dot{z}$ is theoretically captured by the approximation [80]

$$z^2(t) = z_0^2 \cdot \frac{\exp\left[-\frac{t}{\tau}\right]}{1 + \frac{2\eta}{8 m_\mathrm{eff}} \cdot \tau \cdot z_0^2 \cdot \left(1 - \exp\left[-\frac{t}{\tau}\right]\right)}. \tag{3.31}$$

We plot the energy decay for both cases in Fig. 3.5. Energy decay measurements have a decisive advantage compared to spectral measurements. As the total mechanical energy is independent of the phase of the mechanical resonator they are immune to fluctuations of the mechanical resonance frequency, which is in stark contrast to spectral measurements.

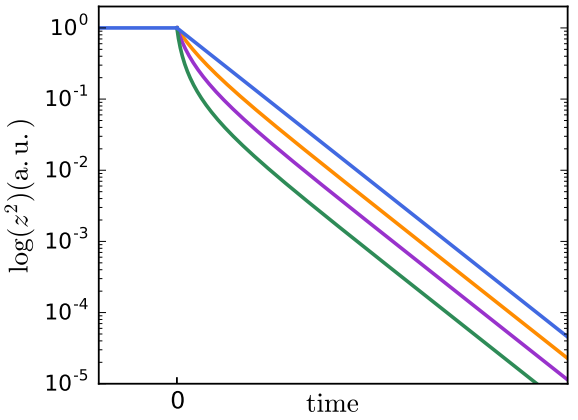

Figure 3.5: **Energy decay traces for varying η.** Logarithmus of the squared amplitude as a function of time. At time $t = 0$ the driving force is switched off. For $t > 0$ the mechanical energy decays freely. For the blue trace $\eta = 0$. The dissipative force parameter η increases from the blue trace to the green trace.

3.2 Circular graphene resonator in the membrane limit

In this section, we make the connection between the harmonic oscillator model introduced above and the circular membranes used in our experiments. For this, we introduce the effective mass that we obtain from the mode shape of the fundamental mechanical mode. We model the mechanical resonators as membranes under tension and derive explicit expressions for the mechanical resonant frequency, and the static displacement as a function of the electrostatic potential applied to a nearby gate electrode.

We model the local deflection $\xi(x, y, t)$ of the graphene resonator as a thin plate with negligible mechanical energy in bending compared to the energy resulting from the stretching (membrane limit) [81]

$$\rho_{2D} \frac{\partial^2 \xi}{\partial t^2} = T \nabla^2 \xi + P(x, y) \tag{3.32}$$

with ρ_{2D} the sheet mass density, $P(x, y)$ the local pressure in z-direction and T a stretching force per unit length at the edge of the membrane (see Fig. 3.6). If we consider radially symmetric modes $\xi(r, t)$, the stretching force T is then related to a radial strain $\epsilon = (R' - R)/R$ with the elongated radius R' by

$$T = Eh\epsilon = Etn_g\epsilon, \tag{3.33}$$

with the 2D graphene Young's modulus $Et = 340$ N/m, n_g the number of graphene layers and $t = 0.335$ nm [82] the interlayer spacing in graphite. The total sheet mass density $\rho_{2D} = \nu n_g \rho_{\text{graphene}}$ includes the mass from the graphene layers, with the graphene mass density ρ_{graphene}, and a correction factor $\nu \geq 1$ to account for additional adsorbents on the graphene.

The electrostatic pressure due to the gate voltage, which is applied between the membrane and a nearby circular electrode, is modeled in a parallel plate approximation with

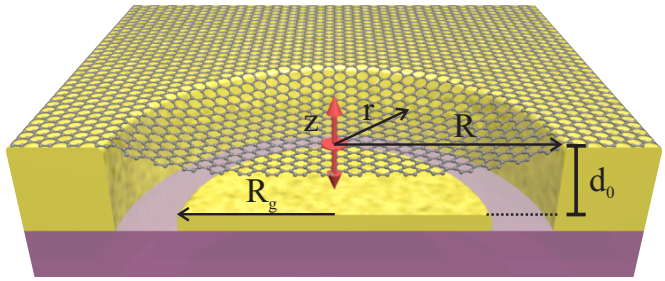

Figure 3.6: **Schematic cross-section of a suspended circular graphene membrane.** The graphene resonator with radius R is suspended above a circular counter electrode with radius R_g and distance d_0. The deflection of the central point of the membrane is denoted by z and the radial distance of an arbitrary point of the membrane to the center by $r = \sqrt{x^2 + y^2}$ where x, y are the cartesian in-plane coordinates. The deflection of an arbitrary point of the membrane at time t is given by $\xi(x, y, t)$, see text.

the capacitive energy given by $U = \frac{1}{2} C_\mathrm{m} V_\mathrm{g}^2$. If we expand the capacitance in terms of ξ we get

$$\begin{aligned} U &\approx \int dxdy \frac{\epsilon_0 V_\mathrm{g}^2}{2} \frac{1}{d - \xi(x,y)} \\ &\approx \int dxdy \frac{\epsilon_0 V_\mathrm{g}^2}{2d} \left(1 + \frac{\xi(x,y)}{d} + \frac{\xi(x,y)^2}{d^2} + \frac{\xi(x,y)^3}{d^3} + \dots\right) \\ P(x,y) &\approx \frac{\epsilon_0 V_\mathrm{g}^2}{2d^2} \left(1 + \frac{2\xi(x,y)}{d} + \frac{3\xi(x,y)^2}{d^2} + \frac{4\xi(x,y)^3}{d^3} + \dots\right). \end{aligned}$$

The differential equation for the deflection is then given by

$$\rho_\mathrm{2D} \frac{\partial^2 \xi}{\partial t^2} = T\nabla^2 \xi + \frac{\epsilon_0 V_\mathrm{g}^2}{2d^2} \left(1 + \frac{2\xi(x,y)}{d} + \frac{3\xi(x,y)^2}{d^2} + \frac{4\xi(x,y)^3}{d^3} + \dots\right) \tag{3.34}$$

To solve the equation, we decompose the deflection $\xi(r, t)$ into a static displacement $\xi_\mathrm{s}(r)$ and time-dependent (radial) modes k with amplitude $\xi_\mathrm{k}(r)$

$$\xi(r,t) \approx \xi_\mathrm{s}(r) + \sum_k \xi_\mathrm{k}(r) e^{-i\omega t}. \tag{3.35}$$

3.2.1 Static displacement as a function of DC voltage

For the static displacement we have

$$0 = T\nabla^2 \xi_\mathrm{s}(r) + \frac{\epsilon_0 V_\mathrm{g}^2}{2d^2} \left(1 + \frac{2\xi_\mathrm{s}(r)}{d} + \dots\right) \tag{3.36}$$

by assuming $2\xi_\mathrm{s}(r)/d \ll 1$. The solution at lowest order in $\xi_\mathrm{s}(r)/d$ is given by

$$\xi_\mathrm{s}(r) = \frac{\epsilon_0 V_\mathrm{g}^2}{8Td^2} \left(r^2 - R^2\right) \tag{3.37}$$

with the normalized center deflection

$$z_{\mathrm{s}} = \frac{\epsilon_0 R_{\mathrm{g}}^2}{8Td^2} V_{\mathrm{g}}^2 = c_{\mathrm{s}} V_{\mathrm{g}}^2. \tag{3.38}$$

The validity of this mode shape has been confirmed with numerical simulations.

3.2.2 Mechanical resonance frequency as a function of gate voltage

If we assume orthogonal modes and neglect mode coupling, we can project Eq. (3.34) on the fundamental mode

$$-\rho_{2\mathrm{D}}\omega^2 \xi_{\mathrm{f}}(r) = T\nabla^2 \xi_{\mathrm{f}}(r) + \frac{\epsilon_0 V_{\mathrm{g}}^2}{d^3} \xi_{\mathrm{f}}(r) \tag{3.39}$$

and solve for the fundamental mode amplitude $\xi_{\mathrm{f}}(r)$. Considering a clamped boundary with $\xi_{\mathrm{f}}(R) = 0$ we get

$$\xi_{\mathrm{f}}(r) = z_0 J_0\left(\frac{2.4}{R} r\right), \tag{3.40}$$

where $z_0 = \xi_{\mathrm{f}}(0)$ is the deflection amplitude at the center of the membrane and J_0 is the 0th Bessel function with $J_0(2.4) = 0$. The resonance frequency as a function of gate voltage is then given by

$$\omega_{\mathrm{m}}(V_{\mathrm{g}}) = \sqrt{\frac{2.4^2 T}{R^2 \rho_{2\mathrm{D}}} - \frac{\epsilon_0}{d^3 \rho_{2\mathrm{D}}} V_{\mathrm{g}}^2}. \tag{3.41}$$

By taking into account the reduced radius of the gate electrode R_{g} with respect to the membrane radius R, the electrical force gets reduced by a factor R_{g}^2/R^2 and we obtain

$$\omega_{\mathrm{m}}(V_{\mathrm{g}}) = \sqrt{\frac{2.4^2 T}{R^2 \rho_{2\mathrm{D}}} - \frac{R_g^2}{R^2} \frac{\epsilon_0}{d^3 \rho_{2\mathrm{D}}} V_{\mathrm{g}}^2} \tag{3.42}$$

for the resonance frequency as a function of V_{g}. At $V_{\mathrm{g}} = 0$ V we get in agreement with Ref. [83]

$$\omega_{\mathrm{m}}(0) = \frac{2.404}{R} \sqrt{\frac{Eh\epsilon}{\rho_{2\mathrm{D}}}}. \tag{3.43}$$

3.2.3 The effective mass and the effective driving force

Knowing the mode shape of the fundamental mode, we are one step closer to the harmonic oscillator equivalent model introduced before. In particular, we are able to derive the effective mass of the circular membrane and obtain the mechanical resonance frequency as a function of V_{g} by solving the equation of motion for a point mass. From the total kinetic energy

$$E_{\mathrm{kin}} = \frac{1}{2} \rho_{2\mathrm{D}} 2\pi \omega_{\mathrm{m}}^2 \int r \xi_{\mathrm{f}}^2(r) dr = \frac{1}{2} m_{\mathrm{eff}} \omega_{\mathrm{m}}^2 z^2 \tag{3.44}$$

we obtain for the effective mass

$$m_{\mathrm{eff}} = 0.27\rho_{\mathrm{2D}}\pi R^2, \tag{3.45}$$

with

$$2\pi\int_0^R dr J_0^2\left(\frac{2.4}{R}r\right)r = 2\pi\frac{R^2}{2.4^2}\int_0^{2.4} dr' J_0^2(r')r' = 0.27\pi R^2.$$

We multiply all the terms of Eq. (3.34) by $J_0\left(\frac{2.4}{R}r\right)$ and integrate over the area. As a result, we get the normalized equation of motion with higher order corrections for the capacitive force

$$\begin{aligned} m_{\mathrm{eff}}\omega^2 z_0 &= \left(0.271\pi R^2 2.4^2 T - 0.271\frac{\epsilon_0\pi R_{\mathrm{g}}^2 V_{\mathrm{g}}^2}{d^3}\right)z_0 \\ &\quad +0.196\frac{3\epsilon_0\pi R_{\mathrm{g}}^2 V_{\mathrm{g}}^2}{2d^4}z_0^2 \\ &\quad +0.125\frac{2\epsilon_0\pi R_{\mathrm{g}}^2 V_{\mathrm{g}}^2}{d^5}z_0^3 + \ldots. \end{aligned} \tag{3.46}$$

Note that we obtain the same expression as Eq. 3.42 for the resonance frequency

$$\omega_{\mathrm{m}}(V_{\mathrm{g}}) = \sqrt{\frac{4.92Eh\epsilon}{m_{\mathrm{eff}}} - \frac{0.271}{m_{\mathrm{eff}}}\frac{\epsilon_0\pi R_{\mathrm{g}}^2}{d^3}V_{\mathrm{g}}^2} = \sqrt{\frac{2.4^2 T}{R^2\rho_{\mathrm{2D}}} - \frac{R_{\mathrm{g}}^2}{R^2}\frac{\epsilon_0}{d^3\rho_{\mathrm{2D}}}V_{\mathrm{g}}^2}. \tag{3.47}$$

The effective mass modeling also leads to a correction in the electrostatic driving force. We obtain the correction factor similarly as the higher order corrections in Eq. 3.46 by considering the capacitive term that scales as z^0 in Eq. 3.34. Integration over the mode shape yields the capacitive driving force

$$F_{\mathrm{d}} = \partial_{\mathrm{z}}C_{\mathrm{m}}V_{\mathrm{g}}\sqrt{2}V_{\mathrm{g}}^{\mathrm{AC}} = 0.433\frac{\epsilon_0\pi R_{\mathrm{g}}^2}{d^2}V_{\mathrm{g}}\sqrt{2}V_{\mathrm{g}}^{\mathrm{AC}} \tag{3.48}$$

with $V_{\mathrm{g}}^{\mathrm{AC}}$ the rms-value of the oscillating driving voltage. The oscillating force drives the central point of the membrane to a vibrational amplitude z_0.

In conclusion, we have modeled the graphene mechanical resonators used in this dissertation as circular membranes under tension. We first derived the fundamental mode shape in the membrane limit, and then looked at static displacement and the mechanical resonance frequency under the influence of a static voltage applied to a nearby gate electrode. Finally, we linked the obtained mode shape to the harmonic oscillator model and included the effective mass correction into the AC driving force amplitude.

Chapter 4

Microwave optomechanics

In this chapter we introduce the system that we use to readout and manipulate graphene mechanical motion. It consists of a graphene mechanical resonator capacitively coupled to a Nb superconducting microwave cavity (SMC). This chapter is divided into two parts. In the first part, we derive expressions for the cavity transmission and reflection coefficients, respectively, neglecting the coupling to the mechanical resonator. Using transmission line theory and idealized lumped-element models of the SMCs, we calculate the expected output signal levels and their frequency dependence for a given input signal. In the second part, we discuss the parametrical interaction between the nanomechanical resonator (NR) and the electromagnetic mode of the SMC. We present the quantum mechanical formulation of the optomechanical interaction, but also a classical analysis by incorporating the NR as a moving capacitor into the lumped-element circuit. Although the classical approach is satisfactory to describe the results in this dissertation, a quantum mechanical description is necessary to describe, for instance, the limitations of sideband cooling correctly [84, 85]. We conclude the chapter with a short discussion on measurement limitations.

To motivate the derivations in this chapter, we show an example of a device and its lumped-element equivalent in Fig. 4.1. The NR is embedded into the quarter-wavelength reflection cavity at its open end where the electromagnetic field amplitudes are maximum. The SMC is capacitively coupled to the cryogenic circuitry and its output signal is amplified by a cryogenic high-electron-mobility transistor (HEMT). The chip is mounted at the mixing chamber of a dilution refrigerator with a base temperature of $T = 15\,\mathrm{mK}$.

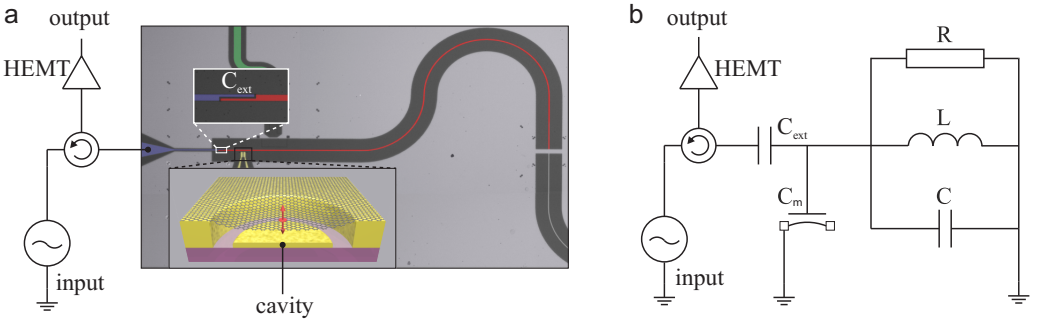

Figure 4.1: **Device example and its lumped-element equivalent circuit.** (**a**) On-chip coplanar waveguide cavity (red line) capacitively coupled to a circularly clamped graphene mechanical resonator (black rectangle and inset). The device is measured at cryostat base temperature through an external coupling capacitor C_{ext} (white rectangle and inset). The cavity is excited with a microwave signal generated by the radio-frequency source at room temperature. The microwave signal is reflected from the cavity and amplified by a cryogenic HEMT amplifier. (**b**) The cavity is modeled as a lumped-element RLC circuit where the mechanical resonator is implemented as a position dependent capacitor C_{m}.

4.1 Superconducting microwave cavities

Superconducting microwave cavities are used as sensitive photon detectors in astronomy [86] as well as in cavity quantum electrodynamics [87, 88]. They are furthermore a very promising platform for future quantum information processing [89] when combined with different physical systems. Examples include artificial atoms in the form of superconducting quantum bits [90], quantum dots [91, 92], spin ensembles [93] and mechanical resonators [94, 36, 38]. SMCs are often fabricated as coplanar waveguide or microstrip resonators. These geometries are compatible with large scale on-chip microfabrication techniques and with low-temperature environments.

4.1.1 Transmission line theory

We model both the coplanar waveguide and the meandered microstrip cavities (Sec. 5.1.2), used in our experiments, by means of transmission line theory. Here we summarize the main results and give a rough outline of how to derive them. For the details of the analysis we refer to [95, 96]. A transmission line is a conductor line and a ground line/plane in parallel (see central part of Fig. 4.3(a)). The equivalent circuit of a short piece of transmission line dx of the conductor pair is characterized by a series inductor L' and a series resistor R'_{s} per unit length, and by a shunt capacitor C' and a shunt conductor G'. The ohmic losses of the system can be summarized by $R' = R'_{\mathrm{s}} + G'(Z'_0)^2$ [97]. Here we define the characteristic impedance

$$Z'_0 = \sqrt{\frac{L'}{C'}}, \tag{4.1}$$

for small losses.

Applying Kirchhoff's laws for the propagating current and voltage along the line yields the steady-state wave equations for both the current and the voltage for a transmission

line of finite length. The solutions are given by

$$V(x) = V_0^+ e^{-\gamma x} + V_0^- e^{\gamma x} \tag{4.2}$$

$$I(x) = \frac{V_0^+}{Z_0} e^{-\gamma x} - \frac{V_0^-}{Z_0} e^{\gamma x} \tag{4.3}$$

where + (-) represents wave propagation in the positive (negative) x-direction and $\gamma = \alpha + i\beta$ is the complex wave number. The attenuation constant for small losses, $R' \ll \omega L'$, is $\alpha = \frac{R'}{2Z_0'} = \frac{1}{2}\sqrt{L'C'}\frac{R'}{L'}$ and the propagation constant is $\beta = \omega\sqrt{L'C'}$ with ω the frequency of the signal wave.

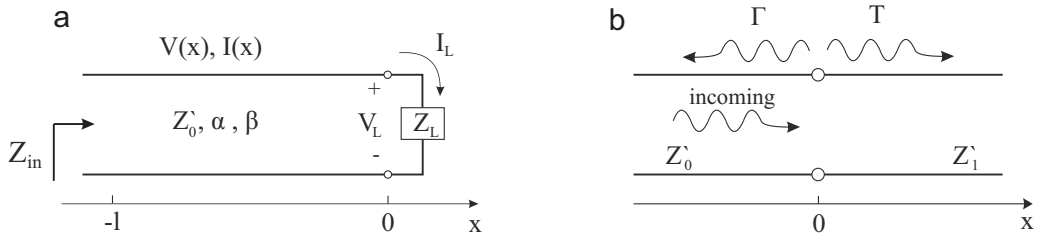

Figure 4.2: **Low loss transmission line with different terminations.** (**a**) A transmission line with characteristic impedance Z_0' is terminated by an arbitrary load at $x = 0$. Reflection of an incoming wave with voltage reflection coefficient Γ at the load leads to a standing wave pattern. (**b**) A transmission line with characteristic impedance Z_0' feeds a transmission line with characteristic impedance Z_1'. Part of the incoming wave is transmitted with voltage transmission coefficient T.

Let us assume a finite length transmission line with characteristic impedance Z_0' that is terminated by an arbitrary load with impedance Z_L, see Fig. 4.2(a). For an incoming wave of the form $V_0^+ e^{-\gamma \mathrm{x}}$ the boundary condition $Z_\mathrm{L} = V(x=0)/I(x=0)$ needs to be fulfilled, which, in general, leads to wave reflection at $x = 0$. The reflection coefficient is defined as the voltage amplitude of the reflected wave normalized by the incident wave. By plugging Eqs. 4.2 and 4.3 into the boundary condition we obtain

$$\Gamma = \frac{V_0^-}{V_0^+} = \frac{Z_\mathrm{L} - Z_0'}{Z_\mathrm{L} + Z_0'}. \tag{4.4}$$

When the impedances Z_L and Z_0' are equal, the load is said to be matched and we have $\Gamma = 0$. When on the other hand the impedances are mismatched, the incident and the reflected wave interfere and form a standing wave pattern along the transmission line. As a result, the impedance along the line is a function of the distance from the load. The expression for the input impedance at position $-l$ of a transmission line terminated by an arbitrary load is given by

$$Z_\mathrm{in} = Z_0 \frac{Z_\mathrm{L} + Z_0 \tanh(\gamma l)}{Z_0 + Z_\mathrm{L} \tanh(\gamma l)}. \tag{4.5}$$

Since, in our experiments, we use transmission line cavities that are short circuited ($Z_\mathrm{L} = 0$) at one end the input impedance can be simplified to

$$Z_\mathrm{in} = Z_0 \tanh(\gamma l). \tag{4.6}$$

We note that for a vanishing load impedance the voltage at the load vanishes, the current is maximum and all the power is reflected with $\Gamma = -1$.

Similarly to the reflection coefficient, we can define a transmission coefficient T that quantifies the transmitted voltage amplitude. For this, we consider a transmission line with characteristic impedance Z_0' feeding a transmission line with characteristic impedance Z_1' at $x = 0$. Let $V(x) = V_0^+(e^{-\gamma x} + \Gamma e^{\gamma x})$ be the wave at $x < 0$ and $V(x) = V_0^+ T e^{-\gamma x}$ the wave at $x > 0$. Equating these voltages at $x = 0$ yields the transmission coefficient

$$T = 1 + \Gamma = \frac{2Z_1'}{Z_1' + Z_0'}. \tag{4.7}$$

The quarter-wavelength transmision line

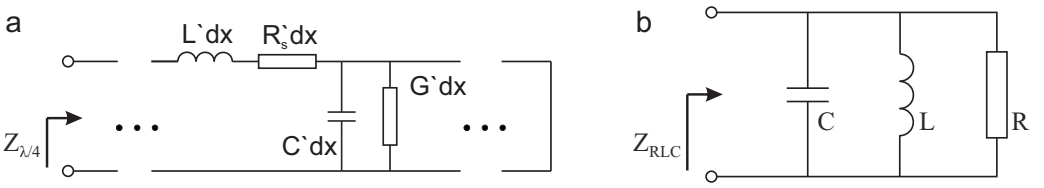

Figure 4.3: **Representation of the quarter-wavelength transmission line as a parallel *RLC* circuit.** (**a**) Finite length transmission line composed of a cascade of several elements of length dx. The boundary conditions with one open-end and one short-circuited end define a resonant cavity with $l = \lambda/4$ (see text). The input impedance is $Z_{\lambda/4}$. (**b**) Equivalent parallel *RLC* circuit of the transmission line of **a**. The circuit has input impedance Z_{RLC}.

Terminating the transmission line at both ends transforms it into a resonant cavity (Fig. 4.3(a)). For the second termination we choose the open end at $x = -l$, so that the resonance condition for a particular frequency is given by $l = \lambda/4$ with λ the wavelength. As a reminder, for the first boundary condition we chose the short-circuited end at $x = 0$. Here we only want to consider the fundamental resonance and find the expression for the input impedance $Z_{\lambda/4}$ close to resonance $\omega_{\lambda/4}$. We write the frequency as a small deviation from resonance $\omega = \omega_{\lambda/4} + \Delta\omega$ and state the resonance condition in terms of the propagation constant $\beta l = \pi/2(1+\Delta\omega/\omega_{\lambda/4}) = (\omega_{\lambda/4}+\Delta\omega)\sqrt{L'C'}l)$. For small losses Eq. 4.6 can be approximated by [96, 95]

$$Z_{\lambda/4} \approx \frac{Z_0'}{\alpha l + i\pi\frac{\Delta\omega}{2\omega_{\lambda/4}}} = \frac{1}{\frac{R'C'}{2L'}l + iC'l\Delta\omega}. \tag{4.8}$$

On the other hand, it is convenient to model the quarter-wavelength transmission line as a parallel lumped-element *RLC* circuit with effective resistance R, effective inductance L, and effective capacitance C (see Fig. 4.3(b)). The input impedance of the parallel *RLC* circuit is given by

$$Z_{\mathrm{RLC}} = \left(\frac{1}{R} + i\omega C + \frac{1}{i\omega L}\right)^{-1}. \tag{4.9}$$

The circuit is resonant when the impedance associated to the inductance is equal to the impedance of the capacitance ($\mathrm{Im}(Z_{\mathrm{in}}(\omega_{\mathrm{RLC}})) = 0$). This is equivalent to

$$\omega_{\mathrm{RLC}} = \frac{1}{\sqrt{LC}}. \tag{4.10}$$

Using the relation $\omega^2 - \omega_{\mathrm{RLC}}^2 = (\omega - \omega_{\mathrm{RLC}})(\omega + \omega_{\mathrm{RLC}}) = \Delta\omega(2\omega - \Delta\omega) \approx 2\omega\Delta\omega$ the input impedance, near resonance, can be approximated by

$$Z_{\mathrm{RLC}} \approx \frac{1}{1/R + 2iC\Delta\omega} \approx \frac{R}{1 + 2iQ_{\mathrm{int}}\Delta\omega/\omega_{\mathrm{RLC}}}. \tag{4.11}$$

Here we have used the definition of the quality factor of the parallel RLC circuit

$$Q_{\mathrm{int}} = \frac{R}{Z_0} = R\sqrt{\frac{C}{L}} = \omega_{\mathrm{RLC}}RC. \tag{4.12}$$

Comparing the input impedance of the quarter-wavelength transmission line (Eq. 4.8) with the input impedance of the parallel RLC circuit (Eq. 4.11) we can state the following relations

$$\omega_{\lambda/4} = \frac{\pi}{2l\sqrt{L'C'}} \tag{4.13}$$

$$R = \frac{2}{l}\frac{L'}{R'C'} \tag{4.14}$$

$$C = \frac{l}{2}C' \tag{4.15}$$

$$L = \frac{8l}{\pi^2}L'. \tag{4.16}$$

The quality factor then takes on the simple form

$$Q_{\mathrm{int}} = \frac{\beta}{2\alpha}. \tag{4.17}$$

Plugging the obtained relations into equation 4.8 we obtain the input impedance of the quarter-wavelength transmission line, near resonance,

$$Z_{\lambda/4} = \frac{4Z_0'Q_{\mathrm{int}}}{\pi}\frac{1}{1 + 2iQ_{\mathrm{int}}\frac{\Delta\omega_{\lambda/4}}{\omega_{\lambda/4}}}. \tag{4.18}$$

Hereafter, we will use the expression cavity when referring to the quarter-wavelength transmission line.

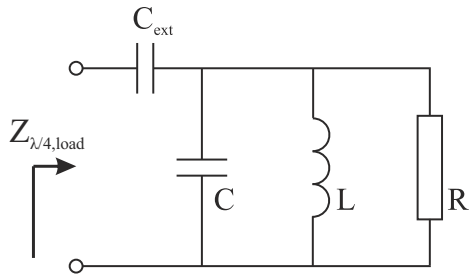

Figure 4.4: **Capacitively coupled parallel RLC circuit.** Lumped-element circuit coupled to transmission line (external circuitry) with external coupling capacitor C_{ext}.

Capacitively coupled transmission line

So far, we assumed that both ends of the cavity are perfectly terminated. We modify this concept by allowing a small part of the signal leaking out of the open end, or in other terms, we couple the cavity to our measurement lines with real characteristic impedance R_{L}. The coupling is capacitive and quantified by the external coupling capacitor C_{ext} (see Fig. 4.4). In order to obtain the input impedance of the entire circuit, we model it as a series combination of the coupling capacitor with the cavity [98]

$$Z_{\lambda/4,\mathrm{load}} = Z_{\lambda/4} + \frac{1}{i\omega C_{\mathrm{ext}}} \approx \frac{\pi}{4Z_0'\omega_{\mathrm{c}}^2 C_{\mathrm{ext}}^2 Q_{\mathrm{int}}} \left(1 + \frac{2iQ_{\mathrm{int}}\Delta\omega_{\mathrm{c}}}{\omega_{\mathrm{c}}}\right) \tag{4.19}$$

where, in the last step, we demand that the impedance on resonance ω_{c} is real ($\mathrm{Im}[Z_{\lambda/4,\mathrm{load}}(\omega_0)] = 0$). This requirement yields a relation between $\omega_{\lambda/4}$ and ω_{c}, which is recursively plugged into the equation for the impedance. Also, we define $\Delta\omega_{\mathrm{c}} = \omega - \omega_{\mathrm{c}}$. The input impedance of the loaded cavity is going to be the basis for the determination of the scattering parameters of the cavities used in our experiments, as discussed in the following two subsections.

Reflection measurement of a $\lambda/4$ cavity

A schematic of the measurement circuit for a quarter-wavelength cavity measured in reflection is shown in Fig. 4.5(a). The signal is generated at the radio frequency source. It travels down the cryostat lines with characteristic impedance R_{L}. A fraction of the microwave power is transmitted through the coupling capacitor into the cavity. The coupling rate $\kappa_{\mathrm{ext}} = \omega/Q_{\mathrm{ext}}$ is defined over the external quality factor Q_{ext}. Inside the cavity, the electromagnetic wave resides for Q_{tot} round trips before it is either dissipated with rate $\kappa_{\mathrm{int}} = \omega/Q_{\mathrm{int}}$ or leaves the cavity with rate κ_{ext}. A microwave circulator is used to separate input from output lines.

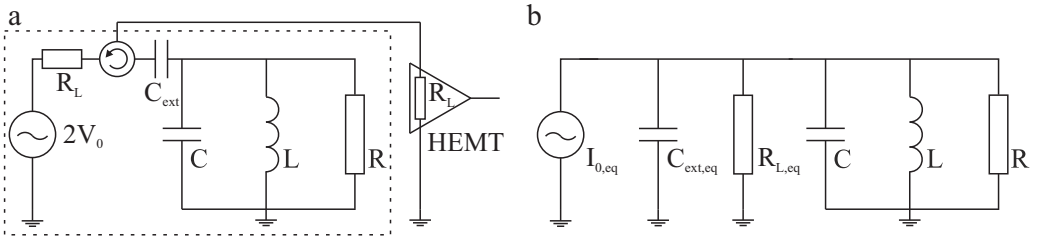

Figure 4.5: **Lumped element representation of reflection cavity coupled to external circuitry.** (**a**) Reflection cavity in series with radio-frequency source, cryostat lines with characteristic impedance R_{L} and cryogenic circulator (all inside the dotted rectangle). The output line with the cryogenic amplifier is shown for completeness. (**b**) Norton equivalent model of the circuit inside the dotted rectangle shown in **a**.

In order to quantify the external quality factor, we apply Norton's theorem [97]. We transform the source voltage being in series with the components R_{L} and C_{ext} (dotted rectangle in Fig. 4.5(a)) into the equivalent current $I_{0,\mathrm{eq}}$ being in parallel with $C_{\mathrm{ext,eq}}$ and $R_{\mathrm{L,eq}}$, Fig. 4.5(b). The equivalent, parallel, lumped-element components are then given

by

$$I_{0,\mathrm{eq}} = \frac{2V_0}{R_\mathrm{L} + \frac{1}{i\omega C_\mathrm{ext}}} \approx 2iV_0\omega C_\mathrm{ext} \tag{4.20}$$

$$R_{\mathrm{L,eq}} = \frac{1 + (\omega C_\mathrm{ext} R_\mathrm{L})^2}{R_\mathrm{L}(\omega C_\mathrm{ext})^2} \approx \frac{1}{R_\mathrm{L}(\omega C_\mathrm{ext})^2} \tag{4.21}$$

$$C_{\mathrm{ext,eq}} = \frac{C_\mathrm{ext}}{1 + (\omega C_\mathrm{ext} R_\mathrm{L})^2} \approx C_\mathrm{ext}. \tag{4.22}$$

We note that the voltage applied with the radio frequency source is doubled for the modeling of the equivalent current $I_{0,\mathrm{eq}}$. This is attributed to the reflection of the input signal at the coupling capacitor. Additionally, in our experiments, we have $\omega_\mathrm{c} \approx 2\pi \cdot 7.5\,\mathrm{GHz}$, $C_\mathrm{ext} \approx 10^{-15}\,\mathrm{F}$ and $R_\mathrm{L} = 50\,\Omega$, which validates the approximations in Eqs. 4.20-4.22. We introduce the total quality factor as the parallel combination of the intrinsic quality factor of the RLC circuit and the external quality factor

$$\frac{1}{Q_\mathrm{tot}} = \frac{1}{Q_\mathrm{int}} + \frac{1}{Q_\mathrm{ext}} = Z_0 \left(\frac{1}{R} + \frac{1}{R_{\mathrm{L,eq}}} \right). \tag{4.23}$$

Here we have neglected the shift in Z_0 arising from C_ext, because $C_\mathrm{ext} << C$. We obtain the external quality factor

$$Q_\mathrm{ext} = \frac{R_{\mathrm{L,eq}}}{Z_0} = \frac{\pi}{4Z_0' R_\mathrm{L}(\omega_\mathrm{c} C_\mathrm{ext})^2} \tag{4.24}$$

by using $Z_0 = \sqrt{\frac{L}{C}} = \frac{4}{\pi} Z_0'$ (see Eqs. 4.15 and 4.16). According to Eq. 4.4, the probability for a signal to be reflected from the cavity expressed in terms of the reflection matrix scattering element $S_{11} = \Gamma$ [96] is given by

$$|S_{11}|^2 = \left| \frac{Z_{\lambda/4,\mathrm{load}} - R_\mathrm{L}}{Z_{\lambda/4,\mathrm{load}} + R_\mathrm{L}} \right|^2 = \frac{(\kappa_\mathrm{int} - \kappa_\mathrm{ext})^2 + 4\Delta\omega_\mathrm{c}^2}{(\kappa_\mathrm{int} + \kappa_\mathrm{ext})^2 + 4\Delta\omega_\mathrm{c}^2}. \tag{4.25}$$

Interestingly, the reflection coefficient on resonance

$$|S_{11,\mathrm{min}}| = |1 - 2\frac{\kappa_\mathrm{ext}}{\kappa}| \tag{4.26}$$

is solely determined by the coupling efficiency $\kappa_\mathrm{ext}/\kappa$ with $\kappa = \kappa_\mathrm{ext} + \kappa_\mathrm{int}$.

Transmission measurement of a $\lambda/4$ cavity

In analogy to the reflection cavity we model the cavity measured in transmission in a lumped-element fashion using Norton's theorem. The lumped-element model and its Norton equivalent are shown in Fig. 4.6. For the equivalent circuit quantities

$$I_{0,\mathrm{eq}} \approx iV_0\omega C_\mathrm{ext} \tag{4.27}$$

$$R_{\mathrm{L,eq}} \approx \frac{2}{R_\mathrm{L}(\omega C_\mathrm{ext})^2} \tag{4.28}$$

$$C_{\mathrm{ext,eq}} \approx C_\mathrm{ext} \tag{4.29}$$

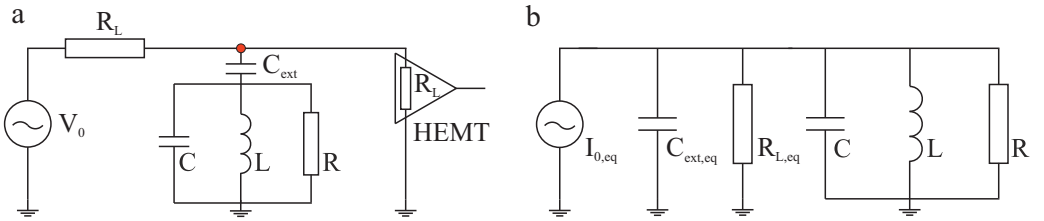

Figure 4.6: **Lumped element representation of $\lambda/4$ cavity measured in transmission.** (**a**) Cavity in parallel with radio-frequency source, cryostat lines with characteristic impedance R_L and cryogenic amplifier with load impedance R_L. (**b**) Norton equivalent model of the circuit shown in **a**.

we perform similar approximations as in the previous subsection. The external quality factor

$$Q_\mathrm{ext} = \frac{R_\mathrm{L,eq}}{Z_0} = \frac{\pi}{2Z_0' R_\mathrm{L} (\omega_\mathrm{c} C_\mathrm{ext})^2} \tag{4.30}$$

differs by a factor two from the external quality factor when measuring in reflection. We obtain the forward matrix scattering element $S_{21} = T$ [96] by calculating the parallel sum of the impedances $Z_{\lambda/4,\mathrm{load}}$ and R_L that an incoming signal encounters at the point marked as the red circle in Fig. 4.6(a)

$$\frac{1}{Z_\mathrm{tot}} = \frac{1}{R_\mathrm{L}} + \frac{1}{Z_{\lambda/4,\mathrm{load}}}. \tag{4.31}$$

According to Eq. 4.7, the probability for a signal to be transmitted is given by

$$|S_{21}|^2 = \left| \frac{2Z_\mathrm{tot}}{Z_\mathrm{tot} + R_\mathrm{L}} \right|^2 = \frac{S_{21,\mathrm{min}}^2 + 4(Q_\mathrm{tot} \frac{\Delta\omega_\mathrm{c}}{\omega_\mathrm{c}})^2}{1 + 4(Q_\mathrm{tot} \frac{\Delta\omega_\mathrm{c}}{\omega_\mathrm{c}})^2} \tag{4.32}$$

where on resonance $S_{21} = S_{21,\mathrm{min}} = \frac{Q_\mathrm{ext}}{Q_\mathrm{ext}+Q_\mathrm{int}}$.

4.1.2 Transmitted power

We are interested in the frequency dependence and in the magnitude of the output power P_out when applying a power P_in at the input port of the cryostat. In order to quantify the transmitted power, we note that the signal is attenuated by the loss coefficient *loss* from the input port to the cavity and amplified by the gain coefficient *gain* by the HEMT amplifier from the cavity to the output port. Consider the voltage

$$V_\mathrm{cav} = I_\mathrm{0,eq} \left(i\omega C + \frac{1}{i\omega L} + \frac{1}{R} + \frac{1}{R_\mathrm{L,eq}} \right)^{-1} \tag{4.33}$$

in the cavity, which can be related to the voltage V_0 at the radio-frequency source by plugging the previously obtained expressions for the individual lumped-element components, both for the reflection and for the transmission cavity. Further, the cavity voltage can be related to the voltage at the amplifier V_amp by taking into account that V_amp is

by the amount $R_{\mathrm{L}}/(R_{\mathrm{L}} + \frac{1}{i\omega C_{\mathrm{ext}}})$ smaller than V_{cav}. A derivation analogue to the one given in [97], section 2.2, yields the relations between the voltages. From the total energy stored in the reactive components of the cavity

$$E = \frac{1}{2}CV_{\mathrm{cav,rms}}^2 + \frac{1}{2}LI_{\mathrm{cav,rms}}^2 = \frac{1}{2}CV_{\mathrm{cav}}^2, \tag{4.34}$$

we establish the relation between the energy inside the cavity and the input power

$$E_{\mathrm{cav}} = P_{\mathrm{in}} \cdot loss \cdot \frac{2A}{\kappa_{\mathrm{ext}}} \frac{\kappa_{\mathrm{ext}}^2}{\kappa^2 + 4\Delta\omega^2}. \tag{4.35}$$

Here, the subscript *rms* denotes time-averaged magnitudes and $A = 2$ ($A = 1$) applies for the reflection (transmission) cavity. The equivalent relation for the output power

$$E_{\mathrm{cav}} = \frac{B}{\kappa_{\mathrm{ext}}} \frac{P_{\mathrm{out}}}{gain} \tag{4.36}$$

results from the consideration that the SMC emits the power $E_{\mathrm{cav}}\kappa_{\mathrm{ext}}/B$ from the coupling capacitor into the output mode of the transmission line. $B = 1$ ($B = 2$) corresponds to the reflection (transmission) cavity. The output power as a function of the input power is given by

$$P_{\mathrm{out}} = P_{\mathrm{in}} \cdot gain \cdot loss \cdot \frac{D \cdot \kappa_{\mathrm{ext}}^2}{\kappa^2 + 4\Delta\omega^2} \tag{4.37}$$

with $D = 4$ ($D = 1$) for the reflection (transmission) cavity.

4.2 Mechanical interaction with the cavity field

4.2.1 Electromechanical interaction

In the microwave domain, the interaction between the cavity mode and the motion of the nanomechanical resonator is modeled by including a position dependent capacitance into the lumped-element model. For small displacements compared to the distance d_0 between the cavity electrode and the circular mechanical resonator (parallel plate approximation) we can approximate

$$C_{\mathrm{m}}(z) = C_{\mathrm{m}}(0) + \frac{\partial C_{\mathrm{m}}}{\partial z} z_0 \cos(\omega_{\mathrm{m}} t + \phi). \tag{4.38}$$

The modulation of the capacitance translates into a modulation of the cavity resonance frequency due to $C_{\mathrm{tot}} = C + C_{\mathrm{ext}} + C_{\mathrm{m}}$ and $\omega_{\mathrm{c}} = 1/\sqrt{LC_{\mathrm{tot}}}$, and we have

$$\frac{\partial \omega_{\mathrm{c}}}{\partial z} = -\frac{\omega_{\mathrm{c}}}{2C_{\mathrm{tot}}} \frac{\partial C_{\mathrm{m}}}{\partial z}. \tag{4.39}$$

This results in a time-dependent cavity frequency

$$\omega_{\mathrm{c}}(t) = \omega_{\mathrm{c}} \cdot (1 - \frac{1}{2C_{\mathrm{tot}}} \frac{\partial C_{\mathrm{m}}}{\partial z} z_0 \cos(\omega_{\mathrm{m}} t + \phi)) \tag{4.40}$$

suggesting a time-domain measurement of the oscillation, which should map the oscillation of the nanomechanical resonator. However, in our experiment, the mechanical frequency

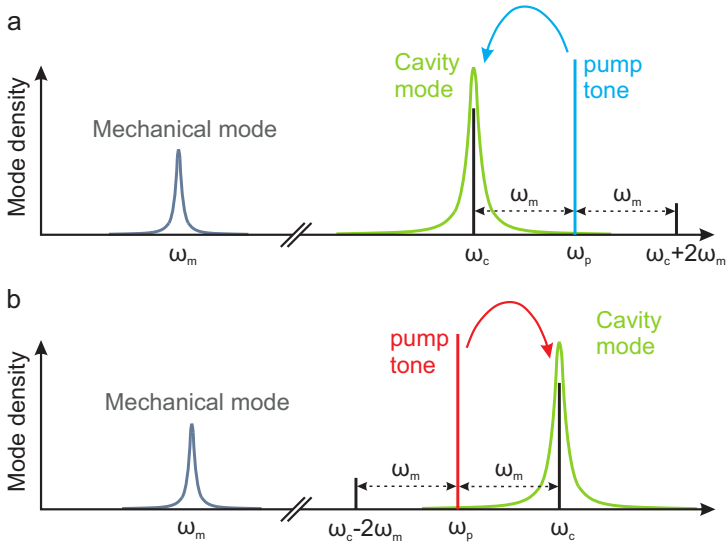

Figure 4.7: **Electromechanical interaction in the frequency domain.** (**a**) The cavity pump tone is applied on the blue sideband at $\omega_\mathrm{p} = \omega_\mathrm{c} + \omega_\mathrm{m}$. The interaction between the mechanical mode and the cavity mode creates sidebands at ω_c and $\omega_\mathrm{c} + 2\omega_\mathrm{m}$. Due to the cavity line shape the sideband at ω_c is resonantly enhanced and the upper sideband is suppressed (in the resolved sideband limit). (**b**) The cavity is pumped on the red sideband at $\omega_\mathrm{p} = \omega_\mathrm{c} - \omega_\mathrm{m}$. Similar to **a**, the sideband at ω_c is enhanced and the sideband at $\omega_\mathrm{c} - 2\omega_\mathrm{m}$ is suppressed.

is much larger than the cavity line width $\kappa \ll \omega_\mathrm{m}$ (sideband resolved limit) and thus the cavity can not follow the mechanical motion.

The analysis of the nanomechanical resonator motion is performed in the frequency domain. Our analysis assumes that the system response contains terms $\sim \cos(\omega_\mathrm{m} t)\cos(\omega_\mathrm{p} t)$ with ω_p the frequency of the cavity pump tone. This leads to the generation of sidebands at $\omega_\mathrm{p} \pm \omega_\mathrm{m}$. We want to restrict the pump frequency to values $\omega_\mathrm{p} = \omega_\mathrm{c} - (+)\,\omega_\mathrm{m}$ since, in this case, the upper (lower) sideband of the pump falls onto the cavity frequency and thus is resonantly enhanced (see Fig. 4.7). The sidebands at $\omega_\mathrm{c} \pm 2\omega_\mathrm{m}$ are suppressed due to the cavity line shape. A simple circuit analysis as the one presented in [97], section 2.4, yields the output power at ω_c

$$P_\mathrm{out}(\omega_\mathrm{c}) = P_\mathrm{in}(\omega_\mathrm{p}) \cdot loss(\omega_\mathrm{p}) \cdot gain(\omega_\mathrm{c}) \cdot \left(\frac{1}{\kappa}\frac{\partial \omega_\mathrm{c}}{\partial z}\right)^2 \cdot 2\left\langle z^2 \right\rangle \frac{D \cdot \kappa_\mathrm{ext}^2}{\kappa^2 + 4(\omega_\mathrm{p} - \omega_\mathrm{c})^2} \qquad (4.41)$$

where, as before, $D = 4$ ($D = 1$) for the reflection (transmission) cavity. This equation can be used to precisely relate the measured output power to the time averaged mechanical deflection $\left\langle z^2 \right\rangle$ of the effective mass motion.

4.2.2 Radiation pressure interaction

The modulation of the cavity frequency by the mechanical resonator leads to modulation of the circulating intra cavity power [99] (see Fig. 4.8). Let us consider an optical cavity whose one end mirror is oscillating. The intra cavity field exerts a radiation pressure force

$F_{\mathrm{rad}} = -\frac{\partial \hat{H}_{\mathrm{int}}}{\partial z}$ onto the mechanical resonator, with $\hat{H}_{\mathrm{int}}$ describing the optomechanical interaction (see below). The cavity decay time $1/\kappa$ introduces a retardation between the modulation of the intra cavity power and the mechanical motion. The in-phase component changes the frequency of the mechanical resonator, also called optical spring effect, and the out-of-phase component changes the mechanical damping [97]. When $\omega_{\mathrm{p}} < \omega_{\mathrm{c}}$ the work on the mechanical resonator over one oscillation cycle is negative. The mechanical motion is damped and cooled. When on the other hand $\omega_{\mathrm{p}} > \omega_{\mathrm{c}}$ the work is positive and the motion is amplified and heated. We discuss both phenomena using a Hamiltonian formulation in the following.

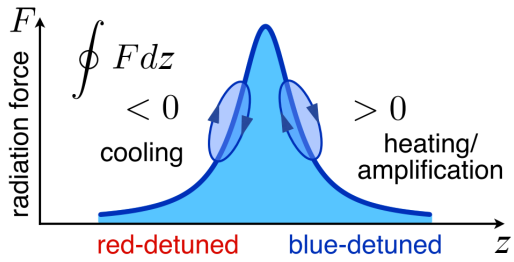

Figure 4.8: **Force-displacement diagram of the radiation pressure force.** The work done by the radiation force on the mechanical mode is denoted as the path integral over one oscillation cycle. The Lorentzian denotes the cavity resonance. On the red side of the resonance the work is negative and on the blue side positive (see text). The panel is adapted from [45].

In the quantum mechanical description, the radiation mode and the mechanical mode are approximated by harmonic oscillators. The Hamiltonian of the dispersively coupled system is given by [100, 38, 45]

$$\hat{H}_0 = \hbar\omega_{\mathrm{c}}\hat{a}^\dagger\hat{a} + \underbrace{\hbar g_0 \hat{a}^\dagger\hat{a}(\hat{b}^\dagger + \hat{b})}_{\hat{H}_{\mathrm{int}}} + \hbar\omega_{\mathrm{m}}\hat{b}^\dagger\hat{b} \tag{4.42}$$

where $\hat{a}^\dagger$ ($\hat{a}$) denote the raising (lowering) operator of the electromagnetic mode and $\hat{b}^\dagger$ ($\hat{b}$) the operators of the mechanical mode. Here, we have introduced the vacuum optomechanical coupling strength $g_0 = G_0 z_{\mathrm{zp}}$ with $G_0 = \partial\omega_{\mathrm{c}}/\partial z$, and the mechanical zero-point motion amplitude

$$z_{\mathrm{zp}} = \sqrt{\frac{\hbar}{2m_{\mathrm{eff}}\omega_{\mathrm{m}}}}. \tag{4.43}$$

The second term in the sum of the Hamiltonian represents the interaction $\hat{H}_{\mathrm{int}}$. This is the general formulation of the radiation pressure interaction both for an optical cavity with one vibrating end mirror and for a microwave cavity whose capacitance is modulated by a mechanical resonator. In order to linearize the Hamiltonian, we choose to work in a frame rotating at the detuned frequency $\Delta = \omega_{\mathrm{p}} - \omega_{\mathrm{c}}$. Additionally, we shift the normal coordinates $\hat{a} = \bar{\alpha} + \delta\hat{a}$ by a steady state value $\bar{\alpha} = \sqrt{n_{\mathrm{p}}}$, which is parametrized by the intra cavity photon number n_{p}. For $\sqrt{n_{\mathrm{p}}} >> 1$ we have

$$\hat{H}' = -\hbar\Delta\delta\hat{a}^\dagger\delta\hat{a} + \hbar g_0\sqrt{n_{\mathrm{p}}}(\delta\hat{a}^\dagger + \delta\hat{a})(\hat{b}^\dagger + \hat{b}) + \hbar\omega_{\mathrm{m}}\hat{b}^\dagger\hat{b}. \tag{4.44}$$

In the sideband resolved limit ($\kappa \ll \omega_{\mathrm{m}}$), we essentially distinguish between three different detuning regimes $\Delta = 0$ and $\Delta \approx \pm\omega_{\mathrm{m}}$. For $\Delta = 0$ the cavity field acquires a phase shift due to the mechanical motion. This is not practical for $\kappa \ll \omega_{\mathrm{m}}$, as the cavity field can not follow the mechanical motion instantaneously.

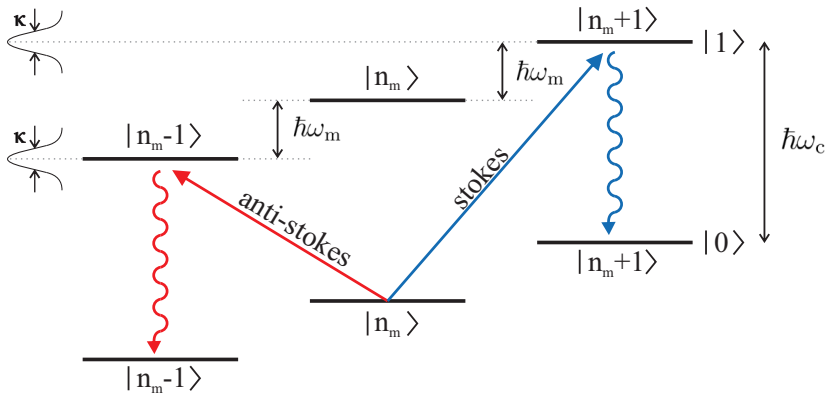

Figure 4.9: **Energy level diagram for anti-Stokes and Stokes scattering between cavity mode and mechanical mode.** The energy levels from left to right represent energy levels with mechanical occupation from $n_{\mathrm{m}} - 1$ to $n_{\mathrm{m}} + 1$. The lower three energy levels correspond to the cavity ground state $|0\rangle$ and the upper three to the cavity excited state $|1\rangle$.

When choosing $\Delta = -\omega_{\mathrm{m}}$ the two harmonic oscillators can interchange quanta of energy since their frequencies are comparable. The Hamiltonian simplifies to a "beam-splitter" interaction

$$\hat{H}_{\mathrm{int}} = \hbar g_0 \sqrt{n_{\mathrm{p}}}(\delta\hat{a}^\dagger\hat{b} + \delta\hat{a}\hat{b}^\dagger). \tag{4.45}$$

This is at the heart of quantum state transfer [101, 53, 57], and sideband cooling [36, 38, 41, 40]. The cooling mechanism is related to the anti-Stokes scattering, that is, the energy up-conversion of a microwave photon from $\hbar\omega_{\mathrm{p}}$ to $\hbar\omega_{\mathrm{c}}$ (in the lab frame) by the absorption of a phonon with the energy $\hbar\omega_{\mathrm{m}}$ (see red arrow in Fig. 4.9). The emission of the photon leaves the cavity in the ground state while the phonon occupation of the mechanical resonator has decreased by one phonon. As expected, the rate of this process is proportional to the effective optomechanical coupling strength $g = g_0\sqrt{n_{\mathrm{p}}}$.

For $\Delta = \omega_{\mathrm{m}}$ we obtain the "two-mode squeezing" Hamiltonian

$$\hat{H}_{\mathrm{int}} = \hbar g_0 \sqrt{n_{\mathrm{p}}}(\delta\hat{a}^\dagger\hat{b}^\dagger + \delta\hat{a}\hat{b}). \tag{4.46}$$

Again, we have two harmonic oscillators with similar frequencies, but instead of exchanging energy they both absorb quanta leading to parametric amplification and to entanglement, respectively, between the mechanical mode and the radiation mode [37, 102, 103, 54]. In the lab frame, this process can be understood as Stokes scattering of a microwave photon from $\hbar\omega_{\mathrm{p}}$ to $\hbar\omega_{\mathrm{c}}$ by emitting a mechanical phonon with the energy $\hbar\omega_{\mathrm{m}}$ (see blue arrow Fig. 4.9). Both the mechanical mode and the cavity are found in their excited state, before either of them decay. If the scattering rate exceeds the mechanical dissipation rate, coherent amplification of the mechanical motion leads to self-induced mechanical oscillations.

4.2.3 Optomechanical scattering rates and transduction

In analogy to section 4.2.1, we wish to formulate the cavity output power as a function of the input power, but in terms of Stokes (-) and anti-Stokes (+) scattering between the photon population in the cavity and the mechanical resonator. The scattering rates can be derived from the linearized Hamiltonian (Eq. 4.42) using the input-output formalism [38, 45]. Solving the obtained equations of motion for the cavity field $\hat{a}$ and the mechanical amplitude $\hat{b}$ in the presence of the optomechanical interaction yields a modified mechanical susceptibility with the effective mechanical line width

$$\Gamma_{\mathrm{eff}} = \Gamma_{\mathrm{m}} + \Gamma_{\mathrm{opt}}. \tag{4.47}$$

The optomechanical scattering rates are given by

$$\Gamma_{\mathrm{opt}} = 4n_{\mathrm{p}}g_0^2 \cdot \Big(\frac{\kappa}{\kappa^2 + 4(\Delta + \omega_{\mathrm{m}})^2} - \frac{\kappa}{\kappa^2 + 4(\Delta - \omega_{\mathrm{m}})^2} \Big). \tag{4.48}$$

From these two equations it is evident that the optomechanical scattering leads to positive damping (anti-Stokes) or to negative damping (Stokes) depending on the detuning Δ. In the case of $\Delta = -\omega_m$ ($\Delta = \omega_{\mathrm{m}}$) anti-Stokes (Stokes) scattering is resonantly enhanced and we have $\Gamma_{\mathrm{opt}} \approx \pm 4n_{\mathrm{p}}g_0^2/\kappa$ in the resolved sideband limit.

When the detuning is small compared to the cavity frequency ($\Delta \ll \omega_{\mathrm{c}}, \omega_{\mathrm{p}}$) we may relate the energy inside the cavity to the photon population over $E_{\mathrm{cav}} \approx \hbar\omega_{\mathrm{p}} n_{\mathrm{p}}$. Using Eq. 4.35, we obtain the photon population in our setup as a function of P_{in}

$$n_{\mathrm{p}} = \frac{2A}{\hbar\omega_{\mathrm{p}}} P_{\mathrm{in}} \cdot loss \cdot \frac{\kappa_{\mathrm{ext}}}{\kappa^2 + 4(\omega_{\mathrm{p}} - \omega_{\mathrm{c}})^2}. \tag{4.49}$$

Note $A = 2$ ($A = 1$) for the reflection (transmission) cavity.

The anti-Stokes (Stokes) scattering leads to an equilibrium cavity population n_{c} at ω_{c} determined by $n_c\kappa \approx \Gamma_{\mathrm{opt}} n_{\mathrm{m}}$ ($n_c\kappa \approx \Gamma_{\mathrm{opt}}(n_{\mathrm{m}} + 1) \approx \Gamma_{\mathrm{opt}} n_{\mathrm{m}}$ for $n_{\mathrm{m}} \gg 1$) [84] where we have assumed negligible thermal population of the cavity mode. The number of phonons n_{m} is related to the zero-point motion z_{zp} by $n_{\mathrm{m}} \approx \langle z^2 \rangle / 2z_{\mathrm{zp}}^2$. The cavity mode leaks into the output mode of the transmission line with a rate κ_{ext}/B, which results in the detectable output power $P_{\mathrm{out}} = n_{\mathrm{c}}\hbar\omega_{\mathrm{c}}\kappa_{\mathrm{ext}}/B$, Eq. 4.36, and we recover Eq. 4.41. Note $B = 2$ ($B = 1$) for the transmission (reflection) cavity.

Additionally, we can characterize the transduction scheme of our setup i.e. convert the power spectral density $S_{\mathrm{out}} = gain(\omega_{\mathrm{c}}) \cdot S_{\mathrm{N}}$ measured at the output of the cryostat (S_{N} is the PSD at the input of the HEMT) into the displacement spectral density S_{z}. We simplify Eq. 4.41 to

$$P_{\mathrm{out}}(\omega_{\mathrm{c}}) = A \cdot gain(\omega_{\mathrm{c}}) \cdot \hbar\omega_{\mathrm{c}} \cdot \frac{\kappa_{\mathrm{ext}}}{\kappa^2} G_0^2 \langle z^2 \rangle \cdot n_{\mathrm{p}} \tag{4.50}$$

by substituting n_{p} and using the approximation $\omega_{\mathrm{c}} \approx \omega_{\mathrm{p}}$. We use the single-sided definitions of the output power $P_{\mathrm{out}} = \int_0^\infty S_{\mathrm{out}} \frac{d\omega}{2\pi}$ and the averaged mechanical displacement $\langle z^2 \rangle = \int_0^\infty S_{\mathrm{z}} \frac{d\omega}{2\pi}$ to establish the relation between the PSD and the displacement noise

$$S_{\mathrm{z}} = \frac{1}{A} \frac{S_{\mathrm{N}}}{\hbar\omega_{\mathrm{c}}} \frac{z_{\mathrm{zp}}^2\kappa^2}{\kappa_{\mathrm{ext}} g_0^2} \frac{1}{n_{\mathrm{p}}}. \tag{4.51}$$

A takes the value 2 (1) for a reflection (transmission) cavity.

4.2.4 Sideband cooling

The thermo-mechanical occupation of a mechanical mode at frequency ω_m and bath temperature T_bath is given by the Bose-Einstein distribution

$$n_\mathrm{m}^\mathrm{th} = \frac{1}{\exp(\frac{\hbar\omega_\mathrm{m}}{k_\mathrm{B}T_\mathrm{bath}}) - 1}. \tag{4.52}$$

Typical mechanical mode frequencies in the MHz range require temperatures in the sub millikelvin range to enter $n_\mathrm{m}^\mathrm{th} < 1$. Therefore, the mechanical mode must be brought out of equilibrium with its environment.

Classical analysis

Classically, sideband cooling can be understood as the modification of the average mechanical energy $k\left\langle z^2\right\rangle$ due to the enhanced mechanical damping for red sideband detuned pumping $\Delta \approx -\omega_\mathrm{m}$. The radiation pressure force modifies the mechanical susceptibility

$$\chi_\mathrm{eff}(\omega) \approx \frac{1}{m_\mathrm{eff}\cdot(\omega^2 - \omega_\mathrm{m}^2 - i\omega\Gamma_\mathrm{eff})} \tag{4.53}$$

where we have neglected the shift of the mechanical frequency due to the optical spring [45]. Integration of the displacement spectrum (see for comparison Sec. 3.1.2)

$$S_\mathrm{z}(\omega) = \frac{4k_\mathrm{B}T_\mathrm{bath}}{m_\mathrm{eff}} \cdot \frac{\Gamma_\mathrm{m}}{(\omega^2 - \omega_\mathrm{m}^2) + \omega^2\Gamma_\mathrm{eff}^2} \tag{4.54}$$

yields

$$T_\mathrm{eff} = T_\mathrm{bath} \cdot \frac{\Gamma_\mathrm{m}}{\Gamma_\mathrm{m} + \Gamma_\mathrm{opt}}. \tag{4.55}$$

This simple relation quantifies the final temperature T_eff of the mechanical mode as a function of the initial temperature $T_\mathrm{bath} \approx \frac{\hbar\omega_\mathrm{m}}{k_\mathrm{B}} n_\mathrm{m}^\mathrm{th}$ sufficiently well as long as the mode occupation is well above one.

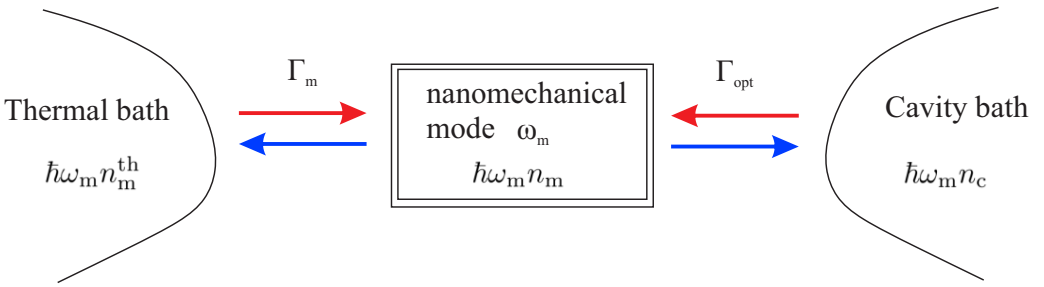

Figure 4.10: **Energy balance between the mechanical mode and its environment.** The mechanical mode emits and absorbs energy from its environment, which is comprised of the thermal bath and a cavity bath. The coupling to the thermal bath is quantified by the intrinsic mechanical dissipation rate Γ_m and the coupling to the cavity bath by the optomechanical scattering rate Γ_opt. The panel is adapted from [97].

Quantum mechanical analysis

In the quantum mechanical description of radiation pressure cooling, the lower bound of the achievable minimum phonon occupation is set by the quantum back-action of the electromagnetic vacuum of the cavity mode onto the mechanical mode [104]. The quantum mechanical approach formalizes the cooling process in terms of energy transition rates between the mechanical mode and its environment [84, 85]. The environment is decomposed of the thermal bath and a cavity bath. The energy absorption of the mechanical mode from a specific bath is given by the energy of the respective bath times the coupling rate to the bath, see Fig. 4.10. The energy emission of the mechanical mode is given by $k_{\mathrm{B}}T_{\mathrm{eff}}\Gamma_{\mathrm{eff}}$. In the weak coupling regime $g < \kappa$, detailed balance of the rate equations yields the final phonon occupation

$$n_{\mathrm{m}} = \frac{\Gamma_{\mathrm{m}} n_{\mathrm{m}}^{\mathrm{th}} + \Gamma_{\mathrm{opt}} n_{\mathrm{c}}}{\Gamma_{\mathrm{m}} + \Gamma_{\mathrm{opt}}} \tag{4.56}$$

where $n_{\mathrm{c}} = n_{\mathrm{min}} + n_{\mathrm{c}}^{\mathrm{th}}(1 + 2n_{\mathrm{min}})$ represents the theoretical lower bound for a given setup [36]. The limit given by n_{c} is essentially composed of two terms. First, the theoretical back-action limit, which for sideband detuned pumping $\Delta = -\omega_{\mathrm{m}}$ is given by $n_{\mathrm{min}} = (\frac{\kappa}{4\omega_{\mathrm{m}}})^2$. This expression represents the main difference to the classical result as it predicts that, in a dispersive coupling scheme, ground-state cooling requires sideband resolution. The second term is the finite thermal occupation $n_{\mathrm{c}}^{\mathrm{th}}$ of the cavity. For optical cavities this occupation is negligible at room temperature, while microwave cavities require dilution refrigeration in order to fulfill $n_{\mathrm{c}}^{\mathrm{th}} \ll 1$. Thermal occupation can also be caused by a noisy signal source, which makes careful filtering of the input lines necessary.

4.2.5 Imprecision versus backaction

In this section, we discuss fundamental quantum mechanical measurement limits of continuous displacement detection. This discussion includes the evaluation of measurement imprecision noise versus quantum back-action noise at zero temperature ($k_{\mathrm{B}}T \ll \hbar\omega_{\mathrm{m}}$). Although a discussion in the classical limit ($k_{\mathrm{B}}T \gg \hbar\omega_{\mathrm{m}}$) is sufficient to describe the results in this dissertation, we provide the quantum mechanical formulation, because our devices are, in principle, capable to reach the quantum back-action limit. Both these limits affect the ability to sense minuscule forces with mechanical resonators, which is discussed in detail in chapter 7.

Quantum mechanical limitations for continuous displacement detection are best illustrated for an optomechanical system that fulfills $\omega_{\mathrm{m}} \ll \kappa$. When the pump is resonant with the cavity $\Delta = 0$, one typically detects the phase shift of the light field that is reflected or transmitted from the cavity in a homodyne and heterodyne detection scheme [46, 48, 45], respectively. The photon shot-noise induces uncertainty on the phase measurement and results in an imprecision proportional to $1/\sqrt{n_{\mathrm{p}}}$. In a weak, continuous measurement the Heisenberg principle poses the limit

$$\Delta X \cdot \Delta Y \geq z_{\mathrm{zp}}^2 \tag{4.57}$$

where X and Y are the quadratures of motion of the trajectory $z(t) = X\cos(\omega_{\mathrm{m}}t) + Y\sin(\omega_{\mathrm{m}}t)$ of the mechanical resonator. An increasingly large photon number decreases

the measurement imprecision but at the same time imparts random momentum on the mechanical resonator associated to the photon shot-noise. This force noise is called quantum back-action noise. Rephrasing the Heisenberg uncertainty principle in terms of imprecision and back-action noise

$$S_{\mathrm{z}}^{\mathrm{imp}}(\omega)S_{\mathrm{F}}^{\mathrm{ba}}(\omega) \geq \hbar^2 \tag{4.58}$$

and denoting $S_{\mathrm{z}}^{\mathrm{add}}$ as the total noise added by the measurement one arrives at the fundamental inequality

$$S_{\mathrm{z}}^{\mathrm{add}}(\omega) \geq S_{\mathrm{z}}^{\mathrm{zp}}(\omega), \tag{4.59}$$

which is called the standard quantum limit (SQL). At the mechanical frequency the SQL fulfills the equality. This highlights the fundamental limit of weak continuous displacement detection. In a quantum non-demolition or back-action evasion measurement this limitation can be overcome by detecting one quadrature with arbitrarily high precision, while placing the increased uncertainty in the other quadrature [49, 51, 52].

We wish to formulate explicit expressions for the noise contributions in our system, that is, for a sideband resolved optomechanical system (reflection cavity) being pumped on the red sideband. For this, we first quantify the white noise background of a displacement measurement (see cf. Eq. 4.51)

$$S_{\mathrm{z}}^{\mathrm{imp}} = \frac{n_{\mathrm{add}} + \frac{1}{2}}{\hbar\omega_{\mathrm{c}}} \frac{z_{\mathrm{zp}}^2\kappa^2}{2\kappa_{\mathrm{ext}}g_0^2} \frac{1}{n_{\mathrm{p}}} = \frac{n_{\mathrm{add}} + \frac{1}{2}}{\hbar\omega_{\mathrm{c}}} \frac{\hbar}{m_{\mathrm{eff}}\omega_{\mathrm{m}}} \frac{\kappa}{\kappa_{\mathrm{ext}}} \frac{1}{\Gamma_{\mathrm{opt}}}. \tag{4.60}$$

The first fraction is a measure for the noise added by the measurement. It includes the vacuum noise of the electromagnetic field and the noise of the amplifier. Typical, commercial amplifiers (HEMT) add about 20-30 quanta at the detection frequency of a few GHz. In the context of cavity QED, the necessity of detecting the state of superconducting quantum bits with no added noise has led to the use of quantum-limited amplifiers with $n_{\mathrm{add}} \approx 0.5$ [105, 106]. These amplifiers are based on Josephson junction arrays incorporated into superconducting microwave cavities. Typically they are operated in a phase-insensitive mode with $n_{\mathrm{add}} \approx 0.5$. Phase-sensitive detection alternatively allows to squeeze the electromagnetic vacuum [107].

We use the mechanical susceptibility at the mechanical frequency $|\chi_{\mathrm{eff}}(\omega_{\mathrm{m}})|^2 = 1/(m_{\mathrm{eff}}\omega_{\mathrm{m}}\Gamma_{\mathrm{eff}})^2$ to derive the imprecision force noise

$$S_{\mathrm{F}}^{\mathrm{imp}} = S_{\mathrm{z}}^{\mathrm{imp}}/|\chi_{\mathrm{eff}}(\omega_{\mathrm{m}})|^2 = \hbar\omega_{\mathrm{m}}m_{\mathrm{eff}} \frac{\kappa}{\kappa_{\mathrm{ext}}} \frac{\Gamma_{\mathrm{eff}}^2}{\Gamma_{\mathrm{opt}}} (n_{\mathrm{add}} + \frac{1}{2}). \tag{4.61}$$

It is instructive to compare the quantum back-action force noise and the imprecision force noise for large photon number. For red sideband detuned pumping, the quantum back-action force noise

$$S_{\mathrm{F}}^{\mathrm{qba}} = 2\hbar\omega_{\mathrm{m}}m_{\mathrm{eff}}\Gamma_{\mathrm{eff}} \approx 2\hbar\omega_{\mathrm{m}}m_{\mathrm{eff}}\Gamma_{\mathrm{opt}} \tag{4.62}$$

is obtained from the quantum fluctuation dissipation theorem [108, 109] by setting the effective mechanical mode occupation to zero (the approximation is valid for large n_{p}). At zero temperature, the force sensitivity is approximated by the sum of the imprecision force noise and the quantum back-action force noise $S_{\mathrm{F}}^{\mathrm{tot}} = S_{\mathrm{F}}^{\mathrm{imp}} + S_{\mathrm{F}}^{\mathrm{qba}}$. In the limit $n_{\mathrm{p}} \to \infty$ we obtain

$$\frac{S_{\mathrm{F}}^{\mathrm{imp}}}{S_{\mathrm{F}}^{\mathrm{qba}}} = \frac{1}{2} \frac{\kappa}{\kappa_{\mathrm{ext}}} (n_{\mathrm{add}} + \frac{1}{2}). \tag{4.63}$$

We conclude, that in an optomechanical system with an overcoupled cavity ($\kappa \approx \kappa_{\mathrm{ext}}$) and a small n_{add} the quantum back-action force noise is detectable despite of the increase of the imprecision force noise at high n_{p} (see Fig. 4.11).

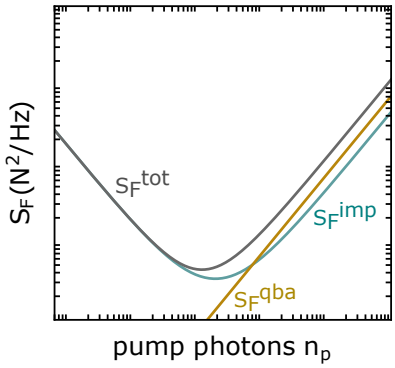

Figure 4.11: **Comparison between imprecision and back-action for $\Delta = -\omega_{\mathrm{m}}$.** Force sensitivity $S_{\mathrm{F}}^{\mathrm{tot}} = S_{\mathrm{F}}^{\mathrm{imp}} + S_{\mathrm{F}}^{\mathrm{qba}}$ (dark grey). The individual components are the imprecision force noise $S_{\mathrm{F}}^{\mathrm{imp}}$ (turquois) and the quantum back-action force noise $S_{\mathrm{F}}^{\mathrm{qba}}$ (dark yellow). The plots are done for a hypothetical device with $\kappa_{\mathrm{ext}} = \frac{4}{5}\kappa$, $n_{\mathrm{add}} = 0.5$ and $T_{\mathrm{bath}} = 0$ (see cf. Fig. 7.1). Note that we have neglected the force noise associated to the zero-point fluctuations, which is much smaller than $S_{\mathrm{F}}^{\mathrm{tot}}$ for the entire n_{p} range.

Chapter 5

Fabrication and cavity engineering

In this chapter we present the fabrication and microwave engineering for the superconducting cavities used in this work. We employ two types of microwave cavities: meandered microstrip (Fig. 5.1) and coplanar waveguide (CPW) (Fig. 5.2). We first discuss the principle design ideas and then proceed to the advantages and disadvantages of the respective cavity design. We also give detailed insight into the fabrication of the structure of the suspended graphene mechanical resonator.

5.1 Superconducting structure

5.1.1 Cavity fabrication and PCB

We use a highly resistive silicon wafer (6 kΩcm) with a 295 nm thick, dry chlorinated thermal oxide from *NOVA wafers*. The wafers are sputtered with 200 nm Nb, followed by optical lithography and ion-milling to define the superconducting cavity, the feed lines and the coarse part of the graphene contact electrodes. These process steps, and the subsequent wafer dicing, are carried out by *STAR cryoelectronics*. The chip dimensions are chosen to be $4.1 \times 7.2\,\mathrm{mm}^2$. We use Nb as a cavity material because of the high critical temperature $T_c = 9.2\,\mathrm{K}$ that allows the cavity to be tested at liquid helium temperature and to sustain large pump fields.

For the experiment, the chips are glued (with poly(methyl methcrylate)(PMMA)) into a printed circuit board (PCB) that is copper coated and contains impedance matched vias to access the input and output ports of the chip. An excavation on the PCB with the height and lateral dimensions of the chip guarantees impedance matching between the PCB and the chip. We adapted the technology of the group of Prof. Andreas Wallraff at ETH Zurich. For further details on the PCB see [110, 111].

5.1.2 Microwave cavity design

When employing superconducting microwave cavities as detectors for nanomechanical motion, the main goal is the maximization of the coupling between the cavity mode

and the mechanical mode. The magnitude of the coupling is governed by the cavity parameters, but also by geometrical aspects and properties of the mechanical resonator. We simulate the cavity parameters including resonance frequency ω_c, total capacitance C_{tot} and coupling capacitance C_{ext} by performing electromagnetic simulations using the software Microwave Office® from NI AWR. The frame for the simulations is set by the thickness $h = 500\,\mu$m of the chip, the dielectric constant $\epsilon_r \approx 11.6$ of Si, the thickness of the thermal oxide, the dielectric constant $\epsilon_r \approx 3.8$ of SiO_2 [110], the thickness of the Nb film and the boundary conditions for a quarter-wavelength cavity. The conductive back-plane of the chip is defined by the PCB.

To optimize the coupling, we wish to minimize the cavity capacitance C and to maximize the cavity frequency $\omega_c = 1/\sqrt{LC_{tot}}$, as can be seen from the single-photon coupling

$$g_0 = z_{zp}\frac{\omega_c}{2C_{tot}}\frac{\partial C_m}{\partial z}. \tag{5.1}$$

For our devices, we have $C_{tot} = C + C_{ext} + C_m \approx C$. When choosing the cavity frequency, one needs to find the right trade-off between frequency and practical operability of the radio-frequency setup. In general, the higher the frequency the higher the requirements for the used materials and the electronic equipment, and the stronger the signal loss between different components due to impedance mismatching. We target a cavity frequency of 7.5 GHz, which is directly related to the amplification band ($4 - 8$ GHz) of our cryogenic HEMT amplifier.

In order to investigate the dependence of the cavity capacitance on different parameters we simulate different cavity geometries. Here we restrict ourselves to microstrip and CPW cavities. We obtain the capacitance

$$C = \Delta C \cdot \frac{(\omega_c - \Delta\omega_c)^2}{2\omega_c\Delta\omega_c - \Delta\omega_c^2} \tag{5.2}$$

from the induced cavity frequency shift $\Delta\omega_c$ when inserting a lumped-element capacitor ΔC between the open end of the cavity and ground. The lumped-element capacitor is chosen much smaller than the cavity capacitance, typically $\Delta C = 1$ fF.

Meandered microstrip cavity

In Fig. 5.1 we show an optical micrograph of a quarter-wavelength meandered microstrip transmission cavity. The cavity conductor is $w = 2\,\mu$m wide, the distance between conductor lines is $8\,\mu$m and the ground plane is designed to have a distance of $s = 200\,\mu$m to the outermost conductor lines (see Fig. 5.1(a)). We choose a narrow cavity conductor to increase the total inductance and reduce the total capacitance for a given resonant frequency. The minimum conductor width is limited by the reliability of the fabrication process. For a desired cavity frequency of $\omega_c/2\pi = 7.5$ GHz we obtain a length of about $L = 9.5$ mm, which results in a total capacitance of $C \approx 85$ fF and a capacitance per length $C' = 18$ pF/m.

The cavity is coupled over a capacitive finger to a transmission line, which is connected to our measurement circuitry (see Fig. 5.1(b)). The transmission line is impedance matched to $R_L = 50\,\Omega$ with dimensions $w = 10\,\mu$m and $s = 8\,\mu$m. We choose two different external quality factors $Q_{ext} = 2000$ and $Q_{ext} = 5000$, respectively. To accomplish these values, the capacitive finger has a length of $190\,\mu$m, a distance to the transmission line

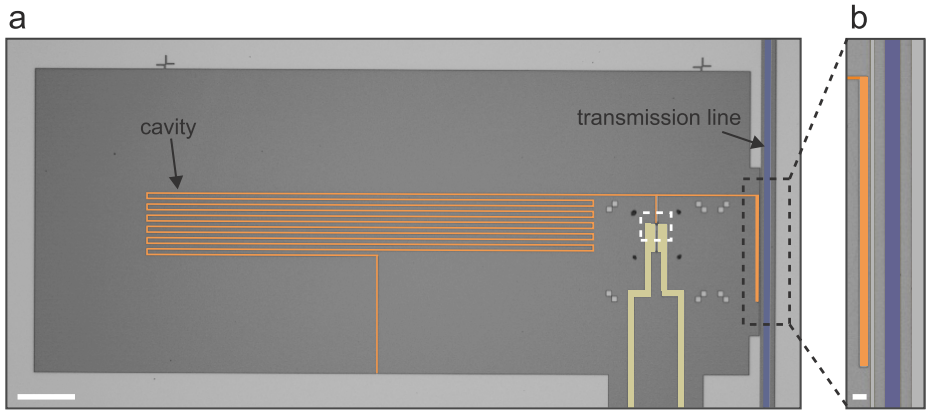

Figure 5.1: **Meandered microstrip transmission cavity.** (**a**) Meandered microstrip cavity (orange) with Nb graphene contacts (yellow) and capacitive coupling to a transmission line (blue/purple). The bright grey areas represent the ground plane of the chip, and the dark grey area the electrically insulating part. The scale bar is 100 μm. (**b**) Zoom-in into region marked by black dashed rectangle in **a**. The capacitive finger (orange) couples the cavity to the transmission line. In this example, the finger has a width of 6 μm corresponding to an external quality factor of $Q_{\text{ext}} = 2000$. The scale bar is 10 μm.

of 14 μm, and a width of 6 μm and 2 μm, respectively. The main motivation for choosing these rather low values for Q_{ext} [36, 108, 37] is justified by the goal to fabricate devices that are better than critically coupled $Q_{\text{int}} > Q_{\text{ext}}$. Testing the cavities before graphene deposition at $T = 4\,\text{K}$, in liquid helium, we obtain $Q_{\text{int}} \approx 3000$. Although this value is expected to improve when cooling the cavity to millikelvin temperatures, we use it as an indicator whether a particular cavity has suffered damage during the fabrication process.

While meandered microstrip cavities achieve low cavity capacitance compared to coplanar waveguide cavities [112, 34, 35, 36, 39], CPW features distinct advantages. The electromagnetic field between cavity conductor and ground plane is very well confined at the surface of the device and CPW is more robust against imperfections in the center conductor. These imperfections can be caused during the fabrication of the graphene fine structure and subsequent graphene deposition. The fabrication steps for the graphene structure are carried out on the cavities after the cavity structure is finished (see below). Both the imperfections and the worse confinement of the electromagentic field cause the internal cavity quality factor to strongly vary between samples.

Coplanar waveguide cavity

In Fig. 5.2 appears a microscope image of a coplanar waveguide quarter-wavelength reflection cavity (for a discussion on the additional ports, see below). The center conductor measures a width of $w = 10\,\mu$m, distance to the ground plane of $s = 100\,\mu$m and a length of $L = 4\,$mm. Compared to standard CPW cavities [112, 35, 39], we choose a large gap between center conductor and ground plane. Although this reduces some of the benefit of using CPW, the cavities experience only a minimum increase in their capacitance $C \approx 130\,\text{fF}$ ($C' = 65\,\text{pF/m}$) compared to meandered microstrip. In general, one has to find the right trade-off between low cavity capacitance and a well defined electromagnetic

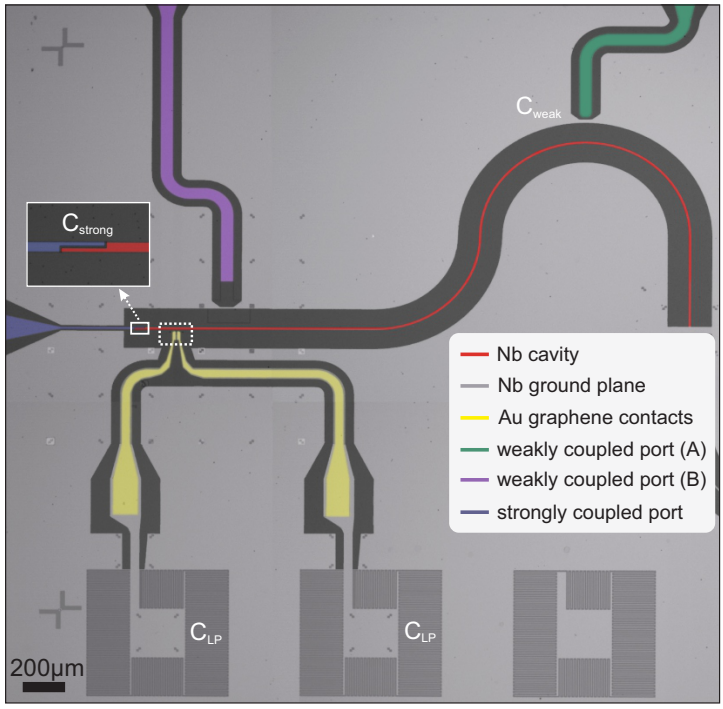

Figure 5.2: **Coplanar waveguide reflection cavity.** (**c**) Superconducting CPW cavity (red line) with coupling ports and graphene contact electrodes (yellow). On-chip capacitors $C_{\mathrm{LP}} \approx 1-2$ pF between the graphene contact electrodes and the ground reduce the internal loss of the cavity. In a reflection measurement, the cavity is probed using the strongly coupled port (blue). In a transmission measurement, the weakly coupled port is used as the input (C_{weak}) and the strongly coupled port as the output (C_{strong}). Depending on the particular device the weakly coupled input port is either the purple or the green port.

field distribution between center conductor and ground plane, which is usually accompanied by an improved internal cavity quality factor. Another advantage of choosing a large gap manifests itself in the fact that the final cavity-graphene device is immune against short-circuiting by graphene flakes. This is a crucial advantage as our graphene transfer technique involves transferring not only the target graphene flake, but also several neighboring flakes that are nearby on the PMMA membrane (see below).

Coplanar waveguide chip layout

We have implemented a few modifications to the design of the CPW to ensure compatibility with a Josephson parametric amplifier (JPA) readout and to improve the internal quality factor of the cavity. For a JPA compatible readout, the cavity is capacitively connected to both a weakly coupled input port and a strongly coupled output port 5.2. This layout prevents the saturation of the amplifier by the strong pump tone typically at $\omega_{\mathrm{p}} = \omega_{\mathrm{c}} - \omega_{\mathrm{m}}$ in a transmission measurement configuration. That is, the pump signal is attenuated by the cavity by $\approx 40\,\mathrm{dB}$. We choose the coupling rate of the weakly coupled

port much smaller than the coupling rate of the strongly coupled port so that we can neglect the output signal loss over the weakly coupled port (see Sec. 8.6.3). The separation between the weak port (green in Fig. 5.2(c)) and the strong port (blue) is large in order to reduce residual coupling between the input and output ports.

In order to reduce internal losses of the cavity over the graphene electrodes, we fabricate capacitors with $C_{\mathrm{LP}} \approx 1 - 2\,\mathrm{pF}$ to the ground plane of the chip at the end of the graphene electrodes. The coupling capacitors are necessary, because parasitic capacitive coupling between the cavity counter electrode and the graphene contacts causes additional internal cavity loss once the graphene contacts are connected to resistive DC electronics outside the chip. These capacitors effectively convert the graphene contacts into a ground plane for the cavity for frequencies above a certain threshold. We choose the threshold to be on the order of 1 GHz in order not to loose the ability to drive the mechanical motion with frequencies on the order of $10 - 100\,\mathrm{MHz}$. With this modification we observe an improvement of Q_{int} by a factor up to 10 for coupled graphene-cavity devices resulting in internal quality factors of up to $Q_{\mathrm{int}} = 10,000$.

In conclusion, the cavities that have shown the best performance when operated with graphene are CPW cavities with a center conductor-ground plane distance of 100 μm and with capacitor pads at the graphene contacts.

5.2 Graphene structure

5.2.1 Fabrication of graphene contacts and counter electrode

The fine structure of the device, shown in Figs. 5.3(a,b), consists of the cavity counter electrode and the support electrodes used later on to anchor the graphene flake. The fabrication of this fine structure is carried out with electron-beam lithography (EBL) and reactive-ion etching (RIE). In a first EBL/RIE step, the cavity counter electrode is separated from the support electrodes. As a mask for etching, we use 50-60 nm aluminum (Al). The Al-mask is structured with EBL using PMMA and etched in 0.2% Tetra-Methyl-Ammonium-Hydroxide (TMAH) diluted in H_2O. Unmasked areas are cleaned from Al-residues with 30 s ion-milling in an argon (Ar) atmosphere. The Nb is etched with RIE in a 10 mTorr SF_6/Ar atmosphere with a radio frequency (RF) power of 100 W. In a second EBL/RIE step the cavity counter electrode is thinned down, such that the height difference between the cavity counter electrode and the support electrodes equals d_0. Optionally, we evaporate 3/40 nm of Cr/Au onto the Nb lines to connect the graphene flake to normal metal contacts (yellow in Fig. 5.2).

5.2.2 Graphene transfer

To position the graphene flake on the fine structure of the superconducting cavity we employ a PMMA supported transfer technique pioneered at Columbia [113] (see Fig. 5.4). For this, we exfoliate graphene sheets from large graphite crystals onto a Si chip covered by a polymer film consisting of 100 nm polyvinyl alcohol (PVA) and 200 nm PMMA 495K (Fig. 5.4(b)). For the exfoliation of the devices we use either Scotch Tape or polydimethylsiloxane (PDMS) (see device parameters summary in chapters 6-8). PDMS exfoliated graphene flakes show less residues on the graphene surface after exfoliation, as we have observed by AFM imaging. The thickness of the PVA/PMMA film is optimized to

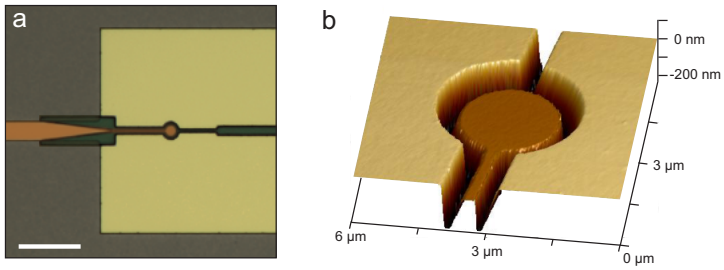

Figure 5.3: **Graphene contacts and cavity counter electrode.** (**a**) False-color optical micrograph of the fine structure of the device marked by the white dotted rectangles in Figs. 5.1 and 5.2, respectively. The graphene contacts are marked as yellow areas and the cavity electrode is marked in orange. Dark grey and dark green areas are electrically insulating. The scale bar is 10 μm. (**b**) AFM image of the fine structure of the device. The circle defined by the edge of the contact electrodes (beige) defines the suspended area of the graphene membrane. The step height between the contacts and the cavity counter electrode (light brown) is d_0.

give the largest optical contrast of graphene flakes in an optical microscope (Fig. 5.4(b)). In particular, it allows to calibrate the number of layers of the graphene flake [114, 115]. The solvability of PVA in water is used to separate the Si chip from the PMMA with the graphene (Figs. 5.4(c-e)). Using a brass slide with a volcano-shaped hole, the membrane is fished from the water and dried on a hotplate (Fig. 5.4(f)). When drying, the PMMA membrane gets uniformly stretched across the volcano hole (Fig. 5.4(g)). By mounting the slide upside down into a micromanipulator, the graphene sheet can be aligned and transferred onto the pre-patterned superconducting cavity structure (Figs. 5.4(h) and 5.5(a)). To improve the attachment of the graphene flake to its support, it was shown that it is important to clamp the graphene membrane on the two sides of its surface [67]. For this, we crosslink part of the transferred PMMA with a 10,000 μC/cm^2 electron beam dose (Fig. 5.5(b)). The unexposed PMMA is removed in 80°C hot N-Methyl-2-pyrrolidone (NMP), followed by critical point drying of the device. As a result, the graphene is firmly sandwiched between the support electrode and the cross-linked PMMA (Fig. 5.5(c)). Using this technique the graphene sheet is less likely to collapse against its counter electrode. This allows us to increase the yield of the device fabrication. We have successfully lowered the separation to $d_0 = 85$ nm for a 3.5 μm diameter graphene resonator, which is among the best diameter-separation ratios reported for graphene resonators [117, 118]. In addition, the strong attachment between the graphene and its support allows us to electrostatically tune the equilibrium position by a large amount, as we will see in the following chapters.

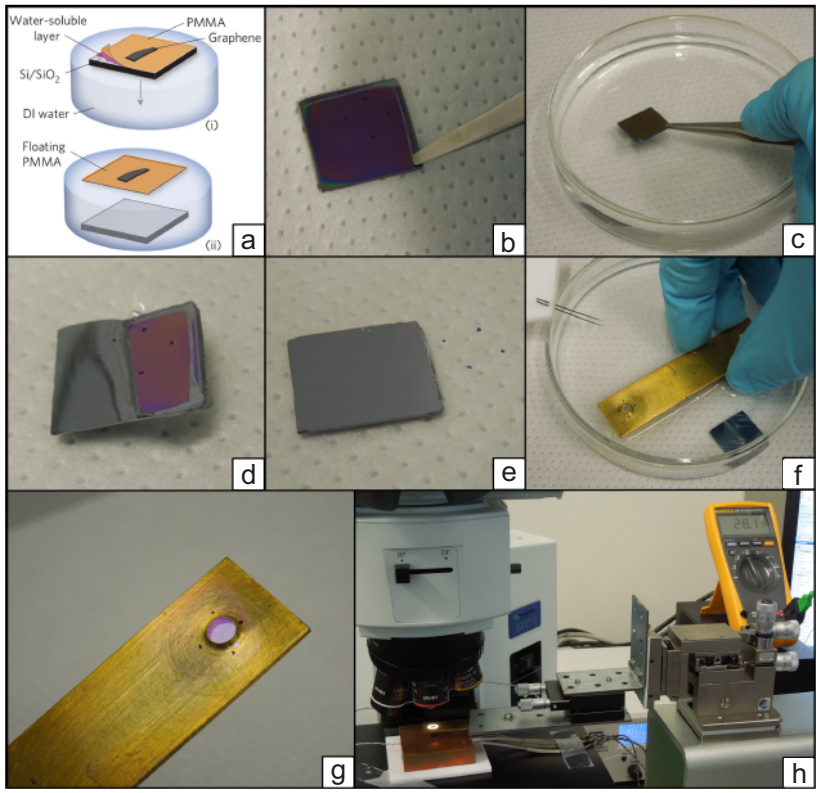

Figure 5.4: **PVA-PMMA based graphene transfer process.** (**a**) Schematic of PMMA membrane removal from Si chip by dissolving PVA in water. The graphene flake is on top of the PMMA membrane. Panel is adapted from [113]. (**b**) Si chip with 100 nm PVA and 200 nm PMMA layer. The thickness of both polymers is chosen such that the color contrast is similar to 285 nm SiO_2. (**c**) The chip with both polymers and graphene on top is put into water. As long as the PVA is not dissolved the chip keeps floating. (**d**) The PVA is slowly dissolving and the PMMA separates from the chip. (**e**) Floating PMMA membrane (4 blue points) on the water surface. (**f**) Fishing of the PMMA membrane using a brass slide with a volcano shaped hole. (**g**) Stretched PMMA membrane over volcano hole. (**h**) Transfer setup with optical microscope, micromanipulator and copper-block heater. Figure is adapted from [116]

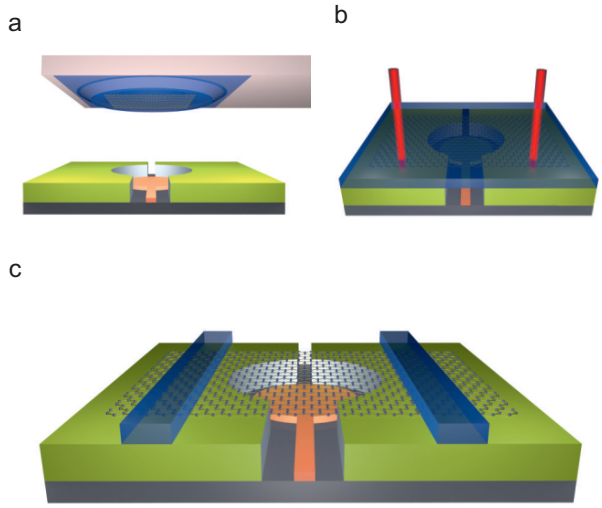

Figure 5.5: **Fabrication process for PMMA-clamped graphene mechanical resonator.** (**a**) Transfer of graphene with PMMA (blue) onto predefined structure (yellow/green, gray). (**b**) Cross-linking part of the transfered PMMA by electron-beam overexposure (red). (**c**) Schematic of the final device.

Chapter 6

Coupling graphene mechanical resonators to superconducting microwave cavities

Thid chapter is published in parts in:

Coupling graphene mechanical resonators to superconducting microwave cavities
P. Weber[1], J. Güttinger[1], I. Tsioutsios, D. E. Chang and A. Bachtold
Nano Letters 14, 2854 (2014)

In this chapter, we study high-Q graphene mechanical resonators coupled to superconducting microwave cavities. After a short introduction on optomechanical systems we motivate the implementation of graphene into a microwave cavity optomechanics scheme. We provide a discussion on the parameter engineering of coupled graphene-cavity devices followed by the characterization of the microwave cavity. We study the mechanical properties of the circular graphene resonators by investigating the driven mechanical vibrations. This includes the gate voltage dependence of the resonant frequency, of the static equilibrium position, and of the optomechanical coupling. Before we conclude the chapter, we study the non-linear mechanical properties of graphene mechanical resonators whose static equilibrium position is tuned by an applied gate voltage.

6.1 Introduction

Mechanical resonators based on individual nanotubes and graphene flakes have outstanding properties. Their masses are ultra-low, their quality factors can be remarkably high, the resonance frequencies are widely tunable, and their equilibrium positions can be varied by a large amount. As a result, the resonators can be used as sensors of mass [119, 19] and force [27, 20, 120] with unprecedented sensitivities, and they can be employed as parametric amplifiers [74] and as tunable oscillators [121, 74, 75]. Thus far, all these scientific applications are accomplished in the classical regime.

[1]Equal contribution

Reaching the quantum regime with mechanical resonators has attracted considerable interest [122, 45]. So far, a handful of groups have been successful in this quest by demonstrating that the number of vibrational quanta n_{m} can be lowered below one. While the first demonstration was achieved by cooling a piezoelectric gigahertz resonator in a dilution refrigerator to millikelvin temperatures [7], the majority of the approaches used radiation pressure cooling of the mechanical mode [38, 41, 49, 51, 52, 104]. The first, and two most prominent examples used (i) a superconducting LC-cavity whose capacitance consists of a mechanically vibrating aluminum membrane [38], and (ii) a photonic crystal that allows for the coexistence of optical and acoustic modes in a nanobeam cavity [41]. Additionally, there is a rich variety of new types of optomechanical and electromechanical devices, the goal being to explore new scientific and technological applications when these devices will enter the quantum regime. These include levitating particles [123, 124, 125], optically trapped cantilevers [126], and heavy pillars [127] to test the foundations of quantum mechanics; metal coated silicon nitride membranes to coherently convert radio-frequency photons to visible photons [101, 57]; microdisks and nanopillars to boost the single-photon coupling and to enter the ultra strong coupling regime [128, 129]. In this context, the unique properties of nanotube and graphene resonators are very interesting.

Although nanotubes and graphene have exceptional properties, an outstanding challenge in approaching the quantum regime has been the development of efficient coupling to external elements, which would enable motional readout and manipulation. For example, while graphene has been coupled to an optical cavity [28], the 2.3% optical absorption of graphene makes it extremely challenging to reach the quantum regime, due to heating of the graphene and quenching of the optical cavity finesse. Here, we employ a different strategy, which is to couple the mechanical resonator capacitively to a superconducting cavity [34, 35, 36, 108, 37, 39]. This is a promising approach with graphene resonators, because the two-dimensional shape of graphene is ideal for large capacitive coupling.

In this chapter, we report on the integration of a circular graphene resonator with a superconducting microwave cavity. We use a transfer technique to precisely position a high-quality exfoliated graphene flake with respect to a predefined superconducting cavity, as described in detail in Sec. 5.2.2. We develop a reliable method to reduce the separation between the graphene membrane and the cavity by tightly clamping the graphene sheet in between a support electrode and a cross-linked Polymethyl methacrylate (PMMA) structure. We show that this technique allows us to improve the mechanical stability and to achieve high mechanical quality factors. By pumping the cavity on a motional sideband, we are able to sensitively readout the graphene motion. Importantly, by applying a constant voltage V_{g} to the graphene, the properties of the optomechanical device can be dramatically tuned. Namely, large static forces can be produced, allowing to tune the steady-state displacement, the mechanical resonance frequency, the optomechanical coupling, and the mechanical nonlinearities. Such a tunability cannot be achieved in other optomechanical systems.

6.2 Device and setup

Our device (see Figs. 6.1(a-d)) consists of a superconducting microwave cavity, modeled as a LC-circuit with angular frequency $\omega_{\mathrm{c}} = 1/\sqrt{LC_{\mathrm{tot}}} \approx 6.7$ GHz, capacitance $C_{\mathrm{tot}} \approx 90$ fF, inductance $L \approx 6.3$ nH, and characteristic impedance $Z_{\mathrm{c}} = \sqrt{L/C_{\mathrm{tot}}} \approx 260\ \Omega$. The total capacitance $C_{\mathrm{tot}} = C + C_{\mathrm{ext}} + C_{\mathrm{m}}(z)$ effectively consists of a cavity capacitance

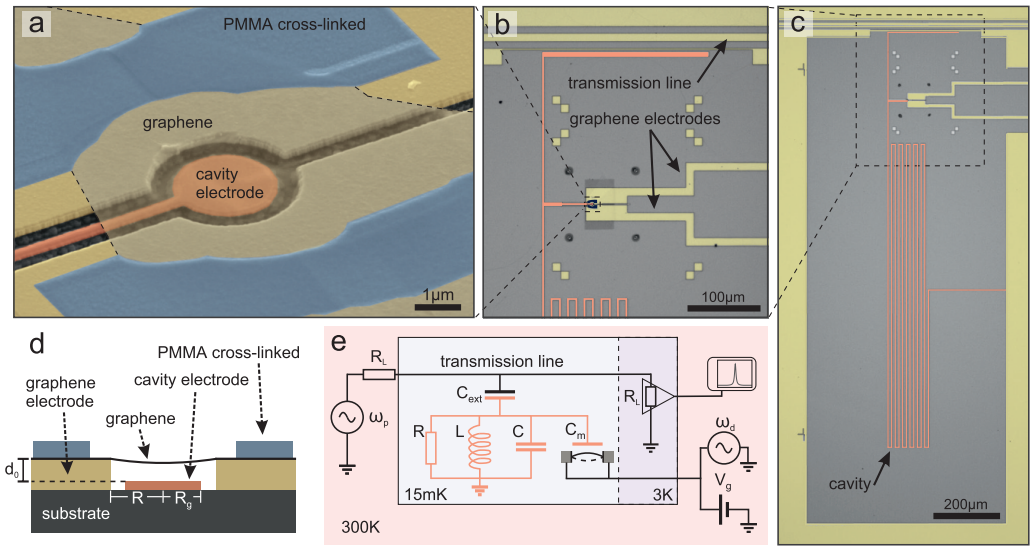

Figure 6.1: **Device and measurement setup.** (**a**) False color SEM image of a circular graphene resonator capacitively coupled to a cavity electrode. The graphene sheet is clamped in between cross-linked PMMA and graphene support electrodes. (**b,c**) Optical microscope images of the superconducting cavity, two electrodes contacting the graphene flake, and a capacitively coupled transmission line. (**d**) Schematic cross-section of the mechanical resonator and the cavity counter electrode. (**e**) Schematic of the measurement circuit. A coherent pump field at ω_p is applied to the transmission line. The graphene mechanical resonator is driven by a field at ω_d and a constant voltage V_g. The microwave signal from the cavity is amplified at 3 K with a HEMT amplifier and recorded at room temperature with a spectrum analyzer. The impedance R_L is 50 Ω.

$C \approx 85$ fF, a contribution $C_{\rm ext} \approx 5$ fF from the external feedline, and importantly, a contribution $C_{\rm m}(z) \approx 0.3 - 0.4$ fF that depends on the graphene position z, which arises from the graphene acting as a moving capacitor plate. A small displacement z therefore produces a shift in $\omega_{\rm c}$ quantified by the coupling parameter $G_0 = \frac{\partial \omega_{\rm c}}{\partial z}$, or more general, by the vacuum optomechanical coupling strength $g_0 = G_0 z_{\rm zp}$. As a result, the interaction between the mechanical resonator and the superconducting cavity can be described by the Hamiltonian $\hat{H}_{\rm int} = \hbar G_0 n_{\rm p} z$ [38]. Central to this work is *(i)* that the low mass of graphene boosts $z_{\rm zp}$ and thus g_0, and *(ii)* that $C_{\rm m}$ and g_0 can be tuned electrostatically with $V_{\rm g}$.

We start with engineering considerations in order to maximize the coupling g_0. When describing $C_{\rm m}$ by a plate capacitor and noting that $C \gg C_{\rm ext} \gg C_{\rm m}(z)$ in our device, we have $g_0 \approx \frac{\omega_{\rm c}}{2C} \frac{\partial C_{\rm m}(z)}{\partial z} z_{\rm zp} \propto \sqrt{\frac{A}{\omega_{\rm m}}} \frac{\omega_{\rm c}}{C d_0^2}$ using $\frac{\partial C_{\rm m}(z)}{\partial z} \propto A/d_0^2$ and $z_{\rm zp} \propto 1/\sqrt{A \omega_{\rm m}}$. Here A is the area of the suspended graphene region and d_0 is the separation between the graphene membrane and its cavity counter electrode. In order to optimize the coupling g_0, it is crucial to minimize both C and d_0. To this end, we utilize a narrow cavity conductor structured in a meander to increase L, while minimizing the capacitance to the ground for a given $\omega_{\rm c}$. In order to be able to tune d with $V_{\rm g}$, we use a cavity that is shorted to ground on one side, allowing for a well defined electrical DC potential. The fundamental mode of the cavity is a quarter wavelength standing wave, with a voltage node at the shorted end and the largest voltage oscillation amplitudes at the open end. The graphene membrane is coupled close to the open end of the cavity to harness the largest cavity fields (see Figs. 6.1(b,c)) [86, 34, 46]. Using this geometry, we achieve a cavity capacitance of $C \approx 90$ fF. This compares favorably with $C = 18$ fF-1 pF in previous studies [34, 35, 36, 38, 37, 39]. Note that the lowest values for C have been achieved in closed-loop cavities, where the mechanical capacitance is incorporated between the two ends of a half-wavelength cavity [38, 37]. In this geometry the two electrodes of the mechanical capacitance are shorted over the cavity, so that no static DC potential can be applied. Compared to the capacitance of a gated half-wavelength cavity [91, 92, 130], the capacitance of a quarter wavelength cavity is lowered by a factor of two.

In order to detect the vibrations of the graphene resonator, we couple the open end of the superconducting cavity to a microwave transmission line through the capacitance $C_{\rm ext}$. The transmission line is used to pump the superconducting cavity at frequency $\omega_{\rm p}/2\pi$ with the power $P_{\rm p,in}$ applied at the cavity input. This relates to the power applied with the radio-frequency source using the *loss* coefficient $P_{\rm p,in} = P_{\rm in} \cdot loss$. The transmission line is also employed to measure the output power $P_{\rm c,out}$ of the cavity at frequency $\omega_{\rm c}/2\pi$. $P_{\rm c,out}$ is amplified at 3 K by a HEMT with a noise temperature of about 2 K and $P_{\rm out} = P_{\rm c,out} \cdot gain$ is measured in a spectrum analyzer (see schematic in Fig. 6.1(e) and Sec. 6.10.2).

We use a graphene resonator with a circular shape. This geometry improves the attachment of the graphene sheet to its support when compared to the doubly-clamped resonator geometry. As further discussed below, a strong attachment of the graphene to its support is crucial to be able to lower d_0. Another advantage of circular graphene resonators over doubly-clamped resonators is that the quality factor tends to be larger [68]. In addition, the mechanical eigenmodes of circular resonators are well defined [68, 131]. In particular, it avoids the formation of modes localized at the edges, which were observed in doubly-clamped resonators [132]. Here we would like to comment as well on the gap between the two support electrodes, which contact the graphene (Figs. 6.1(a,b)). On the one hand this gap allows measuring electrical transport through the graphene, on the

other hand it helps in preventing the collapse of the graphene against the cavity counter electrode during fabrication of the suspended graphene membrane (see Sec. 5.2.2). The openings did not show a significant influence on the mechanical behavior in numerical simulations carried out by Andreas Isacsson and Martin Eriksson at Chalmers.

In this chapter, we present results measured at 15 mK for two different graphene devices, hereafter called devices 1 and 2. Device 1 is a three layer graphene resonator with radius $R = 1.75$ μm and with $d_0 = 95$ nm. The number of layers is determined from optical contrast measurements [114, 115]. The radius of the counter electrode is $R_g = 1.1$ μm (see Fig. 6.1(d)). Device 2 is a four layer graphene resonator with the same membrane radius, $d_0 = 135$ nm and $R_g = 1.25$ μm.

6.3 Characterization of the superconducting cavity

We first characterize the properties of the superconducting cavities, that is, the external coupling and the internal loss by measuring the line shape of the resonance of the cavity. According to Eq. 4.32, the normalized transmission is given by

$$S_{21}(\Delta\omega_c) = 1 - \frac{\kappa_{ext}/\kappa}{1 + 2i\Delta\omega_c/\kappa}. \tag{6.1}$$

with κ the total cavity decay rate and κ_{ext} the external coupling rate of the cavity to the feedline. By measuring the depth and the width of the transmission dip, κ, κ_{ext} and κ_{int} are extracted. In Fig. 6.2 we show the measured transmission spectrum of device 1. For this plot we subtract the background of the measurement containing contributions from the input and the output lines. From a fit of the spectrum to Eq. (6.1) we extract the resonance frequency of the cavity $\omega_c/2\pi = 6.73$ GHz and the external $\kappa_{ext}/2\pi = 2$ MHz and internal $\kappa_{int}/2\pi = 13.2$ MHz decay rates for $V_g = -0.434$ V.

6.3.1 Influence of graphene resistance on internal cavity loss

A detailed analysis of the circuit, which includes a resistance to describe the losses in the graphene flake and the DC connections, shows that this additional resistance contributes roughly 20% to κ_{int}. In Fig. 6.3(a) we show the equivalent circuit of our measurement setup. In order to model dissipation we include a resistor R_m for the loss in the graphene and the DC connection. By using a Norton equivalent circuit [112] we convert all contributions into a parallel equivalent RLC circuit (Fig. 6.3(b)) with $1/R_{tot} = 1/R_{ext,eq} + 1/R + 1/R_{m,eq}$ and $C_{tot} = C_{ext} + C + C_m$. We obtain $1/R_{ext,eq} \approx \omega^2 C_{ext}^2 R_L/2$, $I_{0,eq} = V_p i\omega C_{ext}$, $1/R_{m,eq} \approx \omega^2 C_m^2 R_m$ and we have made use of the fact that in our circuit $\omega C_{ext} R_L \ll 1$ and $\omega^2 R_m^2 C_m^2 \ll 1$. The line width of the equivalent parallel RLC circuit is then given by

$$\kappa = \frac{1}{C_{tot}R_{tot}} = \underbrace{\frac{1}{C_{tot}R_{L,eq}}}_{\kappa_{ext}} + \underbrace{\frac{1}{C_{tot}R}}_{\kappa_{cavity}} + \underbrace{\frac{1}{C_{tot}R_{m,eq}}}_{\kappa_m} \tag{6.2}$$

By substituting the equivalent resistances we get

$$\kappa_{ext} = \frac{\omega_c^2 C_{ext}^2 R_L}{2C_{tot}} \qquad \text{and} \qquad \kappa_m = \frac{\omega_c^2 C_m^2 R_m}{C_{tot}}.$$

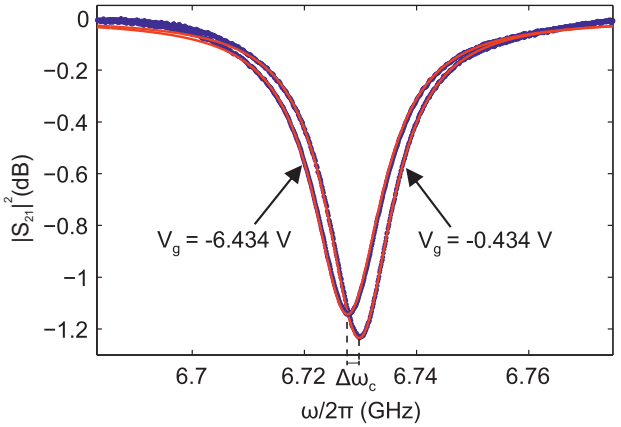

Figure 6.2: **Cavity characterization.** Power transmission $|S_{21}|^2$ through the feedline around the cavity resonance frequency ω_c for two different static voltages applied between the graphene flake and the cavity electrode.

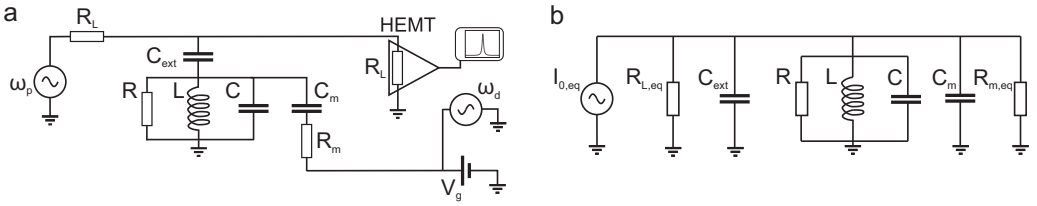

Figure 6.3: **Modelling the graphene resistance.** (**a**) Equivalent circuit of the measurement scheme. (**b**) Norton equivalent circuit where all the contributions are converted into a parallel *RLC* circuit.

From the measured external line width we estimate the coupling capacitance using the above expression to be

$$C_{\mathrm{ext}} = \sqrt{\frac{2C_{\mathrm{tot}}\kappa_{\mathrm{ext}}}{\omega_{\mathrm{c}}^2 R_{\mathrm{L}}}}. \tag{6.3}$$

Using $C_{\mathrm{tot}} = 90$ fF, $\kappa_{\mathrm{ext}}/2\pi = 2$ MHz, $\omega_{\mathrm{c}} = 6.7$ GHz and $R_{\mathrm{L}} = 50\ \Omega$ we get $C_{\mathrm{ext}} = 5$ fF in good agreement with the simulated values of $C_{\mathrm{ext}} = 4$ fF for device 1 and $C_{\mathrm{ext}} = 6$ fF for device 2.

The measured increase of κ with V_{g} in Fig. 6.2 allows to estimate the resistance R_{m} in device 1. Here we note that increasing the voltage V_{g} statically deflects the graphene resonator towards the cavity counter electrode and thus increases the graphene-cavity capacitance. This effect is studied in detail in Sec. 6.6. If we assume that the whole change of the cavity line width is due to the static displacement of the resonator ($\Delta\kappa = \Delta\kappa_{\mathrm{m}}$) we have

$$R_{\mathrm{m}} = \frac{\Delta\kappa_{\mathrm{m}} C_{\mathrm{tot}}}{\omega_{\mathrm{c}}^2 (C_{\mathrm{m}}^2 - C_{\mathrm{m0}}^2)} \tag{6.4}$$

where C_{m0} and C_{m} are the capacitances of the graphene for $V_{\mathrm{g}} \approx 0\,\mathrm{V}$ and $V_{\mathrm{g}} \approx -6\,\mathrm{V}$, respectively. Using $\Delta\kappa = \Delta\kappa_{\mathrm{m}}$, $\Delta\kappa_{\mathrm{m}}/2\pi = 0.8\,\mathrm{MHz}$, $C_{\mathrm{m}} = 0.4\,\mathrm{fF}$ and $C_{\mathrm{m0}} = 0.35\,\mathrm{fF}$

(see Eq. 6.8) we obtain $R_{\rm m} \approx 6\,{\rm k}\Omega$. Here, the change in the capacitance $C_{\rm m}$ is derived from the measured change of the cavity resonance frequency $\Delta\omega_c$. By inserting the value for $R_{\rm m}$ in equation (6.2) we obtain $\kappa_{\rm cavity}/2\pi = 10.8\,{\rm MHz}$ and $\kappa_{\rm m}/2\pi = 2.4\,{\rm MHz}$ with $\kappa_{\rm int} = \kappa_{\rm cavity} + \kappa_{\rm m}$. The high value of $\kappa_{\rm int}$ is therefore mainly attributed to the contamination and imperfections of the cavities. Indeed, we have tested the cavity of devices 1 and 2 at $T = 4.2\,{\rm K}$ before the transfer of the graphene flakes, and we observed larger $\kappa_{\rm int}$ than what we usually observe in devices processed in the same way.

6.4 Readout of driven mechanical motion

We drive the graphene resonator by applying a constant voltage $V_{\rm g}$ and an oscillating voltage $V_{\rm g}^{\rm AC}$ at a frequency $\omega_{\rm d}/2\pi$ close to $\omega_{\rm m}/2\pi$ so that $\omega_{\rm d} = \omega_{\rm c} - \omega_{\rm p}$. As a result, the graphene resonator vibrates at $z(t) = z_0\cos(\omega_{\rm d}t + \phi)$ with ϕ the phase difference between the displacement and the driving force. The cavity output power at $\omega_{\rm c}$, when pumping the cavity on the red sideband, is (see cf. Eq. 4.41)

$$P_{\rm c,out} = P_{\rm p,in}\frac{\kappa_{\rm ext}^2}{\kappa^2 + 4(\omega_{\rm c}-\omega_{\rm p})^2}4\frac{g_0^2}{\kappa^2}\frac{\langle z(t)^2\rangle}{2z_{\rm zp}^2}. \tag{6.5}$$

Figures 6.4(b,c) show the resonance of the driven vibrations for the fundamental modes of devices 1 and 2. Modes at higher frequencies are observed as well, but they are hardly detectable. For device 1 we extract the mechanical quality factor $Q_{\rm m} = \omega_{\rm m}/\Gamma_{\rm m} \approx 10^5$ from the line width of the resonance $\Gamma_{\rm m}/2\pi = 575$ Hz. This $Q_{\rm m}$ is comparable to the largest values reported thus far for graphene resonators [22], showing that our fabrication process does provide us with mechanical resonators of excellent quality. We used $n_{\rm p} = 8000$ photons for this measurement, so that $\Gamma_{\rm opt}/2\pi \approx 0.12$ Hz (with $g_0/2\pi \approx 8\,{\rm Hz}$, see Fig. 6.4(f) and Sec. 6.7). With these parameters, the measurement imprecision, estimated to be $S_{\rm z}^{\rm imp} = (2.55\,{\rm pm}/\sqrt{\rm Hz})^2$, is limited by the noise of the low-temperature HEMT amplifier. With a stronger pump tone $n_{\rm p} = 10^6$ we are able to achieve $S_{\rm z}^{\rm imp} = (230\,{\rm fm}/\sqrt{\rm Hz})^2$. We estimate these values from the detection limit of our readout circuit $S_{\rm N} = -192\,{\rm dBm/Hz}$ (see Sec. 6.10.3) using $S_{\rm z}^{\rm imp} = \frac{S_{\rm N}}{\hbar\omega_{\rm c}}\frac{z_{\rm zp}^2\kappa^2}{\kappa_{\rm ext}g_0^2}\frac{1}{n_{\rm p}}$. For comparison, the height of the resonance in the power spectral density of the thermal motion at 1 K is $(42\,{\rm fm}/\sqrt{\rm Hz})^2$ and $(5\,{\rm fm}/\sqrt{\rm Hz})^2$ at 15 mK. We will improve our displacement resolution (i) by reducing the loss in the cavity (up to a factor 8 improvement in $\sqrt{S_{\rm z,imp}}$), (ii) by using a quantum limited amplifier [107] (up to a factor 10 improvement in $\sqrt{S_{\rm z,imp}}$) and (iii) by increasing the coupling (with a factor 5 improvement in $\sqrt{S_{\rm z,imp}}$ for $g_0/2\pi = 40$ Hz).

In device 2, we measure a quality factor of $Q_{\rm m} = 17.7\times10^3$. We attribute this lower $Q_{\rm m}$ to the fact that the device was imaged in a scanning electron microscope (SEM) before the measurements, where the graphene surface got contaminated by amorphous carbon. This measurement was done with $n_{\rm p} = 4500$ photons, corresponding to $\Gamma_{\rm opt}/2\pi \approx 0.01$ Hz. If we further increase the pump power we observe a reduction of the quality factor. In Fig. 6.5(a) we show a measurement of the quality factor in device 2 as a function of the number of pump photons in the cavity. While the quality factor is roughly constant for $n_{\rm p} < 6000$, $Q_{\rm m}$ decreases for higher pump fields. Upon increasing the temperature of our cryostat $Q_{\rm m}$ also decreases, as shown in Fig. 6.5(b). From the comparison between the two figures we conclude that a pump power of $n_{\rm p} = 10^6$ has the same influence on the

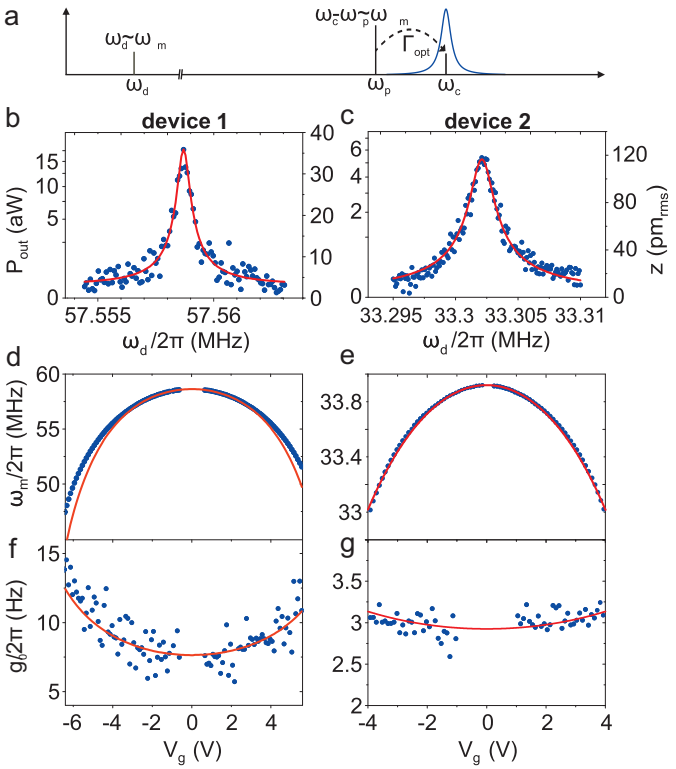

Figure 6.4: **Graphene device characterization.** (**a**) Measurement scheme: If the pump frequency is detuned such that $\omega_\mathrm{p} = \omega_\mathrm{c} - \omega_\mathrm{m}$, anti-Stokes scattering with phonons at rate Γ_opt leads to a detectable photon population at ω_c. (**b,c**) Sideband measurement of the mechanical motion for device 1 with $V_\mathrm{g} = -2.894$ V and $V_\mathrm{g}^\mathrm{AC} = 190$ nV, and for device 2 with $V_\mathrm{g} = 3.405$ V and $V_\mathrm{g}^\mathrm{AC} = 4.3$ μV. Red lines are Lorentzian fits to the data which yield a mechanical quality factor of $Q_\mathrm{m} = 10^5$ in device 1 and $Q_\mathrm{m} = 17.7 \times 10^3$ in device 2. The calculated motional rms amplitude z is plotted on the right scale. (**d,e**) Mechanical resonance frequency as a function of V_g. We have compensated V_g by an offset of 0.434 V for device 1 and 0.395 V for device 2. In addition to capacitive softening, the static deflection z_s of the resonator towards the cavity counter electrode is considered in order to account for the measurement (red line). (**f,g**) Single-photon coupling rate $g_0 = G_0 z_\mathrm{zp}$. By including the static displacement z_s we are able to model the single-photon coupling as a function of V_g (red line).

mechanical resonator as heating the cryostat to 200 mK. In order to minimize the heating it is beneficial to reduce the resistance of the graphene and to improve the heat flow away from the mechanical resonator.

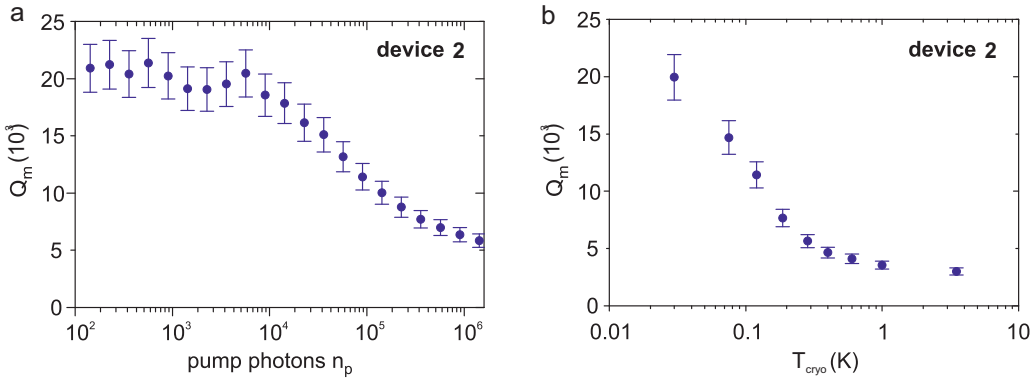

Figure 6.5: **Heating of the mechanical mode in device 2.** (**a**) Mechanical quality factor as a function of cavity pump photon number. (**b**) Mechanical qualtiy factor versus cryostat temperature.

6.5 Gate dependence of mechanical resonance frequency

The resonance frequency decreases upon increasing $|V_g|$ (see Fig. 6.4(d,e)). This reduction of the resonance frequency has been observed previously in graphene resonators under tension [24, 22, 23]. This softening of the resonator is attributed to the change of the restoring potential of the resonator by the capacitive energy [133, 24, 22, 23]. We model the mechanical resonator with a circular membrane under tension [81] to quantify the observed dependence. When neglecting static deflection, the frequency dependence is given by (see Eq. 3.47)

$$\omega_m(V_g) = \sqrt{\frac{4.92Eh\epsilon}{m_{\text{eff}}} - \frac{0.271}{m_{\text{eff}}}\frac{\epsilon_0 \pi R_g^2}{d_0^3}V_g^2}, \tag{6.6}$$

with ϵ the strain in the graphene sheet, $E \approx 1\,\text{TPa}$ the Young's modulus of graphite, $h = n_g \times 0.34\,\text{nm}$ the graphene thickness, and n_g the number of graphene layers. From a fit to the measurements around $V_g = 0$ (in Fig. 6.4(d,e)), we extract the effective mass $m_{\text{eff}} = 13 \cdot 10^{-18}$ kg and the strain $\epsilon = 0.036\%$ for device 1, and $m_{\text{eff}} = 36 \cdot 10^{-18}$ kg and $\epsilon = 0.024\%$ for device 2. The obtained mass for device 1 is $\nu = 2.2$ times larger than the total effective mass of a three-layer graphene device and the mass for device 2 $\nu = 4.5$ times larger than the total effective mass of a four-layer graphene device. The larger ν for device 2 might be attributed to the amorphous carbon deposited during SEM inspection. The tension is intermediate compared to previous measurements, where ϵ ranges from 0.002% to 1% [27, 68, 22, 29].

6.6 Static deflection of the graphene membrane

In order to account for the variation of ω_m for large V_g in Fig. 6.4(d,e), the static deflection of the graphene sheet towards the cavity counter electrode has to be considered. The static displacement of the center of the membrane z_s is given by (see cf. Eq. 3.38)

$$z_s \approx \frac{\epsilon_0 R_g^2}{8Eh\epsilon d_0^2} V_g^2 = c_s V_g^2 \tag{6.7}$$

for small displacement compared to d_0. Although the renormalization of the mechanical frequency due to static displacement cannot be solved exactly, as an approximation we can include z_s in Eq. (6.6) using $d = d_0 - z_s$, with d_0 the separation for $V_g = 0$. We get a good agreement for $\omega_m(V_g)$ between the measurements and theory without any fitting parameter over the V_g range shown in Fig. 6.4(d,e). The effect of z_s on the shift in ω_m is 42% at $V_g = -6\,\mathrm{V}$ for device 1 and 10% at $V_g = 4\,\mathrm{V}$ for device 2. The expected variation of z_s is plotted in Fig. 6.6(a). For device 1, the approximation of small static deflections is well valid up to $V_g \approx 3.5$ V where $z_s = 5\,\mathrm{nm}$ and $2z_s/d = 0.1 \ll 1$. At large V_g we underestimate the static displacement by not including higher order corrections of the electrostatic force. On the other hand we also underestimate the mechanical force when neglecting nonlinear effects as described below. In device 2 $z_s \approx 7.5\,\mathrm{nm}$ with $2z_s/d = 0.1 \ll 1$, which corresponds to $V_g \approx 5$ V. The assumption of constant strain at moderate gate voltages is justified by analysing the strain induced by the static deflection. At $V_g \approx 6$ V the additional strain induced by the static deflection of 10 nm (in device 2) is given by $\epsilon_s = 2 \cdot 10^{-5} \ll \epsilon_{\mathrm{init}}$, significantly smaller than the initial strain.

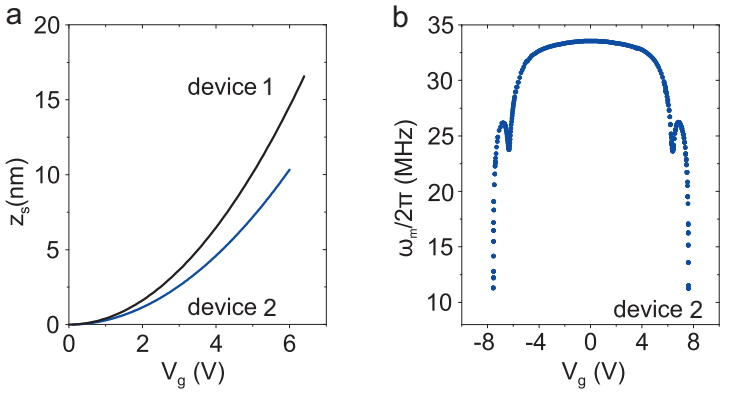

Figure 6.6: **Static displacement and extrem electrostatic softening in device 2.** (**a**) Static displacement of the center of the membrane calculated from Eq. (3.38) with constants $c_s = 0.405\ \mathrm{nm/V^2}$ for device 1 and $c_s = 0.287\ \mathrm{nm/V^2}$ for device 2. (**b**) Mechanical resonance frequency as a function of V_g.

The softening of the graphene resonator becomes enormous upon further increasing V_g, with a reduction of ω_m by a factor of three down to ≈ 10 MHz as shown in Fig. 6.4(b) for device 2. This reduction of ω_m is large compared to that measured in previous works [133, 24, 23]. Such a large reduction is expected when the capacitive force becomes comparable to the restoring force of the resonator. When the two forces are equal, ω_m drops to

zero and the resonator collapses against the counter electrode [134]. Even though further work is needed to understand the quantitative dependence of $\omega_{\rm m}$ on $V_{\rm g}$, it reveals that the graphene resonators we fabricate can bend by a large amount without being ripped apart due to the large induced strain and without sliding with respect to the anchor electrodes.

The static displacement of the graphene sheet also changes the resonance frequency of the microwave cavity upon varying $V_{\rm g}$. As the graphene moves closer to the cavity counter electrode, the total capacitance of the cavity increases, so that the cavity frequency decreases. For $\Delta V_{\rm g} = 6\,{\rm V}$ the observed decrease in the resonance frequency $\Delta\omega_{\rm c}/2\pi \approx 2$ MHz (see Fig. 6.3) is equivalent to a change in cavity capacitance of $\Delta C \approx 50$ aF. The change in resonance frequency can be well explained with an increased graphene-cavity capacitance due to static displacement

$$\Delta C_{\rm m} = \int_0^{2\pi} d\phi \int_0^{R_{\rm g}} r dr \frac{\epsilon_0}{d_0 - \xi_{\rm s}(r)} - C_{\rm m0} \tag{6.8}$$

where $\xi_{\rm s}(r) = z_{\rm s}(V_{\rm g}) \cdot (1 - r^2/R^2)$ is the static mode shape of the pulled down graphene. If we calculate the capacitive change using $z_{\rm s}(V_{\rm g}) = 15$ nm for $V_{\rm g} \approx 6$ V (Fig. 6.6(a)) we obtain $\Delta C_{\rm m} = 49$ aF. This value is in excellent agreement with the value of ΔC estimated from the change in $\omega_{\rm c}$.

6.7 Optomechanical coupling

Our device layout allows us to get large couplings g_0 between the mechanical resonator and the superconducting cavity (Figs. 6.4(f,g)). We extract

$$g_0 = z_{\rm zp} \sqrt{P_{\rm c,out}(\omega_{\rm c}) \frac{\kappa^2}{n_{\rm p} \hbar \omega_{\rm c} \kappa_{\rm ext} \langle z^2 \rangle}} \tag{6.9}$$

from the measurements of the response of driven vibrations at $\omega_{\rm d} = \omega_{\rm m}$ using Eqs. (4.49) and (6.5) where $\langle z(t)^2 \rangle = [\partial_{\rm z} C_{\rm m} \cdot V_{\rm g} V_{\rm g}^{\rm AC} Q_{\rm m}/(m_{\rm eff}\omega_{\rm m}^2)]^2$. Remarkably, g_0 gets larger upon increasing $|V_{\rm g}|$ for device 1. This tunability of g_0 is attributed to the static deflection of the graphene sheet. To model the dependence of $g_0 = G_0 z_{\rm zp}$ on the voltage $V_{\rm g}$, we have to account for the $V_{\rm g}$ dependence of both G_0 and $z_{\rm zp}$. For the estimation of $G_0(V_{\rm g})$ we use the calculated value of the equilibrium position $z_{\rm s}$ (Fig. 6.6(a)) to substitute d_0 by $d = d_0 - z_{\rm s}$ in the calculated graphene-cavity capacitance $C_{\rm m}$

$$G_0(V_{\rm g}) = \frac{\omega_c}{2C_{\rm tot}} \frac{\partial C_{\rm m}(V_{\rm g})}{\partial z} \approx \frac{\omega_c}{2C} \frac{0.433 \epsilon_0 \pi R_{\rm g}^2}{[d_0 - z_{\rm s}(V_{\rm g})]^2}. \tag{6.10}$$

The factor 0.433 is a correction factor that arises from the effective mass modeling when calculating the capacitance $C_{\rm m}$ (see Sec. 3.2.3). The increase of the zero-point motion is accounted for by calculating $z_{\rm zp}$ as a function of $V_{\rm g}$ from the measurement of the resonance frequency $\omega_{\rm m}$ as a function of $V_{\rm g}$ in Figs. 6.4(c,d)

$$z_{\rm zp}(V_{\rm g}) = \sqrt{\frac{\hbar}{2 m_{\rm eff} \omega_{\rm m}(V_{\rm g})}}. \tag{6.11}$$

When incorporating the effect of the static displacement into $C_{\rm m}$, we get a good agreement between the expected $g_0 = \omega_{\rm c}/(2C) \cdot \partial_{\rm z} C_{\rm m}$ and the measurements, using $C = 75$ fF and

100 fF for devices 1 and 2, respectively (red lines in Fig. 6.4(f,g)). These values of C agree well with $C = 90$ fF estimated from simulations. The obtained coupling rates g_0 compare favorably with previous experiments carried out with mechanical resonators made from other materials. Indeed, the coupling was $g_0/2\pi \sim 1$ Hz in works with cavity geometries similar to ours [94, 36, 39]. Larger values were achieved with closed-loop cavities ($g_0/2\pi = 40$ and 210 Hz) but this geometry does not allow one to apply V_g between the mechanical resonator and a counter electrode as discussed above [38, 37].

6.8 Nonlinearities, symmetry breaking

Now, we investigate in device 2 how the strong tunability of the graphene equilibrium position affects the nonlinear response of the mechanical resonator. For this, we measure P_out as a function of ω_d as in Figs. 6.4(b,c) in order to obtain the response of the vibrational amplitude $z_0(\omega_\mathrm{d})$ for large driving forces at different V_g (Figs. 6.7(a-c)). Interestingly, we are able to tune the sign of the Duffing nonlinearity from a hardening behavior at low V_g (Fig. 6.7(a)) to a softening behavior at high V_g (Fig. 6.7(c)). At an intermediate V_g of about 3.4 V, we are able to cancel the Duffing nonlinearity, that is, the resonant frequency remains roughly constant upon varying the driving force (Fig. 6.7(b)). We quantify the Duffing nonlinearity from the critical displacement amplitude z_crit above which the response gets bistable. For a Duffing resonator with linear damping, the effective Duffing constant α_eff is related to z_crit by $\alpha_\mathrm{eff} = \frac{8}{3\sqrt{3}} m_\mathrm{eff}\omega_\mathrm{m}^2/(Q_\mathrm{m} z_\mathrm{crit})$ (see cf. Eq. 3.21). Figure 6.7(d) shows that α_eff is positive at low V_g and becomes negative at large V_g. This dependence can be attributed to the symmetry breaking of the mechanical motion induced by static deflection [135, 136].

To prove this, we consider quadratic and cubic nonlinear terms in the equation of motion (without dissipation and drive)

$$m_\mathrm{eff}\ddot{z}(t) = -m_\mathrm{eff}\omega_m^2 z(t) - \beta_0 z^2(t) - \alpha_0 z^3(t) + F_\mathrm{el} \tag{6.12}$$

with β_0 and α_0 two constants, and $F_\mathrm{el} = \frac{1}{2}\partial_\mathrm{z} C_\mathrm{m} V_\mathrm{g}^2$ the electrostatic force. With the separation ansatz $z(t) = z_\mathrm{s} + z_\mathrm{f}(t)$ and the Taylor-expansion of F_el we get

$$\begin{aligned} m_\mathrm{eff}\ddot{z}_\mathrm{f}(t) \;=\; & -\left[m_\mathrm{eff}\omega_{\mathrm{m},0}^2 z_\mathrm{s} + \beta_0 z_\mathrm{s}^2 + \alpha_0 z_\mathrm{s}^3 - \frac{1}{2}\partial_z C_\mathrm{m}(z_\mathrm{s}) V_\mathrm{g}^2\right] \\ & - \underbrace{\left[m_\mathrm{eff}\omega_{\mathrm{m},0}^2 + 2\beta_0 z_\mathrm{s} + 3\alpha_0 z_\mathrm{s}^2 - \frac{1}{2}\partial_z^2 C_\mathrm{m}(z_\mathrm{s}) V_\mathrm{g}^2\right]}_{k_\mathrm{tot}} z_\mathrm{f}(t) \\ & - \underbrace{\left[\beta_0 + 3\alpha_0 z_\mathrm{s} - \frac{1}{4}\partial_z^3 C_\mathrm{m}(z_\mathrm{s}) V_\mathrm{g}^2\right]}_{\beta_\mathrm{tot}} z_\mathrm{f}^2(t) \\ & - \underbrace{\left[\alpha_0 - \frac{1}{12}\partial_z^4 C_\mathrm{m}(z_\mathrm{s}) V_\mathrm{g}^2\right]}_{\alpha_\mathrm{tot}} z_\mathrm{f}^3(t) \end{aligned}$$

From the first bracket we can estimate the static displacement by neglecting the nonlinear

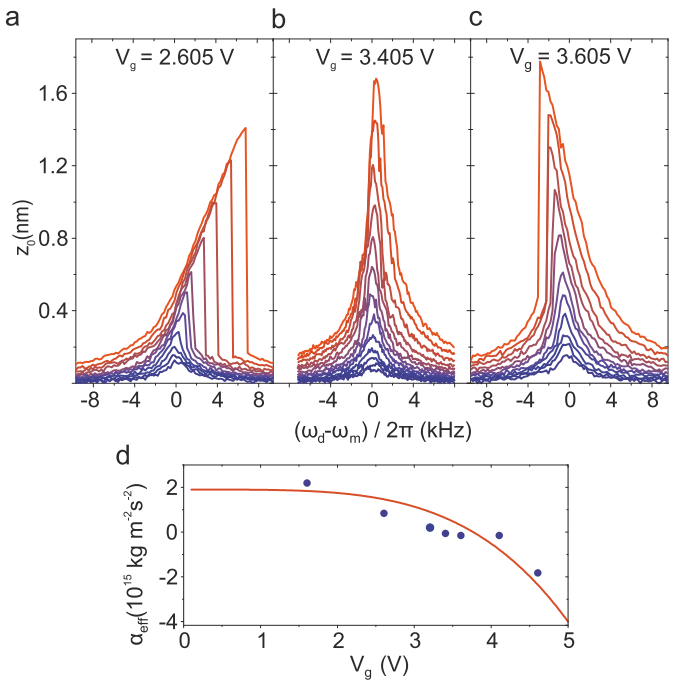

Figure 6.7: **Control of nonlinear behaviour of mechanical vibrations. (a-c)** Dependence of the vibrational amplitude z_0 in device 2 on the drive frequency for different $V_{\mathrm{g}}^{\mathrm{AC}}$ in each plot. In **a** and **c**, $V_{\mathrm{g}}^{\mathrm{AC}}$ = 3 μV - 31 μV. In **b** $V_{\mathrm{g}}^{\mathrm{AC}} = 1.9\mu V - 31\mu V$. The onset of bistability is determined to be at z_{crit} = 360 pm for (a) and at z_{crit} = 900 pm for **c**. (**d**) Effective Duffing parameter α_{eff} as a function of V_{g}. The red line is a plot of Eq. (6.13) with c_{s} = 0.65 nm/V^2 and $\alpha_0 = 1.9 \cdot 10^{15}$ kg·m^{-2}s^{-2}.

contributions and assuming a similar deflection profile as the fundamental oscillation

$$\begin{aligned} z_{\rm s} &\approx \frac{1}{2m_{\rm eff}\omega_{\rm m,0}^2}\partial_z C_{\rm m} V_{\rm g}^2 \\ &\approx \frac{0.433}{2m_{\rm eff}\omega_{\rm m,0}^2}\frac{\epsilon_0 \pi R_g^2}{d^2} V_{\rm g}^2 \\ &= \frac{\epsilon_0 R_{\rm g}^2}{7.21 T d^2} V_{\rm g}^2. \end{aligned}$$

Compared to the result of the direct calculation with the static modeshape in Eq. (3.38) there is a small difference with a factor 7.21 instead of 8 in the denominator. For small nonlinear amplitudes we transform the quadratic and cubic nonlinear terms in a single cubic term [137]

$$\begin{aligned} \alpha_{\rm eff} &\approx \alpha_{\rm tot} - \frac{10}{9}\frac{\beta_{\rm tot}^2}{m_{\rm eff}\omega_m^2} \\ &\approx \alpha_0 - \frac{1}{12}\partial_z^4 C_{\rm m} V_{\rm g}^2 - \frac{10}{9m_{\rm eff}\omega_m^2}\left(3\alpha_0 z_{\rm s} - \frac{1}{4}\partial_z^3 C_{\rm m} V_{\rm g}^2\right)^2 \\ &\approx \alpha_0 - \frac{1}{12}\partial_z^4 C_{\rm m} V_{\rm g}^2 - \frac{10}{144 m_{\rm eff}\omega_m^2}\partial_z^3 C_{\rm m}^2 V_{\rm g}^4 - \frac{10}{m_{\rm eff}\omega_m^2}\alpha_0^2 z_{\rm s}^2 \end{aligned}$$

where α_0 is the duffing nonlinear constant when $V_{\rm g} = 0\,{\rm V}$; α_0 could have a geometrical origin [78]. We assumed that $\partial_z^n C_{\rm m}(z_{\rm s}) \approx \partial_z^n C_{\rm m}(z_{\rm s}=0)$ and that β is small (no symmetry breaking visible at small $V_{\rm g}$). With $\alpha_0 \sim 2\times 10^{15}$ kg s^{-2}m^{-2} and $V_{\rm g} = 5$ V, the second and the third terms of the last equation are $\sim -6\times 10^{12}$kg s^{-2}m^{-2} and $\sim -6\times 10^{11}$kg s^{-2}m^{-2}, respectively. This is much smaller than the fourth term ($\sim -4\times 10^{15}$kg s^{-2}m^{-2}). Hence we can write

$$\alpha_{\rm eff} \approx \alpha_0 - \frac{10}{m_{\rm eff}\omega_m^2}\alpha_0^2 z_{\rm s}^2. \tag{6.13}$$

The fit of Eq. (6.13) to the measurement yields $c_{\rm s} = 0.65$ nm/V^2 and $\alpha_0 = 1.9\cdot 10^{15}$ kgm^{-2}s^{-2} (red line in Fig. 6.7(d)). This value of $c_{\rm s}$ is consistent with that expected from Eq. (3.38). With the obtained α_0 it is also possible to analyze the nonlinear contribution in $k_{\rm tot}$. For $z_{\rm s} = 17$ nm, in device 2, the nonlinear contribution equals the linear contribution as $3\alpha_0 z_{\rm s}^2 = m_{\rm eff}\omega_{\rm m}^2 = 1.6$ kg·s^{-2}. The measured values for the Duffing nonlinearities are within the range of $\alpha_{\rm eff} = 1.74\cdot 10^{12}$ kg·m^{-2}s^{-2} to $7.16\cdot 10^{17}$ kg·m^{-2}s^{-2} observed in other graphene resonators [22, 23] and are compatible with the observation of intermediate strain. The sign change of the Duffing nonlinearity due to static deformation is a unique property of graphene and nanotube resonators [138].

6.9 Conclusions and outlook

The prospects to reach the quantum regime with graphene resonators are promising. For this, it is illustrative to compare the figures of merit achieved here to those reported by Teufel *et al.* [38], which demonstrated ground-state cooling with a superconducting cavity. In the device 1 of our work, we measure $g_0/2\pi \approx 15$ Hz with $n_{\rm p} = 8000$, $\omega_{\rm m}/2\pi \approx 57$ MHz, $Q_{\rm m} = 10^5$ and $\kappa_{\rm int}/2\pi = 13$ MHz, while the parameters of Teufel *et al.* are $g_0/2\pi \approx$

200 Hz, $n_{\mathrm{p}} = 4000$, $\omega_{\mathrm{m}}/2\pi \approx 10\,\mathrm{MHz}$, $Q_{\mathrm{m}} = 3.5\times10^5$ and $\kappa_{\mathrm{int}}/2\pi = 40\,\mathrm{kHz}$. As discussed above, an obvious way to improve κ_{int} is to fabricate cavities with less contamination and imperfections. κ_{int} can then be further reduced by lowering the resistance of the graphene flake. This can be achieved for instance by selecting thicker graphene flakes or electrostatically doping the graphene. Minimizing the graphene resistance, together with increasing the area of the interface between the graphene and the electrodes, is beneficial for diminishing Joule heating at high pump power. In order to increase g_0, we will reduce d further by fabrication and graphene pulling. We should reach $g_0/2\pi \approx 250$ Hz with $d = 30$ nm. An alternative route to increase g_0 is to enhance the coupling using a cooper-pair box [139, 140].

In conclusion, we have reported devices where a graphene resonator is coupled to a superconducting cavity. The tunability of these devices, in combination with the large graphene-cavity coupling, constitutes a promising approach to study quantum motion. The large reduction of the resonance frequency of the graphene resonator observed here is interesting to enhance the zero-point motion and to increase the effect of mechanical nonlinearities [141, 142, 143]. The tunability of the resonance frequency with V_{g} is suitable for parametric amplification and quantum squeezing of mechanical states [144]. In these graphene-cavity devices, the optomechanical coupling can be varied not only with the number of pump photons but also with V_{g}. Interestingly, the tuning of the coupling with V_{g} can be made faster than that with n_{p}, since the inverse of the cavity line width poses an upper limit on how fast the photon number inside the cavity can be changed. Because the mass of graphene is ultra-low, its motion is extremely sensitive to changes in the environment. It will be interesting to couple the quantum vibrations of motion to other degrees of freedom, such as electrons and spins.

6.10 Additional information

6.10.1 Device Parameters

Important parameters of the measured devices are summarized in Table 6.1.

6.10.2 Measurement setup

Figure 6.8 shows a detailed schematic of the measurement setup. We perform the measurements in a Triton 200 dilution refrigerator from Oxford instruments with a base temperature of 15 mK. The RF-lines are UT85-SS-SS coaxial cables from room temperature to the 700 mK stage and superconducting UT85-Nb-Nb coaxial cables from 700 to 15 mK. The input lines are attenuated by cryogenic attenuators to decrease the thermal electromagnetic noise from room temperature. The attenuation is 10 dB at $T = 47\,\mathrm{K}$, 20 dB at $T = 3\,\mathrm{K}$, 6 dB at $T = 700\,\mathrm{mK}$ and 20 dB at $T = 15\,\mathrm{mK}$ where we use for the last attenuation step an Arra 5191-20 20 dB directional coupler to physically interrupt the central part of the coaxial line [38]. The circulators are CTH0408KC from Quinstar. We use two circulators at the output line to shield the sample from the thermal noise of the higher temperature stages.

The source used to apply the constant voltage V_{g} is a Keithley 2400. The DC line is filtered with π-filters at room temperature and a custom made RC filter at the mixing chamber. A bias tee ZFBT-6GW from Minicircuits connects the V_{g} line with the coaxial

	Device 1	Device 2
Cavity	microstrip meander	microstrip meander
$\omega_c/2\pi$ (0 V)	6.73 GHz	6.62 GHz
$\kappa_{tot}/2\pi$ (0 V)	15.2 MHz	17 MHz
$\kappa_{ext}/2\pi$ (0 V)	2 MHz	2.1 MHz
$\kappa_{int}/2\pi$ (0 V)	13.2 MHz	14.9 MHz
Graphene device		
Exfoliated with	Scotch tape	Scotch tape
Drum radius	1.75 μm	1.75 μm
Cavity electrode radius	1.1 μm	1.25 μm
Graphene cavity-electrode separation	95 nm	135 nm
Graphene contacts	Nb	Nb
$\omega_m/2\pi$	58 MHz (0 V)	33.9 MHz (0 V)
Effective mass	$6.6 \times m_{eff,0}$	$18 \times m_{eff,0}$
Coupling		
$g_0/2\pi$	7 Hz (0 V)	3 Hz (0 V)

Table 6.1: **Device parameters.** The cavity is characterized by its resonance frequency ω_c and its total coupling rate κ_{tot}, which is composed of the external coupling rate κ_{ext} and the internal loss rate κ_{int}. The voltage in brackets is the DC electrode voltage V_g at which the parameter is measured. The dimensions of the mechanical resonators are measured with an atomic force microscope. The initial separation of the graphene drum and the gate electrode is estimated from the height difference between the graphene contact electrodes and the gate electrode. The resonance frequency of the lowest mechanical mode is $\omega_m/2\pi$. The effective mass m_{eff} of the few layer graphene drums is given in terms of the effective mass of a single layer graphene drum $m_{eff,0} \approx 2$ fg. The single photon coupling g_0 is calibrated from the driven motion as described in Sec. 6.7.

cable used to apply the low frequency drive. In contrast to the directional coupler employed for the thermalization of the pump line, we use a 20 dB cryogenic attenuator at 15 mK on the drive line.

The cavity pump tone at frequency ω_p is generated with an Agilent E8257D PSG microwave source. An Agilent N5181A microwave source is used to generate the MHz frequency drive at ω_d. The HEMT is a LNF-LNC4_8A from Low Noise Factory. We use an Agilent MXA N9020A with integrated preamplifier to measure the output spectrum. We characterize the properties of the superconducting cavity with a vector-network analyzer (VNA) ZVB14 from Rohde&Schwarz.

6.10.3 Calibration

To relate the externally applied RF power and the measured RF power to the actual fields at the sample, a careful calibration of the attenuation and gain in the setup is needed. The RF-input lines are attenuated at different temperature stages in the cryostat to shield the device from electromagnetic noise and to thermalize the lines. The total loss in the lines is the sum of the contributions from the attenuators and the loss in cables and connectors. In the input lines of the cold cryostat we measure a total attenuation of $loss(\omega_d) = 57$ dB in the 10-100 MHz range and $loss(\omega_c) = 64$ dB around $\omega_c/2\pi = 6.7$ GHz. The output of the cavity is shielded by two circulators that are operated as isolators at 15 mK, and then

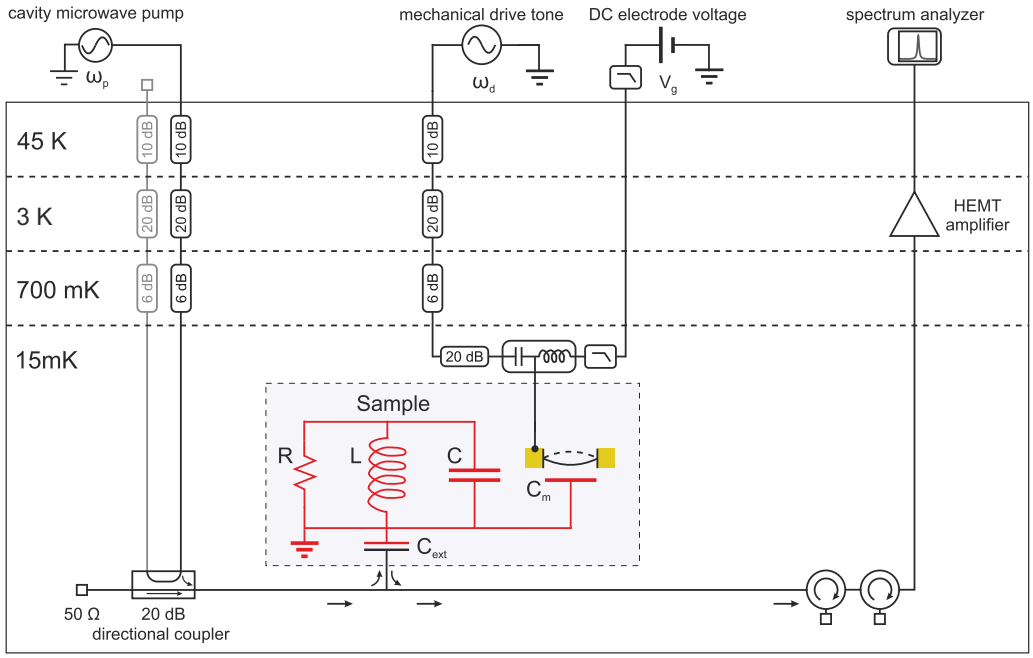

Figure 6.8: **Measurement setup with cryogenic wiring.**

amplified by a low-noise amplifier at 3 K with gain $G(\omega_c) = 43\,\mathrm{dB}$ and noise temperature $T_{\mathrm{noise}} \approx 2\,\mathrm{K}$ measured by the factory at 10 K.

We measure a detection limit of $S_{N,SA} = -157\,\mathrm{dBm/Hz}$ in our spectrum analyzer (SA). This noise floor is limited by the input noise of the amplifier. From $k_{\mathrm{B}}T_{\mathrm{noise}}(G - loss_{4\mathrm{K-SA}}) = -157\,\mathrm{dBm}$ we can extract $G - loss_{4\mathrm{K-SA}} = 38.5\,\mathrm{dB}$ and $loss_{4\mathrm{K-SA}} = 4.5\,\mathrm{dB}$. The total measured gain of the output line is $gain = G - loss_{4\mathrm{K-SA}} - loss_{\mathrm{sample-4K}} \approx 35\,\mathrm{dB}$ with $loss_{\mathrm{sample-4K}} \approx 3.5\,\mathrm{dB}$ which is reasonable considering the losses in the two circulators and the line at the level of the sample. Hence we are able to resolve noise powers of $S_{\mathrm{N}} > -157\,\mathrm{dBm/Hz} - 35\,\mathrm{dB} = -192\,\mathrm{dBm/Hz}$ in the transmission line of the sample. We measure a total transmitted power of $|S_{21}|^2 = -29.5\,\mathrm{dB}$ in device 1 and $|S_{21}|^2 = -28.5\,\mathrm{dB}$ in device 2, from the output of the RF source to the input of the spectrum analyzer around ω_{c}. This values agree well with our calibration, $|S_{21}|^2 = -loss + gain = -29\,\mathrm{dB}$.

Chapter 7

Force sensitivity of multilayer graphene optomechanical devices

This chapter is be published in parts in:

Force sensitivity of multilayer graphene optomechanical devices
P. Weber, J. Güttinger, A. Noury, J. Vergara-Cruz and A. Bachtold
Nature Communications 7, 12496 (2016)

In this chapter, we quantitatively investigate the force sensing performance of multilayer graphene mechanical resonators coupled to superconducting microwave cavities. We study how the measurement imprecision in the measurement of the vibrations affects the capability to sense small thermal forces. In particular, we illustrate the interplay between thermal force noise and imprecision force noise as a function of pump power when the superconducting cavity is pumped on the red sideband. In order to precisely study these effects we perform a thorough characterization of the optomechanical device properties, including the thermal calibration of the mechanical phonon occupation, the optomechanical single-photon coupling, and the tunability of the single-photon coupling by an applied static gate voltage. Additionally, we use the enhanced single-photon coupling at high gate voltage to perform sideband cooling experiments. We conclude the chapter with a discussion on thermal heating of the graphene resonators by cavity photons and the influence of mechanical resonance frequency fluctuations on the force sensing performance.

7.1 Introduction

Considerable effort has been devoted to developing mechanical resonators based on low-dimensional materials, such as carbon nanotubes [145, 10, 119, 146, 147, 148, 19, 20, 149, 30, 150, 151], semiconducting nanowires [121, 152, 153, 154, 155, 156, 157, 158, 159, 160], graphene [27, 24, 22, 161, 162, 163, 164], and monolayer semiconductors [117, 165, 109]. The specificity of these resonators is their small size and their ultra-low mass, which enables sensing of force and mass with unprecedented sensitivities [30, 19]. Such

high-precision sensing capabilities hold promise for studying physical phenomena in new regimes that have not been explored thus far, for instance, in spin physics [5], quantum electron transport [166, 167], light-matter interaction [157] and surface science [168, 169]. However, the transduction of the mechanical vibrations of nanoscale mechanical systems into a measurable electrical or optical output signal is challenging. As a result, force and mass sensing is often limited by the imprecision in the measurement of the vibrations, and cannot reach the fundamental limit imposed by thermo-mechanical noise.

A powerful method to obtain efficient electrical readout of small resonators is to amplify the interaction between mechanical vibrations and the readout field using a superconducting microwave cavity [163, 162]. Increasing the field in the cavity improves the readout sensitivity and eventually leads to dynamical back-action on the thermo-mechanical noise. This effect has been studied intensively on comparatively large micro-fabricated resonators, resulting for instance in enhanced optomechanical damping [31, 170], ground-state cooling of mechanical vibrations [108, 41], and displacement imprecision below the standard quantum limit [46, 47]. Another phenomenon often observed when detecting and manipulating the motion of mechanical resonators is the induced heating that can occur through Joule dissipation and optical absorption [163, 171]. Heating is especially prominent in tiny mechanical resonators because of their small heat capacity. An additional difficulty in characterizing mechanical vibrations is related to the fluctuations of the mechanical resonant frequency, also called frequency noise, which are particularly sizable in small resonators endowed with high quality factors Q [30].

In this chapter, we study the force sensitivity of multilayer graphene mechanical resonators coupled to superconducting cavities. In particular, we quantify how the force sensitivity is affected by dynamical back-action, Joule heating, and frequency noise upon increasing the number of pump photons inside the cavity. We demonstrate a force sensitivity of $(S_{\mathrm{F}}^{\mathrm{tot}})^{1/2} = 390 \pm 30\,\mathrm{zN\,Hz^{-1/2}}$, of which $\approx 50\%$ arises from thermo-mechanical noise and $\approx 50\%$ from measurement imprecision. The force sensitivity tends to be limited by measurement imprecision and frequency noise at low pump power, and by optomechanical damping and Joule heating at high pump power.

7.2 Thermal force noise and imprecision force noise

A fundamental limit of force sensing is set by the thermo-mechanical noise of the eigenmode that is measured. According to the fluctuation-dissipation theorem, the associated thermal force noise is white and is quantified by

$$S_{\mathrm{F}}^{\mathrm{mode}} = 4k_{\mathrm{B}}T_{\mathrm{mode}}m_{\mathrm{eff}}\Gamma_{\mathrm{eff}}^{\mathrm{spectral}} \tag{7.1}$$

where T_{mode} is the temperature of the mechanical eigenmode, and m_{eff} is its effective mass [4, 20]. This force noise is transduced into a mechanical resonance with line width $\Gamma_{\mathrm{eff}}^{\mathrm{spectral}}$ and height $S_{\mathrm{z}}^{\mathrm{mode}}$ in the displacement spectrum (Fig. 7.1). Importantly, Eq. 7.1 shows that the low mass of graphene decreases the size of the thermo-mechanical force noise. However, a drawback of tiny resonators with high Q-factors is their tendency to feature sizable frequency noise that broadens the resonance and, therefore, increases the size of the force noise [30, 172].

Measuring mechanical vibrations with high accuracy is key to resolving small forces, since the imprecision in the measurement contributes to the force sensitivity. The force

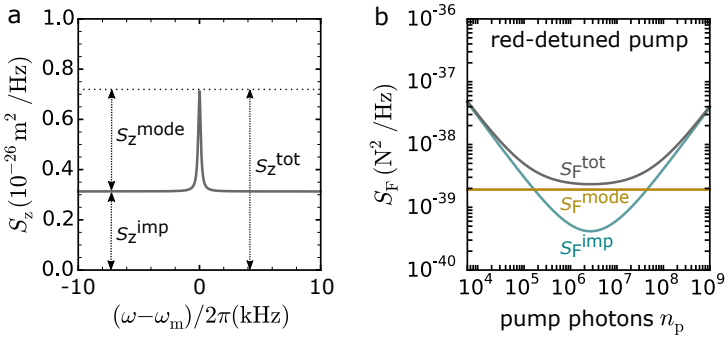

Figure 7.1: **Mechanical displacement and force sensitivity.** (**a**) Mechanical displacement spectrum S_z close to the mechanical resonance frequency $\omega_m/2\pi$. The total displacement spectral density S_z^{tot} at ω_m is the sum of the displacement noise $S_z^{mode}(\omega_m)$ and the displacement imprecision S_z^{imp}. (**b**) Corresponding force sensitivity $S_F^{tot} = S_F^{mode} + S_F^{imp}$ (dark grey). The individual components are the thermal force noise S_F^{mode} (dark yellow) and the imprecision force noise S_F^{imp} (turquois), given by Eqs. 7.1 and 7.2, respectively. The quantum back-action noise is neglected for simplicity. For the plots most of the parameters are those of device B, but we estimate the mass assuming that the graphene flake is a single layer. Further we choose $n_{add} = 0.5$, $T_{bath} = 0.015\,K$, and $n_p = 2 \cdot 10^5$ in **a** (see text).

sensitivity S_F^{tot} is given by the sum of the thermal force noise S_F^{mode} and the imprecision force noise S_F^{imp}, where the latter is the result of the white noise background with strength S_z^{imp} in the displacement spectrum (Fig. 7.1(a)). The challenge with mechanical resonators based on low-dimensional systems is to reach the limit $S_F^{imp} < S_F^{mode}$. When detecting the motion of graphene resonators with microwave cavities, one typically operates in the resolved sideband limit [163, 162], where the cavity decay rate κ is significantly smaller than the mechanical resonance frequency ω_m. This is interesting for force sensing, because pumping on the red sideband allows to enhance the mechanical damping rate, and therefore to reduce the harmful effect of frequency noise, as we will discuss below. In addition, this allows to increase the measurement bandwidth, as is often done in magnetic resonance force microscopy experiments [5] while keeping S_F^{mode} constant. The drawback of red sideband pumping compared to pumping at the cavity resonant frequency is an increased imprecision force noise at high pump powers. In the red-detuned pump regime, the measurement imprecision contributes to the force sensitivity by the amount

$$S_F^{imp} = \hbar\omega_m m_{eff} \frac{\kappa}{\kappa_{ext}} \frac{\left(\Gamma_m^{spectral} + 4n_p g_0^2/\kappa\right)^2}{4n_p g_0^2/\kappa} \left(n_{add} + \frac{1}{2}\right), \tag{7.2}$$

with $\Gamma_m^{spectral}$ the intrinsic line width of the resonator. Figure 7.1(b) shows the pump power dependence of the force sensitivity S_F^{tot} expected in the absence of Joule heating and frequency noise. The increase of S_F^{tot} at high n_p is due to the dynamical back-action, which enhances the mechanical line width by $\Gamma_{opt} = 4n_p g_0^2/\kappa$.

7.3 Device and setup

Our devices consist of a suspended graphene mechanical resonator capacitively coupled to a superconducting Nb cavity (see Fig. 7.2(a-c)). The graphene resonators are circular with a radius of $R \approx 1.6\,\mu$m. Here we present data of 2 devices. The fundamental mode of devices A and B vibrates at $\omega_m/2\pi = 67\,$MHz and $\omega_m/2\pi = 46\,$MHz at $V_g = 0\,$V, respectively. Here V_g is the constant voltage applied between the graphene flake and the superconducting cavity. The separation between the graphene resonator and the cavity counter electrode at $V_g = 0\,$V is assumed to be equal to the hole depth, which is typically $d_0 \approx 85\,$nm in our devices as measured with AFM. For the superconducting cavity we choose a single-port, quarter wavelength, coplanar waveguide reflection geometry. We characterize the cavity by plotting the coefficient $|S_{11}|^2$ and the phase of the reflected signal when sweeping the frequency over the cavity resonance at $\omega_c/2\pi = 7.416\,$GHz (see Figs. 7.2(d,e)). The external coupling rate κ_{ext} and the internal loss rate κ_{int} are extracted by fitting the measurement with the line shape expected for a one-port reflection cavity (see cf. Eq. 4.25)

$$S_{11} = \frac{\kappa_{int} - \kappa_{ext} - 2i(\omega - \omega_c)}{\kappa_{int} + \kappa_{ext} - 2i(\omega - \omega_c)}, \tag{7.3}$$

which yields $\kappa_{int}/2\pi = 950\,$kHz and $\kappa_{ext}/2\pi = 850\,$kHz at $V_g = 3.002\,$V for device A. The rates of Device B are $\kappa_{int}/2\pi = 800\,$kHz and $\kappa_{ext}/2\pi = 1700\,$kHz at $V_g = 0\,$V (see Sec. 8.6.3).

We detect the vibrations of the graphene resonator with high precision by pumping the cavity with an electromagnetic field, and probing its mechanical sideband. We usually set $\omega_p = \omega_c - \omega_m$ and probe the electromagnetic field that exits the cavity at ω_c. We measure the device at the cryostat base temperature of 15 mK if not stated otherwise. The cavity output field is amplified with a high electron-mobility-transistor (HEMT) mounted at the 3 K stage of the cryostat. Mechanical noise spectra are detected with a spectrum analyzer at room temperature. For a detailed description of the measurement setup see Sec. 7.10.2. In addition, we perform ring-down measurements to determine the mechanical dissipation rate Γ_{eff}^{decay} of the graphene resonator. Spectral measurements are not suitable for quantifying reliably Γ_{eff}^{decay} because of the potentially substantial frequency noise of graphene resonators. The implementation of ring-down measurements is described in Sec. 8.6.2.

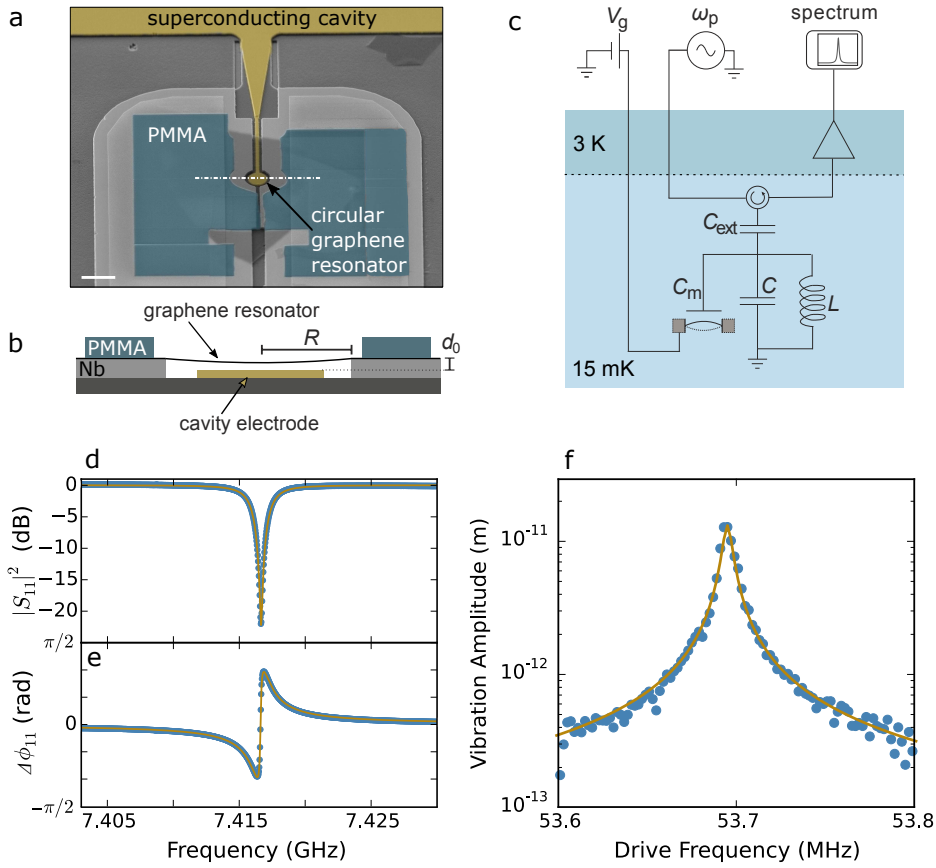

Figure 7.2: **Device and characterization.** (**a**) False-color SEM image of the device. The cavity is coloured in dark yellow. The graphene flake is clamped in between niobium support electrodes (grey) and cross-linked PMMA (turquois). The scale bar is 5 μm. (**b**) Schematic cross-section of the graphene resonator along the white dashed dotted line in **a**. (**c**) Schematic of the measurement circuit. The graphene mechanical resonator is coupled to the superconducting LC cavity through the capacitance C_m. The separation d between the suspended graphene flake and the cavity counter electrode is controlled by the constant voltage V_g. The cavity is pumped with a pump tone at ω_p and the output signal is amplified at 3 K. (**d**) Reflection coefficient $|S_{11}|^2$ and (**e**) reflected phase $\Delta\phi_{11}$ of the superconducting cavity of device A at $V_\mathrm{g} = 3.002\,\mathrm{V}$. The dark yellow lines are fits to the data using $\kappa_\mathrm{int}/2\pi = 950\,\mathrm{kHz}$ and $\kappa_\mathrm{ext}/2\pi = 850\,\mathrm{kHz}$ using Eq. 7.3. (**f**) Driven vibration amplitude of the graphene resonator of device A as a function of drive frequency. The driving voltage is 22 nV and $V_\mathrm{g} = 3.002\,\mathrm{V}$. The dark yellow line is a lorentzian fit to the data.

7.4 Gate dependence of mechanical frequency

Deflecting the graphene membrane by tuning $|V_g|$ results in the reduction of both ω_c and ω_m (Figs. 7.3(a,b)). The reduction of $\omega_m/2\pi$ is particularly large as it decreases from 67 MHz at $V_g = 0$ V to below 40 MHz at $V_g = 3.055$ V for device A. This decrease is attributed to the electrostatic softening of the graphene spring constant [22, 133]. From the comparison between the measurement and the expected electrostatic softening for weak resonator deflection [71]

$$\omega_m = \sqrt{\omega_{m,0} - \frac{1}{2m_{eff}}(\partial_z^2 C_m)V_g^2} \tag{7.4}$$

with $\partial_z^2 C_m$ obtained by differentiating Eq. 7.8 (see Sec. 7.6 for details), we get $m_{eff} = 3.3 \cdot 10^{-17}$ kg (solid line of Fig. 7.3(b)). This value differs from $m_{eff} = 4.9 \cdot 10^{-17}$ kg estimated from the dimensions of the resonator measured by AFM. Both methods may lead to an error in the estimation of m_{eff}, as AFM in air can overestimate the graphene thickness due to electrostatic forces induced by humidity adsorbed on the surface [173], while the mass estimated from electrostatic softening depends on the assumed mode shape, which is not well known. Therefore, we use $m_{eff} = (4.1 \pm 0.8) \cdot 10^{-17}$ kg for device A, which corresponds to approximately 25 layers. For device B we obtain consistently 5-6 layers ($m_{eff} = (9.6 \pm 0.8) \cdot 10^{-18}$ kg), both by measuring the dependence of ω_m on V_g and by optical contrast measurements [114, 115].

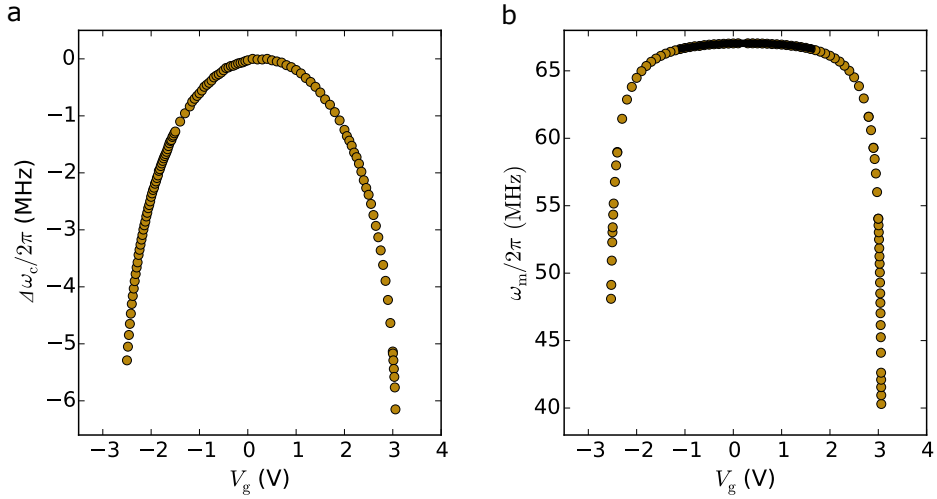

Figure 7.3: **Gate dependence of cavity frequency and mechanical frequency.** (**a**) Change $\Delta\omega_c$ of the resonant frequency of the superconducting cavity. The frequency at $V_g = 0\,\mathrm{V}$ is $\omega_{c,0}/2\pi = 7.42\,\mathrm{GHz}$. (**b**) Resonant frequency $\omega_m/2\pi$ of the graphene resonator as a function of V_g. The black line is the V_g dependence of ω_m expected from electrostatic softening.

7.5 Optomechanical device properties

In order to calibrate the phonon occupation n_m, the single-photon optomechanical coupling g_0, and the cavity pump photon number n_p, we perform the following three characterization measurements on both devices. (i) The measurement of the thermal resonance as a function of cryostat temperature T_{cryo}. This allows for the calibration of n_m by relating the integrated area of the thermal resonance to T_{cryo}. (ii) The measured transmitted power between the input port and the output port of the cryostat several MHz away from the cavity resonance frequency, which quantifies the product of $loss \cdot gain$. The product $loss \cdot gain$ together with the measurement in (i) yield g_0. (iii) Knowing g_0, the measured mechanical decay rate of the graphene resonator as a function of the pump power applied at the input port of the cryostat allows us to precisely calibrate n_p.

7.5.1 Mechanical mode occupation

In order to calibrate the mechanical phonon occupation n_m and the mode temperature T_{mode}, we measure the mechanical thermal motion spectrum while varying the cryostat temperature [108]. This is done by pumping the cavity with a weak pump tone on the red sideband (so that the optomechanical scattering rate Γ_{opt} is much smaller than the intrinsic dissipation rate Γ_m^{decay} of the graphene resonator), and measuring the area of the thermal mechanical resonance at ω_c. In thermal equilibrium, the area is linearly proportional to the motional variance $\langle z^2 \rangle$ and thus directly linked to the temperature of the mode T_{mode} through the equipartition theorem $1/2 m_{eff} \omega_m^2 \langle z^2 \rangle = 1/2 k_B T_{mode}$. In Fig. 7.4(b) we show such a calibration measurement at $V_g = 3.002\,\mathrm{V}$ for device A. T_{mode} is linearly proportional to T_{cryo} for temperatures above 100 mK so that we assign $T_{mode} = T_{cryo}$ and extract the resonator phonon occupation $n_m = \frac{k_B T_{mode}}{\hbar \omega_m}$. Below 100 mK

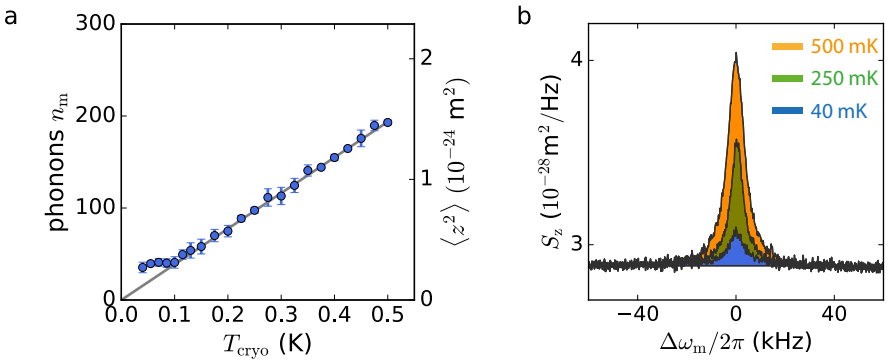

Figure 7.4: **Thermal calibration of fundamental mechanical mode with red-detuned pumping.** (**a**) Selected thermo-mechanical noise spectra for different temperatures and $n_p = 6 \cdot 10^4$. (**b**) Plot of the measured mechanical mode temperature of device A, expressed in phonon occupation n_m, as a function of cryostat temperature at $V_g = 3.002\,\mathrm{V}$ where $\omega_m/2\pi = 53.7\,\mathrm{MHz}$ and $n_p = 6 \cdot 10^4$. On the right y-axis, we display the variance of the vibration amplitude $\langle z^2 \rangle$, which is obtained by integrating the thermal resonance, as is shown in **a**. The phonon occupation is quantified with $\langle z^2 \rangle = \frac{\hbar}{m_{eff}\omega_m} n_m$. The error bars are given by the standard deviation of 5 spectral measurements.

the mechanical mode does not thermalize well with the cryostat. The origin of this poor thermalization at low temperature may be related to the heating induced by the pump field (see Sec. 7.8) [163], and a non-thermal force noise [36] such as the electrostatic force noise related to the voltage noise in the device.

7.5.2 Single-photon optomechanical coupling

The measurement described in the previous subsection also allows to accurately calibrate g_0. It is inferred from the area of the thermal resonance measured as the output power $P_{out} = \int S_{out} d\omega/2\pi$ at the level of the spectrum analyzer and the input power P_{in} applied at the input port of the cryostat. The ratio P_{out}/P_{in} for a $\lambda/4$ cavity measured in reflection, in the resolved sideband regime and for red-detuned pumping, reads (see cf. Eq. 4.41)

$$\frac{P_{out}}{P_{in}} = 4g_0^2 \cdot gain \cdot loss \cdot \frac{\kappa_{ext}^2}{\kappa^2} \frac{1}{\omega_m^2} \frac{k_B}{\hbar\omega_m} T_{cryo}. \tag{7.5}$$

We determine the product $loss \cdot gain = -32.1\,\mathrm{dB}$ by measuring the transmitted power between the input port and the output port of the cryostat at a frequency $\omega_p = \omega_c - \omega_m$. From the data shown in Fig. 7.4(a) we extract $g_0/2\pi = 42.6\,\mathrm{Hz}$, which is the largest value achieved so far with graphene optomechanical systems [162, 163]. For this calibration to be precise, we verify that the response of the transmitted power through our input and output lines remains constant over the frequency range between ω_c and ω_p. For device B we perform the calibration in the same manner and obtain $g_0/2\pi = 7.3\,\mathrm{Hz}$ at $V_g = 0\,\mathrm{V}$.

We check with device B that the aforementioned calibration procedure yields the same g_0 as that obtained with the procedure based on the frequency modulation (FM) of the pump field [162, 39]. In the latter, g_0 is inferred by pumping the cavity with a FM sig-

nal with known modulation index ϕ_0 and modulation frequency $\omega_{\mathrm{mod}}/2\pi$, see Fig. 7.5. The modulation frequency is chosen close to the mechanical frequency, but outside the mechanical line width. When applying the FM signal additionally to the red sideband pump, the single-photon optomechanical coupling can be extracted by measuring the ratio of the area under the mechanical sideband to the area under the modulation peak using

$$g_0^2 = \left(\frac{\phi_0}{2}\right)^2 \frac{\omega_{\mathrm{m}}^2}{n_{\mathrm{m}}} \frac{S_{\mathrm{out}}(\omega_{\mathrm{m}}) \cdot \Gamma_{\mathrm{m}}^{\mathrm{spectral}}/4}{S_{\mathrm{out}}(\omega_{\mathrm{mod}}) \cdot RBW}. \tag{7.6}$$

Here, RBW is the measurement resolution band width. Both $\Gamma_{\mathrm{m}}^{\mathrm{spectral}}$ and RBW are taken in units of frequency. Performing this analysis in thermal equilibrium at $T = 220\,\mathrm{mK}$ we obtain $g_0/2\pi = 8.4\,\mathrm{Hz}$, which is in agreement with the value $g_0/2\pi = 7.3\,\mathrm{Hz}$ obtained from the first calibration method discussed in this section.

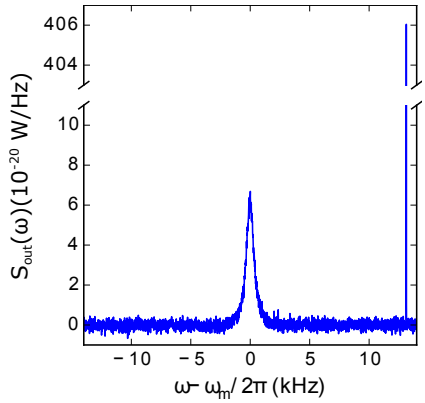

Figure 7.5: Output spectrum of mechanical sideband and FM signal at $T = 220\,\mathrm{mK}$ for device B. The mechanical resonance frequency is $\omega_{\mathrm{m}}/2\pi = 46.06\,\mathrm{MHz}$ and the modulation frequency $\omega_{\mathrm{mod}}/2\pi = \omega_{\mathrm{m}}/2\pi + 13.1\,\mathrm{kHz}$. The data is taken in a regime where backaction is negligible. The modulation depth ϕ_0 is measured by extracting the ratio between pump signal and the first sideband signal $S_{\mathrm{out}}(\omega_{\mathrm{p}} + \omega_{\mathrm{out}})/S_{\mathrm{out}}(\omega_{\mathrm{p}}) = \phi_0/2$ for $\phi_0 << 1$. We use $\phi_0 = 10^{-116.7\,dB/20} \cdot 2 = 2.9244 \cdot 10^{-6}$ for this measurement. Note that we have subtracted the measurement imprecision in the figure.

7.6 Tunability of single-photon coupling and static deflection

For device A, we show that the single-photon optomechanical coupling at $V_{\mathrm{g}} = 3.002\,\mathrm{V}$ is significantly enhanced by the deflection of the membrane towards the cavity electrode. For this, we first relate P_{in} to n_{p} by calibrating the loss coefficient *loss* over the mechanical decay rate. Having calibrated *loss*, we then extract g_0 for different gate voltages to confirm the tunability of g_0. In Fig. 7.6(b) we measure the mechanical decay rate $\Gamma_{\mathrm{eff}}^{\mathrm{decay}}$ at $V_{\mathrm{g}} = 3.002\,\mathrm{V}$ with the ring-down technique as a function of P_{in}. The measurement is well described by $\Gamma_{\mathrm{eff}}^{\mathrm{decay}} = \Gamma_{\mathrm{m}}^{\mathrm{decay}} + \Gamma_{\mathrm{opt}}$ where $\Gamma_{\mathrm{m}}^{\mathrm{decay}}$ is the intrinsic mechanical dissipation

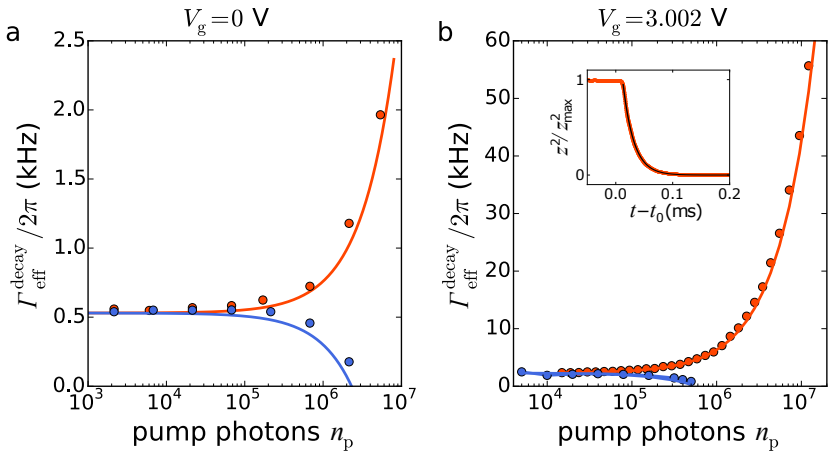

Figure 7.6: **Effective mechanical energy decay rates extracted from ring-down measurements.** Mechanical dissipation rate $\Gamma_{\rm eff}^{\rm decay}$ measured on device A with the ring-down technique as a function of the number $n_{\rm p}$ of pump photons in the cavity at $V_{\rm g} = 0\,{\rm V}$ and $V_{\rm g} = 3.002\,{\rm V}$ where $n_{\rm p}$ is proportional to the microwave power $P_{\rm in}$ applied at the input of the cryostat. Red and blue data points correspond to red and blue detuned pumping, respectively. The measurements are well described by $\Gamma_{\rm eff}^{\rm decay} = \Gamma_{\rm m}^{\rm decay} \pm \Gamma_{\rm opt}$ (red and blue lines) using $g_0/2\pi = 9.7\,{\rm Hz}$ in **a** and $g_0/2\pi = 42.6\,{\rm Hz}$ in **b**. The inset in **b** shows a ring-down measurement for $n_{\rm p} = 1.4 \cdot 10^6$. We plot the normalized vibration amplitude as a function of time t. The resonator is driven with a capacitive driving force for $t < t_0$. At t_0 the drive is switched off and the vibration amplitude decays freely ($t > t_0$). We fit the data with an exponential decay (black line) using $z^2(t) = z_0^2 \exp(-\frac{t-t_0}{\tau})$ with a decay rate $\Gamma_{\rm eff}^{\rm decay} = 1/\tau = 2\pi \cdot 8.4\,{\rm kHz}$.

rate, $\Gamma_{\rm opt} = \pm 4 n_{\rm p} g_0^2/\kappa$, $\pm$ corresponds to red and blue detuned pumping at $\omega_{\rm p} = \omega_{\rm c} \mp \omega_{\rm m}$, respectively, and

$$n_{\rm p} = \frac{1}{\hbar\omega_{\rm p}} \cdot P_{\rm in} \cdot loss(\omega_{\rm p}) \cdot \frac{4\kappa_{\rm ext}}{\kappa^2 + 4(\omega_{\rm p} - \omega_{\rm c})^2}. \tag{7.7}$$

From the fit to the data with the previously obtained value of $g_0/2\pi = 42.6\,{\rm Hz}$ we estimate $loss = -63.7\,{\rm dB}$, which additionally yields $gain = 31.6\,{\rm dB}$ from the product $loss \cdot gain$. In order to get g_0 at $V_{\rm g} = 0\,{\rm V}$, we use the gate voltage independent calibration of $n_{\rm p}$ to fit the measured $n_{\rm p}$ dependence of $\Gamma_{\rm eff}^{\rm decay}$ in Fig. 7.6(a). We obtain $g_0 = 2\pi \times 9.7\,{\rm Hz}$. This confirms that increasing $V_{\rm g}$ from 0 to $3.002\,{\rm V}$ results in a strong increase of the optomechanical coupling by more than a factor four due to the static deflection of the graphene membrane.

We infer the deflection of the graphene flake of device A from the variation of the single-photon coupling when varying the voltage $V_{\rm g}$. We assume that the shape of the static graphene deformation depends on the radial coordinate r as $\xi_{\rm s}(r) = z_{\rm s}(1 - r^2/R^2)$. With this deflection profile we evaluate the derivative of the capacitance with respect to displacement using a local plate capacitor approximation

$$\partial_{\rm z} C_{\rm m} = \epsilon_0 \int_0^{2\pi} d\phi \int_0^{R_{\rm g}} r dr \frac{\partial}{\partial z_{\rm s}} \frac{1}{d_0 - z_{\rm s}(1 - \frac{r^2}{R^2})}. \tag{7.8}$$

Here $R_{\rm g}$ is the radius of the cavity counter electrode. Using the measured g_0 and $\omega_{\rm m}$

values (Figs. 7.3(b) and 7.6(a,b)) in $g_0 \propto \partial_z C_m \sqrt{1/\omega_m}$, we estimate that the separation between the membrane and the cavity counter electrode is reduced from 88 nm to 33 nm when varying V_g from 0 to 3.002 V.

An alternative method to determine the separation as a function of V_g relies on the change of the total capacitance $C_{tot} = C + C_{ext} + C_m$ measured from the dependence of the cavity resonance frequency $\omega_c = 1/\sqrt{LC_{tot}}$ on V_g (see Fig. 7.3(a)). We assume $\Delta C_m = \Delta C_{tot}$ upon varying V_g and compare the measured ΔC_{tot} to $\partial_z C_m$ from which we obtain a reduction of d from 88 nm to 53 nm for $V_g = 3.002$ V.

7.7 Sideband cooling and displacement imprecision

We can take advantage of the enhanced g_0 in order to cool the mode temperature. When increasing the power of the pump tone on the red sideband and keeping the temperature of the cryostat constant at $T = 15$ mK the measured resonance gets broader and its area smaller (Fig. 7.7(a)), showing that the mechanical mode is damped and cooled [31, 170]. At the largest available pump power, the phonon occupation reaches $n_m = 7.2 \pm 0.2$ (Fig. 7.7(c)). This is the lowest phonon occupation obtained in a mechanical resonator based on graphene [163, 28, 162]. The error in the estimation of n_m is given by the standard error obtained from 5 successive spectral measurements.

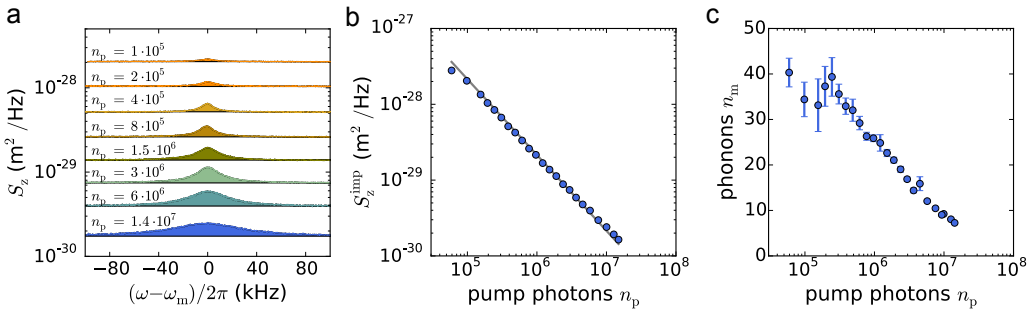

Figure 7.7: **Sideband cooling and displacement imprecision of device A.** (**a**) Mechanical displacement spectral density S_z measured with red-detuned pumping. The cryostat temperature is 15 mK. (**b**) Displacement imprecision as a function of cavity pump photon population. The line is a fit of Eq. 7.9 with $n_{add} = 32$. (**c**) Average phonon number n_m as a function of n_p.

The improved coupling allows us to achieve also an excellent displacement sensitivity S_z^{imp} (Fig. 7.7(b)). At the largest pump power, we obtain $(S_z^{imp})^{1/2} = 1.3 \pm 0.2$ fm Hz$^{-1/2}$, which compares favorably to previous works [28, 162, 174]. The error in S_z^{imp} is given by the uncertainty in the estimation of m_{eff}. We obtain S_z^{imp} from the noise floor of the measured power spectral density S_N using $S_z^{imp} = \frac{S_N}{\hbar\omega_c}\frac{\kappa^2}{2\kappa_{ext}}\frac{z_{zp}^2}{g_0^2}\frac{1}{n_p}$. The displacement sensitivity scales as $1/n_p$ (Fig. 7.7(b)). By comparing the measurement to the expected displacement sensitivity [38]

$$S_z^{imp} = \left(n_{add} + \frac{1}{2}\right)\frac{\kappa^2}{2\kappa_{ext}}\frac{z_{zp}^2}{g_0^2}\frac{1}{n_p}, \tag{7.9}$$

we obtain that the equivalent noise added by the amplifier chain is $n_{\mathrm{add}} = 32$. This is a reasonable value for a HEMT amplifier mounted at 3 K [107, 46].

7.8 Force sensitivity

We now quantify the force sensitivity as a function of the microwave pump power (Figs. 7.8(a,c)). Since the mechanical resonances in the measured displacement spectra are well described by Lorentzian line shapes, the thermal force noise is quantified using $S_{\mathrm{F}}^{\mathrm{mode}} = S_{\mathrm{z}}^{\mathrm{mode}}(\omega_{\mathrm{m}})/|\chi_{\mathrm{eff}}(\omega_{\mathrm{m}})|^2$ with the effective mechanical susceptibility $|\chi_{\mathrm{eff}}(\omega_{\mathrm{m}})|^2 = 1/(m_{\mathrm{eff}}\omega_{\mathrm{m}}\Gamma_{\mathrm{eff}}^{\mathrm{spectral}})^2$. Similarly, we obtain the imprecision force noise with $S_{\mathrm{F}}^{\mathrm{imp}} = S_{\mathrm{z}}^{\mathrm{imp}}/|\chi_{\mathrm{eff}}(\omega_{\mathrm{m}})|^2$. The best force sensitivity we achieve for device A is $(S_{\mathrm{F}}^{\mathrm{tot}})^{1/2} = 5.8\,\mathrm{aN\,Hz^{-1/2}}$ with a mechanical bandwidth of 20 kHz (Figs. 7.8(a) and 7.9(b)). In device B we reach a force sensitivity of $(S_{\mathrm{F}}^{\mathrm{tot}})^{1/2} = 390 \pm 30\,\mathrm{zN\,Hz^{-1/2}}$ with a mechanical bandwidth of 0.2 kHz (see Figs. 7.8(c) and 7.9(d)). The error in the estimation of the force sensitivity is obtained from both the uncertainty in the mass and the fluctuations in the measurement of $S_{\mathrm{F}}^{\mathrm{tot}}$, which we evaluate by calculating the standard error of 10 measurements. This force sensitivity compares favorably with the best sensitivities obtained with micro-fabricated resonators ($(S_{\mathrm{F}}^{\mathrm{tot}})^{1/2} = 510\,\mathrm{zN\,Hz^{-1/2}}$) [4, 46], albeit it is not as good as that of resonators based on carbon nanotubes [20, 30]. Compared to previous devices, the mechanical bandwidth of graphene resonators is much higher, which enables faster detection of sudden force changes.

We plot both $S_{\mathrm{F}}^{\mathrm{mode}}$ and $S_{\mathrm{F}}^{\mathrm{imp}}$ as a function of cavity pump photon population in Fig. 7.8(b). As expected, the imprecision force noise decreases at low n_{p} and increases at high n_{p} due to the enhanced damping caused by the optomechanical back-action. The thermal force noise $S_{\mathrm{F}}^{\mathrm{mode}}$ appears roughly constant when varying n_{p} as a result of the competing effects of Joule heating and frequency noise. Joule heating is caused by the microwave current in the graphene flake induced by the pump field. This results in the increase of the temperature T_{bath} of the thermal bath coupled to the mechanical mode as well as the mechanical dissipation rate [163, 161]. We can infer the product $T_{\mathrm{bath}} \cdot \Gamma_{\mathrm{m}}^{\mathrm{decay}}$ from the measurements of n_{m} and $\Gamma_{\mathrm{eff}}^{\mathrm{decay}}$ in Figs. 7.6(b), 7.7(c) using

$$T_{\mathrm{bath}}\Gamma_{\mathrm{m}}^{\mathrm{decay}} = T_{\mathrm{mode}}\Gamma_{\mathrm{eff}}^{\mathrm{decay}} = n_{\mathrm{m}}\Gamma_{\mathrm{eff}}^{\mathrm{decay}} \cdot \frac{\hbar\omega_{\mathrm{m}}}{k_{\mathrm{B}}}. \tag{7.10}$$

When increasing the pump power, Joule heating significantly increases the product $T_{\mathrm{bath}}\Gamma_{\mathrm{m}}^{\mathrm{decay}}$ (Fig. 7.9(a)), and therefore the size of the thermal force noise (Eq. 7.1). We see next that the effect of frequency noise leads to the opposite dependence of the thermal force noise on pump power. Frequency noise enhances the spectral line width by the amount $\delta\Gamma_{\mathrm{noise}}$,

$$\Gamma_{\mathrm{eff}}^{\mathrm{spectral}} = \Gamma_{\mathrm{eff}}^{\mathrm{decay}} + \delta\Gamma_{\mathrm{noise}}, \tag{7.11}$$

when the fluctuations of the resonant frequency are described by a white noise [20]. The measurements of $\Gamma_{\mathrm{eff}}^{\mathrm{spectral}}$ and $\Gamma_{\mathrm{eff}}^{\mathrm{decay}}$ as a function of pump power can be well described by Eq. 7.11 with $\delta\Gamma_{\mathrm{noise}}/2\pi = 8.7\,\mathrm{kHz}$ (Fig. 7.9(b)). Importantly, Fig. 7.9(b) shows that $\Gamma_{\mathrm{eff}}^{\mathrm{spectral}}$ is comparable to $\Gamma_{\mathrm{eff}}^{\mathrm{decay}}$ at large pump power, showing that the relative contribution of $\delta\Gamma_{\mathrm{noise}}$ to $\Gamma_{\mathrm{eff}}^{\mathrm{spectral}}$ gets negligible upon increasing n_{p}. As the cooling

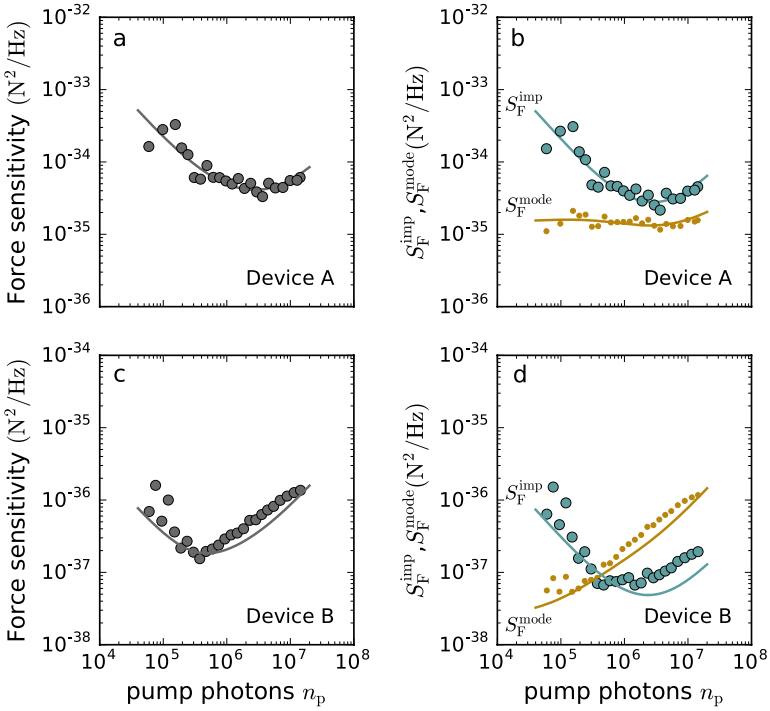

Figure 7.8: **Characterization of the imprecision force noise, the thermal force noise and the total force sensitivity.** (**a**) Force sensitivity $S_F^{tot} = S_F^{imp} + S_F^{mode}$ as a function of cavity pump photon population measured when pumping the cavity on the red sideband. (**b**) Imprecision force noise S_F^{imp} (turquois) and thermal force noise S_F^{mode} (dark yellow) versus n_p. The data in **a,b** are fitted to Eqs. 7.2, 7.12. (**c,d**) Equivalent to (**a,b**) but for device B. The lowest value for the force sensitivity in **c** is $(S_F^{tot})^{1/2} = 390 \pm 30\,\mathrm{zN\,Hz^{-1/2}}$. In **c** and **d** the data are fitted with $n_{add} = 22$. All the measurements on device A are performed at $V_g = 3.002\,\mathrm{V}$ and on device B at $V_g = 0\,\mathrm{V}$. The cryostat temperature is 15 mK.

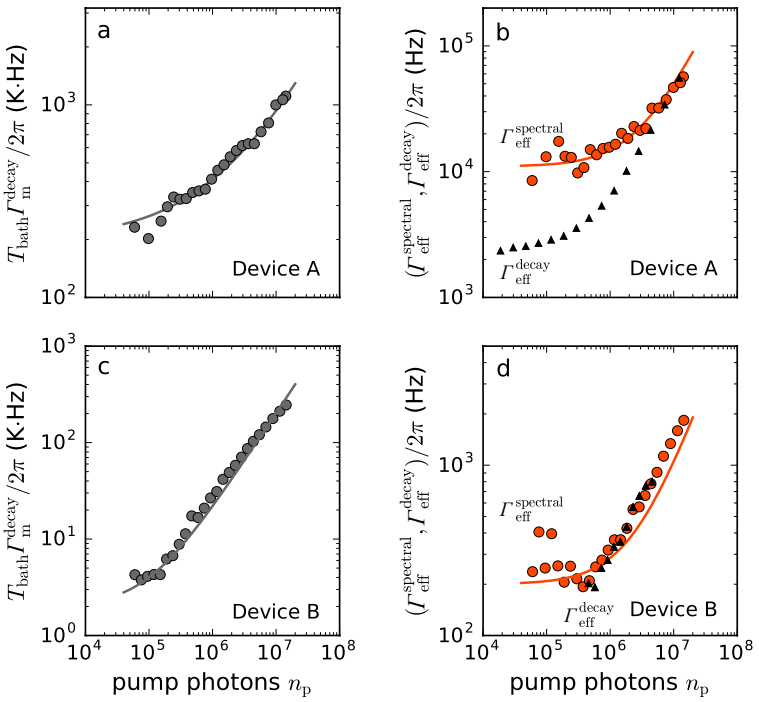

Figure 7.9: **Characterization of thermal heating and frequency fluctuations.** (**a**) Product of the bath temperature T_{bath} and the intrinsic mechanical decay rate $\Gamma_{\mathrm{m}}^{\mathrm{decay}}$ as a function of cavity pump photon occupation. The line is a fit to the data. (**b**) Effective spectral mechanical line width $\Gamma_{\mathrm{eff}}^{\mathrm{spectral}}$ as a function of n_{p}. The data are fitted to $\Gamma_{\mathrm{eff}}^{\mathrm{spectral}} = \Gamma_{\mathrm{eff}}^{\mathrm{decay}} + \delta\Gamma_{\mathrm{noise}}$ with $\delta\Gamma_{\mathrm{noise}}/2\pi = 8.7\,\mathrm{kHz}$. (**c,d**) Equivalent to (**a,b**) but for device B. In **d** we use $g_0/2\pi = 7.3\,\mathrm{Hz}$, $\kappa/2\pi = 2.5\,\mathrm{MHz}$ and $\delta\Gamma_{\mathrm{noise}}/2\pi = 0.145\,\mathrm{kHz}$. All the measurements on device A are performed at $V_{\mathrm{g}} = 3.002\,\mathrm{V}$ and on device B at $V_{\mathrm{g}} = 0\,\mathrm{V}$.

efficiency described by Eq. 7.10 remains unaltered by frequency noise (see chapter 7 in [175]), the thermal force noise is quantified by

$$S_{\mathrm{F}}^{\mathrm{mode}} = 4k_{\mathrm{B}}m_{\mathrm{eff}}T_{\mathrm{bath}}\Gamma_{\mathrm{m}}^{\mathrm{decay}}\frac{\Gamma_{\mathrm{eff}}^{\mathrm{spectral}}}{\Gamma_{\mathrm{eff}}^{\mathrm{decay}}}. \tag{7.12}$$

Taking into account the measured effects of Joule heating and frequency noise in Eq. 7.12, the thermal force noise $S_{\mathrm{F}}^{\mathrm{mode}}$ is expected to remain roughly constant as a function of n_{p} (dark yellow line in Fig. 7.8(b)), in agreement with the measurements. Overall, the best force sensitivity we achieve in this device is $(S_{\mathrm{F}}^{\mathrm{tot}})^{1/2} = 5.8\,\mathrm{aN\,Hz^{-1/2}}$ at $n_{\mathrm{p}} \approx 4 \cdot 10^6$ (Fig. 7.8(a)). While the force sensitivity in this device is primarily limited by the measurement imprecision, the thermal force noise is affected to a large extent by frequency noise at low n_{p} and by Joule heating at high n_{p}.

In device B, the graphene resonator has a lower mass and a narrower mechanical line width, two assets for high force sensitivity (Figs. 7.8(c,d) and 7.9(c,d)). The spectral line width corresponds to a mechanical quality factor of $Q \approx 200,000$. In this device we reach a force sensitivity of $(S_{\mathrm{F}}^{\mathrm{tot}})^{1/2} = 390 \pm 30\,\mathrm{zN\,Hz^{-1/2}}$ at $n_{\mathrm{p}} \approx 4 \cdot 10^5$ (see Figs. 7.8(c)). In an attempt to improve the thermal anchoring of device B compared to device A, the graphene contact electrodes contain an additional Au layer between the graphene and the Nb layer [176, 163]. The normal metal layer is expected to increase the thermal conductance between the graphene flake and the contact electrodes through electron diffusion, which allows for better heat dissipation into the contacts. However, device B is still strongly affected by Joule heating, which substantially increases the value of $S_{\mathrm{F}}^{\mathrm{mode}}$ when increasing the pump power (Figs. 7.8(d) and 7.9(c)). The heating is so strong that we are not able to reduce the phonon occupation n_{m} with sideband cooling. We attribute the strong heating to the fact that the resonator is significantly thinner than the one of device A and therefore has a smaller heat capacity. The effect of frequency noise on the spectral line width is negligible for pump powers above $n_{\mathrm{p}} \approx 4 \cdot 10^5$. We do not know the origin of the frequency noise but it might be related to charged two-level fluctuators in the device. The force sensitivity is here primarily limited by the measurement imprecision at low n_{p}, and by the thermo-mechanical force noise and Joule heating at high n_{p}.

7.9 Conclusions and Outlook

In the future, the force sensitivity of graphene optomechanical devices can be further improved using a quantum-limited Josephson parametric amplifier [107]. This readout will improve the measurement imprecision, by lowering n_{add} in $S_{\mathrm{F}}^{\mathrm{imp}}$. In addition, it will be possible to resolve the thermal vibrations with lower pump power, which is crucial to reduce Joule heating while working with low-mass graphene resonators. A quantum-limited amplifier with $n_{\mathrm{add}} = 0.5$ may allow to achieve $47\,\mathrm{zN\,Hz^{-1/2}}$ force sensitivity at 15 mK taking the mass of a single-layer graphene resonator with the diameter and the quality factor of device B (Fig. 7.1(b)). With only modest device improvements, it may be possible to probe the fundamental limit of continuous displacement detection imposed by quantum mechanics, since the force noise associated to quantum back-action $(S_{\mathrm{F}}^{\mathrm{qba}})^{1/2} = (2\hbar\omega_{\mathrm{m}}m_{\mathrm{eff}}\Gamma_{\mathrm{eff}}^{\mathrm{decay}})^{1/2} = 1.1\,\mathrm{aN\,Hz^{-1/2}}$ is approaching $(S_{\mathrm{F}}^{\mathrm{mode}})^{1/2} = 4.3\,\mathrm{aN\,Hz^{-1/2}}$ measured at $n_{\mathrm{p}} = 1.4{\cdot}10^7$ for device A. Force sensing with resonators based on two-dimensional materials hold promise for detecting electron and nuclear spins [5] using superconducting

cavities compatible with relatively large magnetic fields [177], and studying the thermodynamic properties of two-dimensional materials, such as the quantum capacitance and the magnetization [167].

7.10 Additional information

7.10.1 Device Parameters

Important parameters of the measured devices are summarized in Table 8.1.

7.10.2 Measurement setup

Figure 7.10 shows a detailed schematic of the measurement setup for device A (for device B see Sec. 8.6.2). The experimental setup used in this chapter is slightly modified compared to the configuration in the previous chapter (Sec. 6.10.2).

Due to the fact that the cavity is measured in reflection we connect the sample to the radio frequency lines of the cryostat by using a circulator. Further, the source used to apply the constant voltage V_g is a SIM928 from Stanford Research Systems. This source features better voltage noise characteristics than the Keithley 2400.

We cancel the pump signal at the output of the device in order to avoid saturation of the cryogenic HEMT amplifier, mounted at 3 K, when pumping the cavity with a strong pump tone. For this, we divide the signal of the pump source with a power splitter into a cavity pump signal and a cancellation signal. The cancellation signal interferes destructively with the pump signal after the pump signal is reflected from the cavity. On the cancellation line we use a Krytar 120420 20 dB directional coupler and an additional circulator. We adjust the cancellation signal with a digitally variable attenuator TEA13000-12 and a variable phase shifter TEP8000-6 from Telemakus to cancel the pump tone by ≈ 40 dB.

We amplify and filter the pump and the cancellation signals at room temperature. Careful filtering of the input signal is necessary to avoid populating the cavity with source phase noise or with noise of the amplifier. We use tunable bandpass filters. The bandpass filter BPF1 (Wainwright WBCQV6) at the output of the pump source has a pass band attenuation of -6 dB and reduces the phase noise of the pump signal by -50 dB at ± 50 MHz from its pass band frequency. The amplification is done with Mini-circuits ZVE-3W-83+ amplifiers. We reduce the amplifier white noise by a second set of bandpass filters BPF2 and BPF3 (both wainwright WTBCQV3). They attenuate the signal by -2 dB on the pass band frequency range and by -20 dB at ± 50 MHz away from it. Without this filtering scheme we populate the superconducting cavity at the highest pump powers.

The cancellation and the amplification of the pump signal requires recalibration of the cryostat input power. This is done by measuring P_{in} as a function of the power P_{RF} applied with the radio-frequency source for all available pump powers.

We can measure the output either in the frequency or the time domain. The scheme to measure the energy decay of the graphene resonator is described in detail in Sec. 8.6.2.

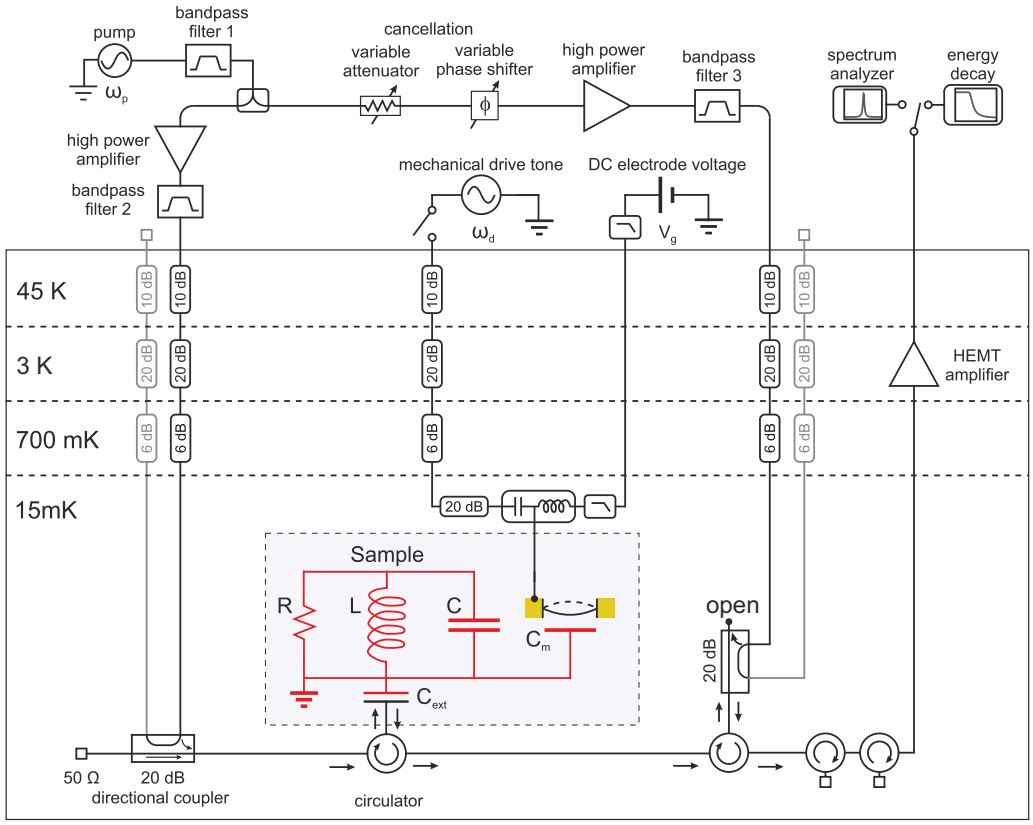

Figure 7.10: **Measurement setup with cryogenic wiring for device A.**

	Device A	Device B
Cavity	CPW	CPW
$\omega_c/2\pi$ (0 V)	7.42 GHz	7.49 GHz
$\kappa_{tot}/2\pi$ (0 V)	1.6 MHz	2.5 MHz
$\kappa_{ext}/2\pi$ (0 V)	850 kHz	1.7 MHz
$\kappa_{int}/2\pi$ (0 V)	750 kHz	850 kHz
Graphene device		
Exfoliated with	Scotch tape	PDMS
Drum radius	1.6 μm	1.65 μm
Cavity electrode radius	1.2 μm	1.1 μm
Graphene cavity-electrode separation	88 nm	85 nm
Graphene contacts	Nb	Nb and Au
$\omega_m/2\pi$	67 MHz (0 V)	46 MHz (0 V)
Effective mass	$25 \times m_{eff,0}$	$5.5 \times m_{eff,0}$
Coupling		
$g_0/2\pi$	9.7 Hz (0 V)	7.3 (0 V)

Table 7.1: **Device parameters.** The effective mass is obtained with different techniques including optical contrast measurements, thickness measurements by AFM and from the electrostatic softening of the graphene resonators (Sec. 7.4) where $m_{eff,0} \approx 1.6\,\text{fg}$. The single-photon coupling is calibrated from thermal motion measurements (Sec. 7.5.2).

Chapter 8

Energy decay measurements in multilayer graphene mechanical resonators

In this chapter, we present mechanical energy decay measurements of multilayer graphene mechanical resonators coupled to superconducting cavities. By comparing the energy decay with spectral measurements, both in the linear and nonlinear vibration regimes, we illustrate the importance of energy decay measurements for gaining insight into mechanical dissipation processes. After a short description of the requirements for the implementation of the detection scheme, we study the linear energy decay as a function of several parameters including the cryostat temperature, the pump photon number, and the gate voltage. Additionally to the decay of the vibrational amplitude, we study the frequency evolution during the decay when driving the mechanical vibrations to larger amplitudes. In the nonlinear vibration regime we discover peculiar features. These can partly be explained by nonlinear dissipation processes.

8.1 Introduction

Energy decay plays a central role in a wide range of phenomena, such as optical emission, nuclear fission, and dissipation in cavities and quantum bits. In mechanical resonators, the energy decay rate is important since it is a key figure of merit for many applications, such as mass, force, and spin sensing [152, 6, 19, 5, 30]. Understanding the physics of the energy decay remains however a challenge. There are many different processes that lead to energy decay in mechanical resonators [178]. They can result from the coupling of the vibrational eigenmodes of the resonator to phonons, electrons, and photons [8, 45]. Such decay processes are usually linear (Fig. 8.1(a)). The role of nonlinear processes is thought to become relevant in small resonators [179]. However, measuring energy decay in nanomechanical resonators remains difficult because of the lack of appropriate experimental tools. Most previous works relied on power spectrum measurements, but this method can suffer from dephasing, which broadens the mechanical resonance line width used to determine the energy decay rate [30, 180, 181, 182, 161, 183].

In this chapter, we report energy decay measurements in graphene resonators by directly recording the vibration amplitude as energy freely decays. Such decay measurements are immune from dephasing, as in population decay measurements of atomic, spin, and circuit quantum bits. For low-amplitude vibrations, we find that the amplitude decreases exponentially in time, as it is the case for a typical energy decay measurement (Fig. 8.1(a)). The decay rate is comparatively low and can correspond to quality factors surpassing 1 million. In the large vibration amplitude regime, the amplitude decays discontinuously (Fig. 8.1(b)). This comes as a surprise, since such a behavior has thus far never been observed nor predicted. This finding is robust as it is measured consistently in all the studied devices. This behavior shows that the energy decay is governed by nonlinear decay processes. We show that it can be related to the energy transfer to a higher energy eigenmode.

8.2 Device and setup

In order to perform high-precision energy decay measurements, also called ring-down measurements, we capacitively couple the graphene mechanical resonator to a superconducting microwave cavity (Fig. 8.1(c)). This allows us to detect the mechanical vibrations with a short time resolution, a high displacement sensitivity, and over a broad range of vibrational amplitudes [46, 163, 162]. The time resolution is limited by the inverse of the coupling rate of the cavity to the external readout circuit, which is on the order of $\kappa_{\mathrm{ext}}/2\pi \approx 1\,\mathrm{MHz}$ in our devices. High displacement sensitivity with minimal heating is demonstrated by resolving thermal motion at about 50 mK, corresponding to $n_{\mathrm{m}} \approx 25$ quanta of vibrations (see Fig. 8.1(d)). In order to reduce heating from the pump field used to detect the vibrations, we use multilayer graphene which has a higher electrical conductance and a higher heat capacity than single layer graphene (see Sec. 7.8), and we evaporate gold onto the superconducting contacts to improve the heat flow out of the graphene membrane [176, 163]. The displacement sensitivity can be further improved using a near quantum-limited Josephson parametric amplifier (JPA) [46, 184]. We use a double cavity JPA [184] for the readout of devices with comparatively low signal output. In energy decay measurements, we typically record vibrations with amplitudes ranging from 1 pm to 1 nm.

Energy decay measurements are carried out by preparing the resonator in an out-of-equilibrium state with a capacitive driving force, then switching the drive off and measuring the vibrational amplitude as the mechanical energy freely decays (Fig. 8.2(a)). We measure the decay with a time-resolved acquisition scheme combined with real-time digital signal processing (dashed box in Fig. 8.1(c)). Specifically, we record the two quadratures of motion, which are digitally squared to compute the vibrational energy. Energy decay traces are obtained by averaging typically 1000 measurements and subtracting a time independent noise background that is related to the amplifier chain. All the measurements presented in the following are carried out at 15 mK. We choose to display decay traces in terms of vibration amplitude instead of energy. We present data of 3 devices.

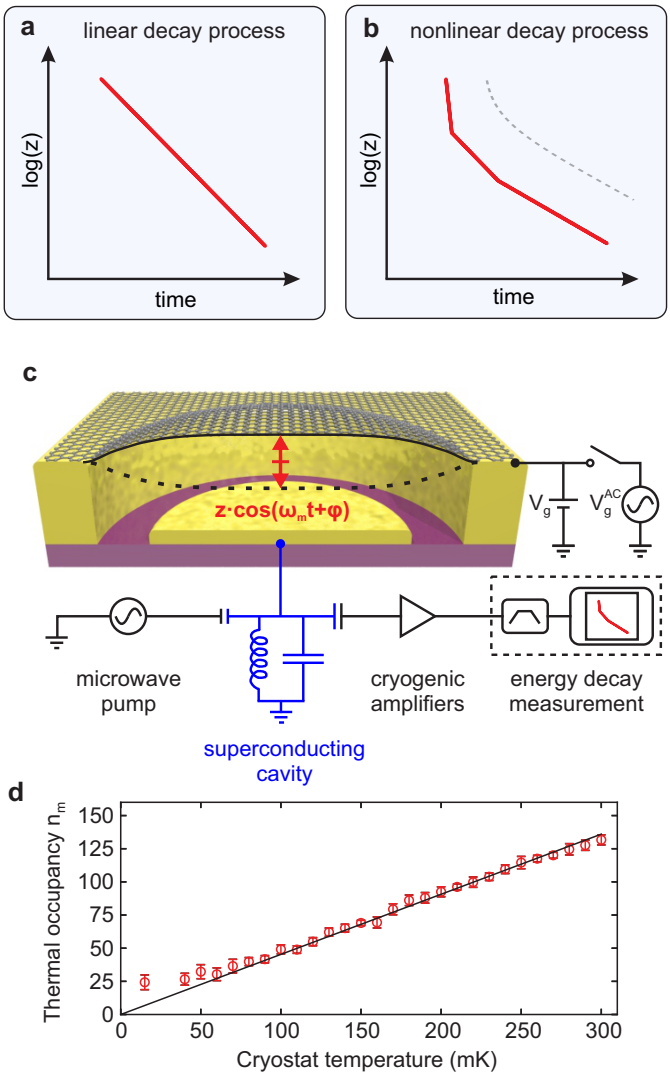

Figure 8.1: **Energy decay measurement: Setup and device characterization.** (**a**) Time-resolved energy decay measurement governed by linear decay processes. (**b**) Energy decay measurement in the presence of nonlinear decay processes as observed in this work (red trace). The gray dashed line corresponds to the decay expected from previous spectral measurements and theoretical works. The energy decay measurements in **a** and **b** are unaffected by dephasing and conservative nonlinear forces. (**c**) Measurement setup with schematic cross-section of a circular graphene drum vibrating as $z \cdot \cos(\omega_{\mathrm{m}} t + \phi)$. ϕ can vary in the course of the decay. The motion is detected with the superconducting microwave cavity. After cryogenic amplification, the output signal of the cavity is recorded and digitally computed to obtain the energy and the frequency of the vibrations as a function of time. (**d**) Average number n_{m} of vibration quanta as a function of the cryostat temperature. We obtain n_{m} from the integrated area of thermal resonances in spectral measurements.

8.3 Linear energy decay

This measurement scheme allows us to observe record high quality factors in graphene-based resonators (Fig. 8.2(b)). The measured amplitude z decays exponentially in time as $z^2 \propto e^{-\Gamma_{\mathrm{eff}}^{\mathrm{decay}} t}$ with an energy decay rate $\Gamma_{\mathrm{eff}}^{\mathrm{decay}} \approx 1/(3.6\ \mathrm{ms})$ (gray dashed line). This value corresponds to a quality factor Q_{m} exceeding 1 million. This Q-factor measured in a resonator made of graphene with 5-6 layers is 10 times larger than that with 1 to 3 layers [22] (see chapter 6) and 5 times larger than that with ≈ 30 layers [162]. By collecting energy decay traces using different drive frequencies near the resonant frequency ω_{m}, we show that the mechanical Q-factor is independent of the drive frequency and the vibrational amplitude induced by the driving force (Fig. 8.2(c)). The traces in Fig. 8.2(b) are shifted in time to show that they have the same decay rate.

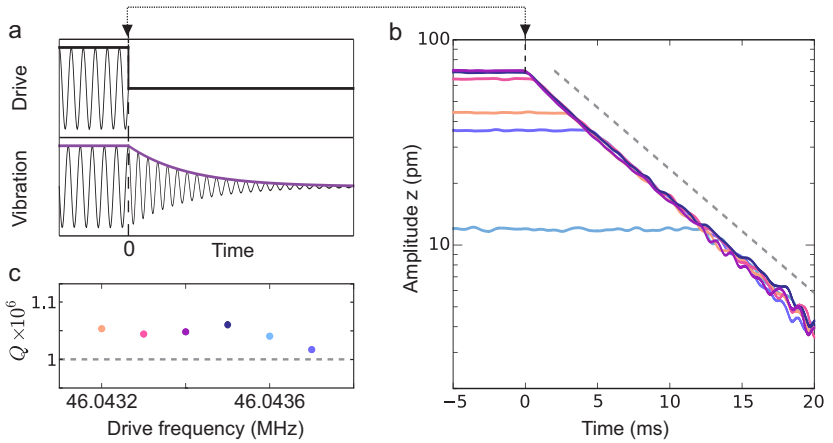

Figure 8.2: **Energy decay measurements in the low vibrational amplitude regime in device B.** (**a**) Measurement principle. At time $t = 0$ the mechanical driving force is switched off and the vibrational amplitude starts to decay. (**b**) Measured energy decay of the vibrational amplitude of device B as a function of time for different drive frequencies (see colors in **c**). The lower amplitude traces are shifted in time so all decaying curves overlap. The dashed grey line indicates an exponential decay corresponding to a Q-factor of 1 million. (**c**) The quality factor as a function of drive frequency. We apply $V_{\mathrm{g}} = 0.6$ V and pump the cavity with $n_{\mathrm{p}} \approx 1200$ photons.

What makes the observation of such high Q-factors possible is (i) the fact that our technique is immune from dephasing, (ii) the thermalization of the sample with the cryostat down to base temperature, and (iii) our ability to resolve small displacements without heating. Further, it is crucial to measure the energy decay at small voltages V_{g} applied between the graphene flake and the superconducting cavity. We discuss these points in detail for device B in the following.

8.3.1 Comparison between $\Gamma_{\mathrm{m}}^{\mathrm{decay}}$ and $\Gamma_{\mathrm{m}}^{\mathrm{spectral}}$

Comparing the energy decay rate $\Gamma_{\mathrm{eff}}^{\mathrm{decay}}$ obtained from ring down measurements with the line width $\Gamma_{\mathrm{eff}}^{\mathrm{spectral}}$ of spectral thermal motion measurements reveals that dephasing is

significant (Fig. 8.3(a)). Thermal spectra are fitted with a Lorentzian (red lines) to extract $\Gamma_{\mathrm{eff}}^{\mathrm{spectral}}$. For comparison, the black dotted lines correspond to Lorentzian resonances with the width $\Gamma_{\mathrm{eff}}^{\mathrm{decay}}$ that is obtained from energy decay measurements. Figure 8.3(a) shows resonances at the cryostat base temperature, which is $T_{\mathrm{cryo}} = 15$ mK. $\Gamma_{\mathrm{eff}}^{\mathrm{spectral}} \approx 2\pi \times 300$ Hz is more than twice as large as $\Gamma_{\mathrm{eff}}^{\mathrm{decay}} \approx 2\pi \times 130$ Hz. Dephasing accounts for about 50% of the spectral line width. Spectral measurements and energy decay measurements are both obtained with $n_{\mathrm{p}} = 1.9 \cdot 10^5$ and $V_{\mathrm{g}} = 0$ V. This value of n_{p} leads to heating as we will discuss below in section 8.3.3.

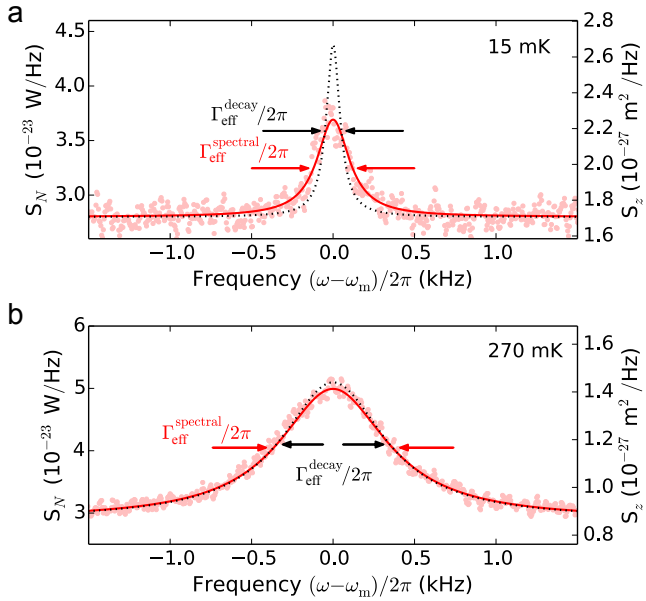

Figure 8.3: **Comparison of spectral line-width and energy decay rate in device B.** (**a**) Power spectral density at the output of the cavity (S_N) and displacement spectral density (S_z) of a typical thermal motion spectrum measured at $T_{\mathrm{cryo}} = 15$ mK (light red data points), yielding $\Gamma_{\mathrm{eff}}^{\mathrm{spectral}}/2\pi = 300$ Hz. Using the same n_{p} and V_{g}, we obtain $\Gamma_{\mathrm{eff}}^{\mathrm{decay}}/2\pi = 130$ Hz from energy decay measurements. The corresponding spectrum is plotted as a black dotted Lorentzian. We set $n_{\mathrm{p}} = 1.9 \cdot 10^5$ and $V_{\mathrm{g}} = 0$ V. (**b**) Thermal spectrum at $T_{\mathrm{cryo}} = 270$ mK, yielding $\Gamma_{\mathrm{eff}}^{\mathrm{spectral}}/2\pi = 800$ Hz. We get $\Gamma_{\mathrm{eff}}^{\mathrm{decay}}/2\pi = 760$ Hz from energy decay measurements. These measurements are recorded with $n_{\mathrm{p}} = 3.8 \cdot 10^5$ and $V_{\mathrm{g}} = 0$ V.

The difference between $\Gamma_{\mathrm{eff}}^{\mathrm{spectral}}$ and $\Gamma_{\mathrm{eff}}^{\mathrm{decay}}$ is greatly reduced at higher temperature. For instance, the difference is suppressed to 40 Hz at 270 mK (Fig. 8.3(b)). Dephasing accounts for about 5% of the spectral line width.

8.3.2 Temperature dependence of the energy decay rate

The ability to probe the decay rate of device B down to 15 mK allows us to reveal an intriguing temperature (T) dependence of the decay rate. Figure 8.4(a) shows that the T dependence of $1/Q_{\mathrm{m}}$ is stronger at low temperature than at high temperature. Comparing

the measured T dependence of $1/Q_{\rm m}$ to a power law, as often done with mechanical resonators, the data can be described by $1/Q_1 \propto T$ below 300 mK and $1/Q_2 \propto T^{1/3}$ above 300 mK. The behavior above 300 mK is similar to that reported by other groups in the same temperature range [24, 25, 8].

These data cannot be accounted for by two independent dissipation channels with decay rates proportional to $1/Q_1$ and $1/Q_2$. Indeed, in such a scenario, the total decay rate would be proportional to $1/Q_{\rm tot} = 1/Q_1 + 1/Q_2$, so that the exponent of the power law below 300 mK should be lower than that above 300 mK. This is just the opposite of what is observed in Fig. 8.4(a), indicating that this scenario where each power law corresponds to a different dissipation channel is not possible.

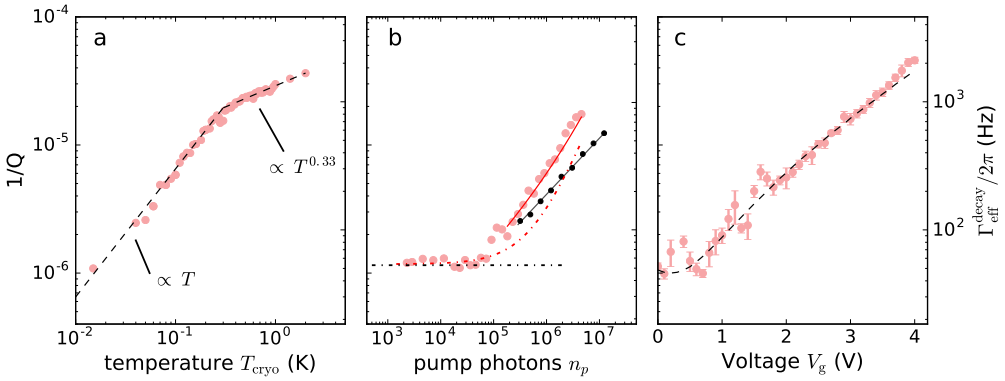

Figure 8.4: **Energy decay as a function of different parameters in the low vibrational amplitude regime in device B**. (**a**) Temperature dependence of energy decay rate. The measurement is recorded at $n_{\rm p} = 1200$ and $V_{\rm g} = 0\,{\rm V}$. For temperatures below $T_{\rm cryo} = 300\,{\rm mK}$ the data is in agreement with a linear temperature dependence. Above $T_{\rm cryo} = 300\,{\rm mK}$ the dependence is $1/Q_{\rm m} \propto T^{1/3}$. (**b**) Dependence of the energy decay rate on cavity pump photons, when pumping the cavity either on the red sideband (light red points) or on cavity resonance (black points). This measurement is performed at $T_{\rm cryo} = 15\,{\rm mK}$ and $V_{\rm g} = 0\,{\rm V}$. The dashed-dotted red line corresponds to $\Gamma_{\rm eff}^{\rm decay} = \Gamma_{\rm m}^{\rm decay} + \Gamma_{\rm opt}$ where $\Gamma_{\rm m}^{\rm decay}$ is the intrinsic decay rate obtained at low $n_{\rm p}$. The continuous red line is obtained by including the effect of Joule heating, that is, by taking into account the $n_{\rm p}$ dependence of $\Gamma_{\rm m}^{\rm decay}$ (black line). (**c**) Energy decay as a function of $V_{\rm g}$. This measurement is recorded with $n_{\rm p} = 1200$ at $T_{\rm cryo} = 15\,{\rm mK}$. The dashed black line is a fit to the data including motion induced displament currents in the graphene membrane.

This measured T dependence of $1/Q_{\rm m}$ might be related to the coupling of the graphene resonator to two-level systems (TLS) [185, 186, 187, 8]. Indeed, TLSs can lead to a temperature variation of $1/Q_{\rm m}$ that is large at low temperature and weak at high temperature, in agreement with the observed T dependence of $1/Q_{\rm m}$ in Fig. 8.4(a). The microscopic origin of the TLS is not clear, but it might be related to contamination adsorbed at the surface of the graphene flake or charge fluctuators localized at the surface of the bottom electrode.

8.3.3 Pump photon number dependence of the energy decay rate

In order to detect the highest mechanical quality factors it is essential to resolve the mechanical motion with a very weak pump field to avoid heating of the mechanical resonator (see Fig. 8.4(b)). We plot $\Gamma_{\rm eff}^{\rm decay}$ as a function of the number $n_{\rm p}$ of pump photons in the cavity for device B at the cryostat temperature $T_{\rm cryo} = 15$ mK (light red data points in Fig. 8.4(b)). For $n_{\rm p} < 10^5$, we observe that the decay rate $\Gamma_{\rm m}^{\rm decay}/2\pi \approx 50$ Hz remains constant over a large range of $n_{\rm p}$. Upon increasing $n_{\rm p}$ above 10^5, $\Gamma_{\rm eff}^{\rm decay}$ gets larger. We show below that the increase of $\Gamma_{\rm eff}^{\rm decay}$ is due both to optomechanical damping and to Joule heating induced by the pump electromagnetic field. These data are recorded by pumping the cavity on the red detuned sideband $\omega_p = \omega_c - \omega_m$. The resulting optomechanical damping $\Gamma_{\rm opt} = 4n_{\rm p}g_0^2/\kappa$, shown with the red dashed-dotted line in Fig. 8.4(b), is lower than the measured $\Gamma_{\rm eff}^{\rm decay}$. This indicates that optomechanical damping alone cannot account for our data.

We quantify the effect of Joule heating by pumping the cavity at $\omega_{\rm p} = \omega_{\rm c}$ and recording energy decay traces at both $\omega_{\rm c}-\omega_{\rm p}$ and $\omega_{\rm c}+\omega_{\rm p}$. Pumping at $\omega_{\rm p} = \omega_{\rm c}$ leads to $\Gamma_{\rm opt} = 0$ Hz. We observe that $\Gamma_{\rm eff}^{\rm decay}$ gets larger upon increasing $n_{\rm p}$ (black data points in Fig. 8.4(b)). This increase of $\Gamma_{\rm eff}^{\rm decay}$ is attributed to Joule heating. This measurement can be described by $\Gamma_{\rm eff}^{\rm decay} \propto n_{\rm p}^{0.43}$ (black line in Fig. 8.4(b)). By adding this $n_{\rm p}$ dependence of $\Gamma_{\rm eff}^{\rm decay}$ due to Joule heating together with $\Gamma_{\rm opt} = 4n_{\rm p}g_0^2/\kappa$, we quantitatively reproduce the measurement of $\Gamma_{\rm eff}^{\rm decay}$ as a function of $n_{\rm p}$ (red line in Fig. 8.4(b)).

8.3.4 Gate dependence of energy decay rate

Figure 8.4(c) shows $1/Q_{\rm m}$ as a function of the DC voltage $V_{\rm g}$ applied between the graphene flake and the cavity for device B. The mechanical quality factor decreases from $Q_{\rm m} \approx 10^6$ at $V_{\rm g} = 0$ V down to $Q_{\rm m} \approx 2 \times 10^4$ at $V_{\rm g} = 4$ V. We attribute this reduction of $Q_{\rm m}$ to electronic Joule dissipation [23, 146], a mechanism which arises from the motion-induced displacement current through the graphene flake. Indeed, the data can be quantitatively described by $1/Q_{\rm m} = 1/Q_0 + 1/Q_{\rm Joule}$ with a $V_{\rm g}$ independent contribution $Q_0 = 10^6$ and

$$\frac{1}{Q_{\rm Joule}} = \frac{R_{\rm eff}}{m_{\rm eff}\omega_{\rm m}}\Big(\frac{\partial C_{\rm m}}{\partial z}\Big)^2 V_{\rm g}^2. \tag{8.1}$$

Here, $R_{\rm eff}$ is an effective electrical resistance. We take into account an offset in $V_{\rm g}$ of 0.25 V observed in the $V_{\rm g}$ dependence of $\omega_{\rm m}$. This offset is attributed to the work function difference between the graphene flake and the cavity counter-electrode. In order to evaluate the derivative of the capacitance with respect to displacement as a function of $V_{\rm g}$, we calculate $\partial C_{\rm m}/\partial z$ using a local plate capacitor approximation (see Eq. 6.8) and compare the obtained values with $\Delta C_{\rm m}$ measured from the dependence of the cavity resonance frequency $\omega_{\rm c} = 1/\sqrt{LC_{\rm tot}}$ on $V_{\rm g}$ where we use $\Delta C_{\rm m} = \Delta C_{\rm tot}$.

From a comparison of the measurement in Fig. 8.4(c) to Eq. 8.1 we obtain $R_{\rm eff} = 220\ \Omega$. This value is comparable to the sheet resistance $0.3 - 1$ kΩ of few-layer graphene at low temperatures [188]. We emphasize that a direct comparison between $R_{\rm eff}$ and the sheet resistance is nontrivial, because of the difficulty to reflect the exact geometry associated with $R_{\rm eff}$. By doing the same analysis for device A, the $V_{\rm g}$ dependence of $1/Q_{\rm m}$ can be described by electron Joule dissipation using $R_{\rm eff} = 480\ \Omega$.

8.4 Nonlinear energy decay

In the high vibrational amplitude regime, our high-precision measurements reveal that energy decays discontinuously (Fig. 8.5(a,b)). This behavior is strikingly different from what is commonly expected for mechanical resonators. This finding is robust, since it is observed in all the studied resonators. The discontinuous decay does not depend on the initial amplitude nor the frequency of the driving force. However, what strongly affects the vibration amplitude associated with the discontinuity of the decay is the static voltage V_{g} applied between the graphene resonator and the cavity. This suggests that the discontinuity of the decay is related to ω_{m}, since the variation of V_{g} strongly modifies the resonant frequency of mechanical modes.

During the decay in the high amplitude vibrational regime, we also monitor the continuous variation of the resonance frequency induced by the nonlinearity of the restoring force (Fig. 8.5(c)). The frequency is computed using the short time Fourier transformation of the vibrations recorded during the decay. After the drive is stopped, the frequency decays smoothly to the natural, i.e. un-driven, resonance frequency ω_0. When comparing the smooth frequency decay and the vibrational amplitude decay (red trace in Fig. 8.5(a)), we find that the frequency depends quadratically on the vibrational amplitude (Fig. 8.5(d)). This is the behavior expected from the nonlinearity of the restoring force at low-amplitude vibrations, which scales as $F_{\mathrm{nl}} \propto z^3$ [78]. This shows that the bandwidth of our signal filtering is wide enough to let us record the frequency-dependent vibrations during the decay.

In addition to the smooth decay of the eigenfrequency, we observe a jump in frequency from ω_{d} to ω_{max} in Fig. 8.5(c). The jump is faster than the time resolution of the Fourier transformation. Furthermore, the jump is consistent with the dynamics of a resonator when it undergoes the transition between the driven and the non-driven regime (see inset in Fig. 8.5(c)). In the driven regime, the resonator is forced to oscillate at ω_{d}, whereas the eigenfrequency $\omega_{\mathrm{m}}(z)$ of a resonator in the non-driven regime only depends on the vibrational amplitude, as indicated by the red line in the inset of Fig. 8.5(c). The jump from ω_{d} to ω_{max} is expected to be quasi-instantaneous, as the motion during the free decay has no frequency memory and depends only on the initial displacement and velocity at $t = 0$. Since the total energy of the resonator $E_{\mathrm{m}} = \frac{1}{2} m_{\mathrm{eff}} \omega(t)^2 z(t)^2$ remains constant over $t \ll 1/\Gamma_{\mathrm{decay}}$, the observed jump in ω should in principle be associated with a change in z. For the observed 15 kHz jump in ω, the corresponding 50 fm change in z is however below the resolution of our measurement.

The abrupt variations in the decay contrasts with expectations from previous works on nonlinear dissipation [22, 80, 189, 190]. Recent spectral measurements have shown that dissipation in nanomechanical resonators can depend on the vibration amplitude. Following the abundant theoretical literature on the subject [179, 78, 191], these measurements have been interpreted in terms of a smooth dependence of the energy decay rate on the vibrational amplitude, which scales as $\Gamma_{\mathrm{decay}} \propto z^2$ (dashed gray line in Fig. 8.1(b)). Here we show that the measured energy decay cannot be described by the energy decay predicted by the dissipative force $F = \eta z^2 \dot{z}$. For this, we extract η and the duffing parameter α from spectral measurements and compare the obtained prediction of the energy decay (see cf. Eq. 3.31)

$$z^2(t) = z_0^2 \cdot \frac{\exp\left[-\frac{t}{\tau}\right]}{1 + \frac{2\eta}{8m_{\mathrm{eff}}} \cdot \tau \cdot z_0^2 \cdot \left(1 - \exp\left[-\frac{t}{\tau}\right]\right)} \tag{8.2}$$

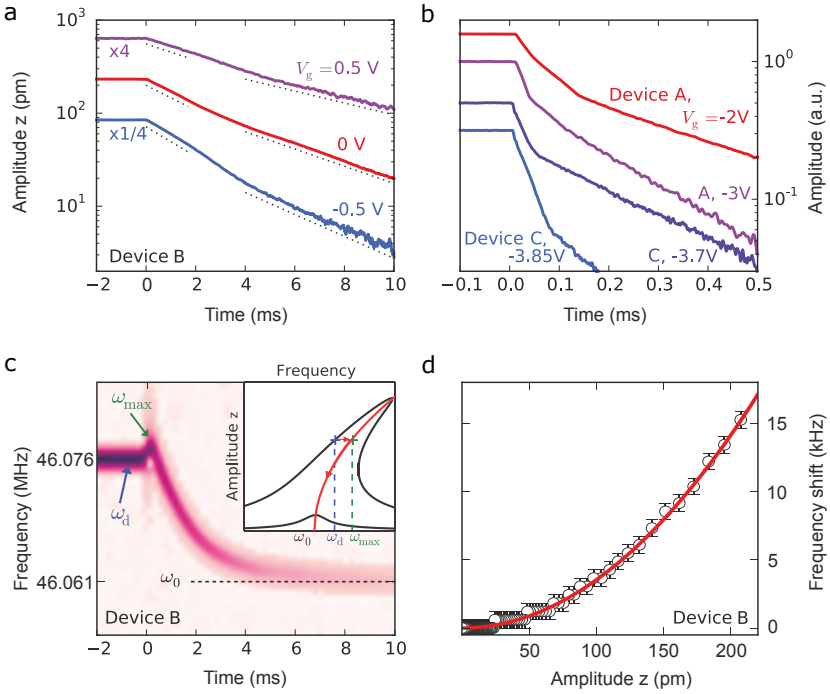

Figure 8.5: **Energy decay in the high vibrational amplitude regime.** (**a,b**) Energy decay measurements at different V_g for devices A, B, and C. In all cases, the decay is discontinuous. The bandwidth of the bandpass filter in **a** is 150 kHz for the violet and red traces and 200 kHz for the blue trace. The bandwidth is 400 kHz and 200 kHz for devices B and C in **b**, respectively. (**c**) Time dependence of the short time Fourier transform of the vibrations corresponding to the red amplitude decay trace in **a**. **Inset**, Schematic showing the relation between the driven spectral response (black) and the free decay (red). The two black curves correspond to the driven spectral response for high and low driving force amplitudes. When the driving force is stopped, the vibration frequency switches from ω_d to ω_{max} and then evolves during the decay along the amplitude dependent eigenfrequency towards ω_0. (**d**) Frequency shift as a function of vibrational amplitude. The quadratic dependence (red line) is in agreement with the frequency pulling expected from the nonlinear restoring force at low vibration amplitude.

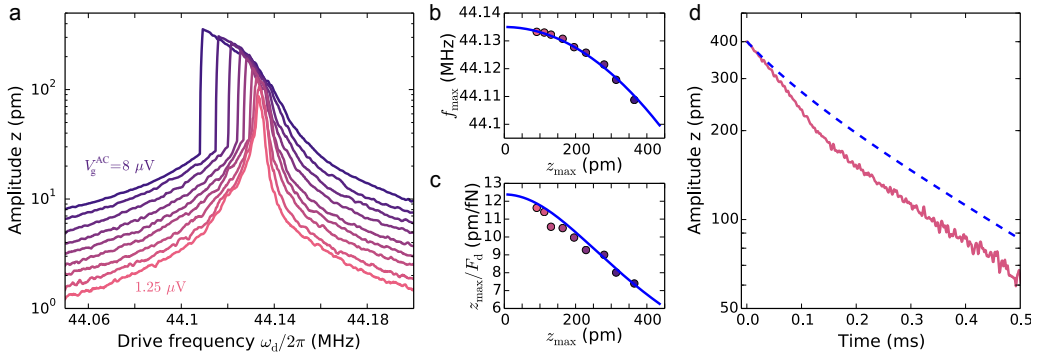

Figure 8.6: **Spectral measurements compared to energy decay measurements in device C.** (**a**) Spectral response of the driven motion for increasing drive voltage V_g^{AC} with ω_d swept from high to low frequency. The measurement is recorded at intermediate vibration amplitude with $V_g = -3.3$ V. (**b**) Plot of f_{max} as a function of z_{max}. From the fit with a nonlinear Duffing restoring force, we extract $\alpha = -5 \cdot 10^{16}$ kg/m^{2}s^2 and $\omega_0 = 44.135$ MHz. (**c**) Plot of z_{max}/F_d as a function of z_{max}. The data can be fitted with $\eta = 6 \cdot 10^6$ kg/m^{2}s and $Q_m = 55\,000$. (**d**) Comparison between energy decay measurement (red line) and prediction with the dissipative force $F = \eta z^2 \dot{z}$ (blue dashed line).

with the measurement (Fig. 8.6). Here, $z_0 = z(t = 0)$ and $\tau = Q_m/\omega_m$. Figure 8.6(a) shows the driven spectra of device C recorded for different driving force amplitudes F_d. We extract z_{max} and $\Delta\omega_m$ for each spectrum. From the plots of $\Delta\omega_m$ and z_{max}/F_d as a function of z_{max} (Figs. 8.6(b,c)), we get that $\alpha = -5 \cdot 10^{16}$ kg/m^{2}s^2, $\eta = 6 \cdot 10^6$ kg/m^{2}s, and $Q = 55\,000$ using Eqs. 3.22 and 3.25. Here we use $m_{eff} = 60$ fg from section 8.6.1. Figure 8.6(d) shows that the measurement of the energy decay is not described by Eq. 3.31 using the values of α, η, and Q_m determined above. To conclude, this analysis indicates that spectral measurements have to be used with care when quantifying nonlinear dissipation. While spectral measurements can be described with $F = \eta z^2 \dot{z}$ in a satisfactory way, energy decay measurements show a strong deviation from such a dissipation process.

8.4.1 Mode-mode coupling

The physical origin of the observed discontinuous decay can be related to a nonlinear decay process. Figures 8.7(a,b) show that the first discontinuity in the decay is related to a peculiar saturation in the spectral response of the vibrational amplitude to the driving force. This saturation is a phenomenon occurring in nanomechanical resonators due to mode-mode coupling over a so-called internal resonance [192, 138]. Indeed, we observe a higher eigenmode with resonance frequency $\omega_{high} = 3 \times \omega_m$ at the V_g value for which the saturation occurs. Figure 8.8(a) shows the resonant frequency of the lowest energy mechanical modes of device C as a function of the DC voltage V_g applied between the graphene flake and the cavity. The resonant frequencies are extracted from driven spectra recorded with a high driving force amplitude and a high pump power ($V_g = 120\,\mu$V, $P_{pump} = 13$ mW at the input of the cryostat). We identify 7 mechanical modes. Six of them can be clearly resolved from spectral measurements, whereas the mode labeled

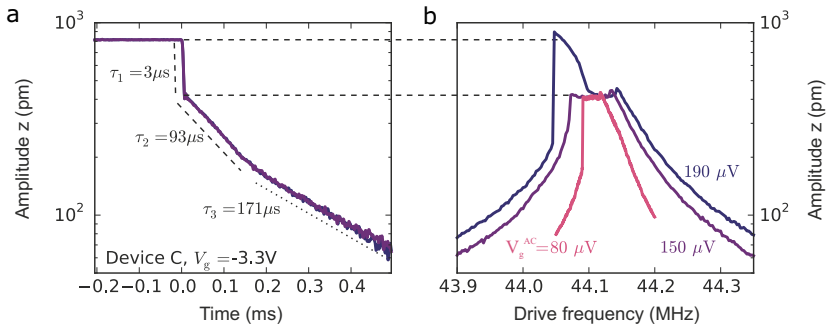

Figure 8.7: **Relation between kink in energy decay and plateau in spectral measurement in device C**. (**a**) Decay trace with an extreme change of the energy decay rate ($\tau_2 \geq 30 \times \tau_1$). The initial decay time is limited by the digital filter bandwidth of 200 kHz. Shifting the center frequency of the band-pass filter by 30 kHz does not affect the measurement as indicated by the purple and blue traces that are on top of each other. (**b**) Driven spectra for different mechanical driving voltages V_g^{AC} recorded with the same V_g as in **a**. The spectra show a saturation in the vibrational amplitude. This amplitude is the same as that of the abrupt change of the energy decay in **a**.

(4) is inferred from the anti-crossing behavior observed in the V_g dependence of the resonant frequency of the modes labeled (5) and (6). In the anti-crossing region shown in Fig. 8.8(b), the vibrations are the result of the hybridization of mode (4) and mode (6). At $V_g = -3.3$ V the resonant frequency of this hybridized mode (indicated by the red point in Fig. 8.8(b)) is three times larger than the resonant frequency of the fundamental mode, labeled (1) and shown in Figs. 8.7(a,b).

The abrupt variation of the decay rate is related to nonlinear mode coupling. This can be explained by a model where the fundamental mode hybridizes with other modes of the resonator at high energy [193]. This nonlinear mode-coupling has the peculiarity of enabling energy transfer between vibrational modes even if resonant frequencies are far apart and the coupling strength depends on the vibrational amplitude. For this to happen, the ratio of resonant frequencies ω_n/ω_1 (ω_n is the frequency of a higher order mode) has to be close to an integer n [137, 138, 192]. At high vibrational amplitude, the modes hybridize, and decay in unison with $(\Gamma_1 + \Gamma_n)/2$ (Γ_1 (Γ_n) is the decay rate of the mode at low (high) frequency). At low amplitude, the two modes are decoupled and decay with their individual decay rates. As a result, the flow of energy takes different paths during an energy decay measurement of the fundamental mode. At high amplitude, the energy of the vibrations is transferred into the bath of the fundamental mode directly, and into the vibrations and the bath of the higher order mode and at low amplitude, the dissipation channel to the bath of the higher order mode is closed.

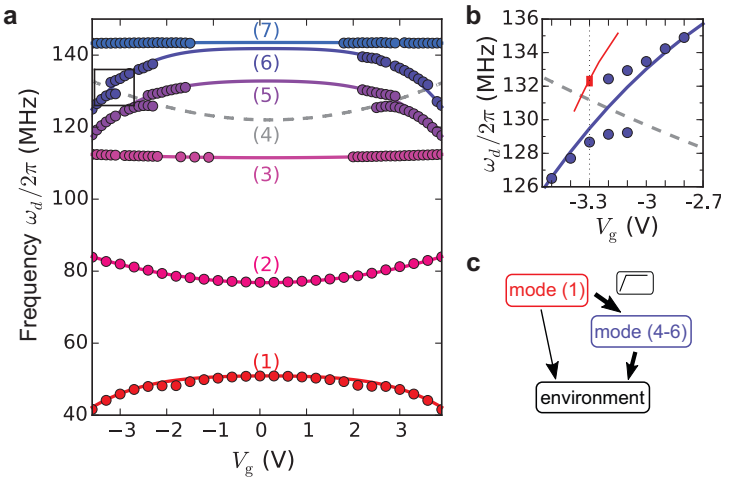

Figure 8.8: **Mode spectrum and internal resonance in device C.** (**a**) Fundamental and higher mechanical mode spectrum extracted from driven measurements. (**b**) Zoom of area marked in **a**. Around 132.2 MHz and $V_g = -3.3$ V, the resonance frequency of the mode at $\omega_{high}/2\pi \approx$ 132.3 MHz is commensurate with $3 \times \omega_m$ of the fundamental mode at high driving (red line). The extent of the red data point at $V_g = -3.3$ V indicates the frequency range of the saturation in the driven spectrum of the fundamental mode multiplied by three (Fig. 8.7(b)). By detuning V_g the saturation frequency of the first mode shifts according to the red line. (**c**) Dissipation channels of mode (1). The dissipation channel through the higher mode (4-6) opens up above a threshold vibration amplitude when $\omega_m = \omega_{high}/3$.

8.5 Conclusions and outlook

The energy decay measurement at the highest vibrational amplitudes in Fig. 8.7(b) can be associated to nonlinear mode-mode coupling. The energy of the first eigenmode is transferred to the higher eigenmode, which is subsequently dissipated into the thermal bath of the higher eigenmode. Below the vibrational amplitude of the saturation, this loss channel is switched off because of the nonlinear nature of the mode-mode coupling [137], resulting in the observed abrupt change of the energy decay. We note that many discontinuities of the decay are observed without any noticeable saturation in the response. Some of these discontinuities might be attributed to nonlinear decay processes involving the coupling between multiple quanta of vibrations of the fundamental mode and other degrees of freedom, such as graphene charge carriers and two-level systems, which we conclude from measurements in the low-amplitude regime [23, 8] (see Secs. 8.3.4 and 8.3.2, respectively).

The unexpected nonlinear energy decay opens up new possibilities to tune dissipation by electrostatic means and to manipulate vibrational states coherently [194, 195]. It will be interesting to study other systems, such as mechanical, electrical, and optical resonators, in order to test the universality of the nonlinear decay process reported in this work.

8.6 Additional information

8.6.1 Device Parameters

Important parameters of the measured devices are summarized in Table 8.1.

8.6.2 Measurement setup and energy decay

Figure 8.9 shows a detailed schematic of the measurement setup. Compared to the previous chapter, the setup is modified by an additional transmission input and by a Josephson parametric amplifier mounted at $T = 15\,\mathrm{mK}$. The JPA is connected at the directional coupler on the cancellation line, which is used to pump the JPA. The transmission measurement configuration, that is, coupling the cavity capacitively to both a weakly coupled input port and a strongly coupled output port ensures JPA compatible readout (for details on the device design see Sec. 5.1.2). In this configuration, the strong pump tone at $\omega_\mathrm{p} = \omega_\mathrm{c} - \omega_\mathrm{m}$, at the input of the JPA, is attenuated by $\approx 40\,\mathrm{dB}$ by the cavity line shape and additionally attenuated by the cancellation, which prevents saturation of the JPA. On the weakly coupled transmission input line we use a 10 dB Pasternack PE2204 directional coupler. We do not need to cancel the JPA pump tone as the double cavity design [184] allows to pump the JPA with a detuning of ≈ 200 MHz from the signal. An additional SIM928 DC voltage source is used to generate a current through a flux coil underneath the JPA and thereby tune the frequency of the JPA amplification band.

Energy decay setup and methods

A detailed schematic of the energy decay measurement setup is shown in Fig. 8.10. To stop the mechanical drive signal and initiate the energy decay, we use a ZASW-2-50DR+ RF

	Device A	Device B	Device C
Cavity	CPW	CPW	CPW
Weak port, transmission	No	Yes	Yes
JPA read out	No	No	Yes
$\omega_c/2\pi$ (0 V)	7.42 GHz	7.49 GHz	7.44 GHz
$\kappa_{tot}/2\pi$ (0 V)	1.6 MHz	2.5 MHz	3.25 MHz
$\kappa_{ext}/2\pi$ (0 V)	850 kHz	1.7 MHz	1.32 MHz
$\kappa_{int}/2\pi$ (0 V)	750 kHz	850 kHz	1.93 MHz
Graphene device			
Exfoliated with	Scotch tape	PDMS	Scotch tape
Drum radius	1.6 μm	1.65 μm	1.6 μm
Cavity electrode radius	1.2 μm	1.1 μm	1.1 μm
Graphene cavity-electrode separation	88 nm	85 nm	90 nm
Graphene contacts	Nb	Nb and Au	Nb
$\omega_m/2\pi$	70 MHz (0 V)	46 MHz (0 V)	47 MHz (-2.6 V)
Effective mass	$25 \times m_{eff,0}$	$5.5 \times m_{eff,0}$	$35 \times m_{eff,0}$
Graphene resistance	480 Ω	220 Ω	-
Coupling			
$g_0/2\pi$	9.7 Hz (0 V)	7.3 (0 V)	2.95 Hz (-3.3 V)

Table 8.1: **Device parameters.** The effective mass m_{eff} of the few layer graphene drums is given in terms of the effective mass of a single layer graphene drum $m_{eff,0} \approx 1.6$ fg. The effective graphene resistance is estimated from the measured mechanical decay rate induced by electron Joule dissipation. The single photon coupling g_0 is calibrated from thermal motion measurements in device A and B. For device C the coupling is calibrated from the driven motion as described in Sec. 6.7. Note that devices A and B correspond to devices A and B from chapter 7, but the parameters for device A given here are from a different cool down.

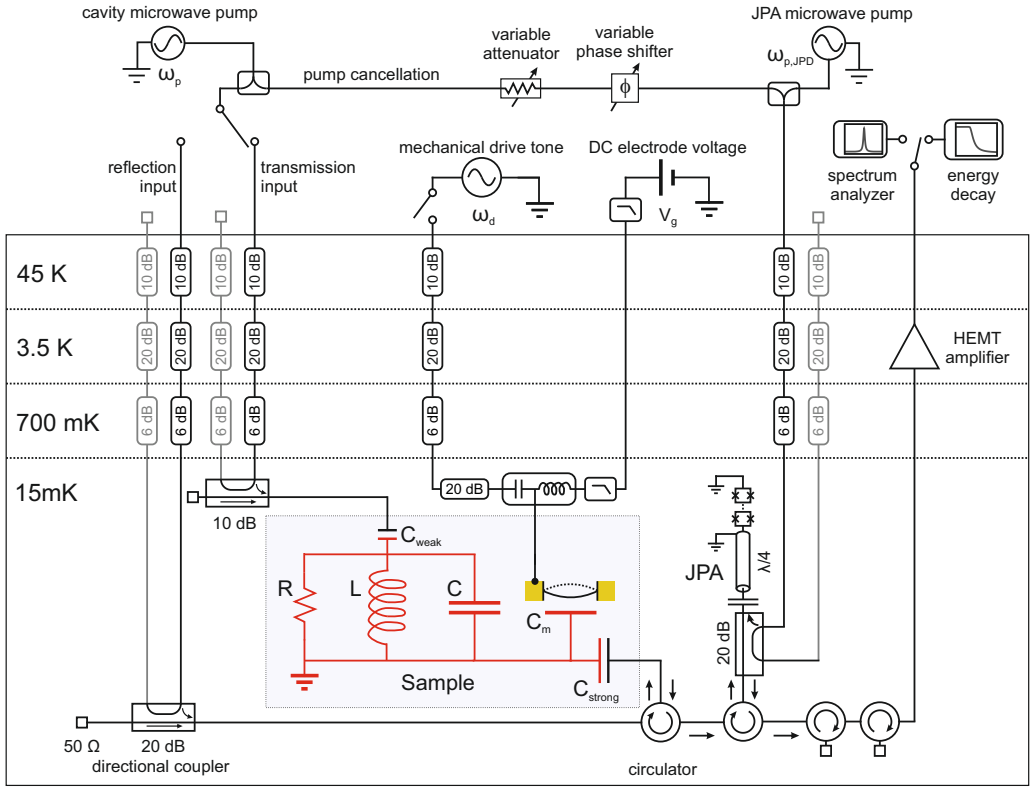

Figure 8.9: **Measurement setup with cryogenic wiring.**

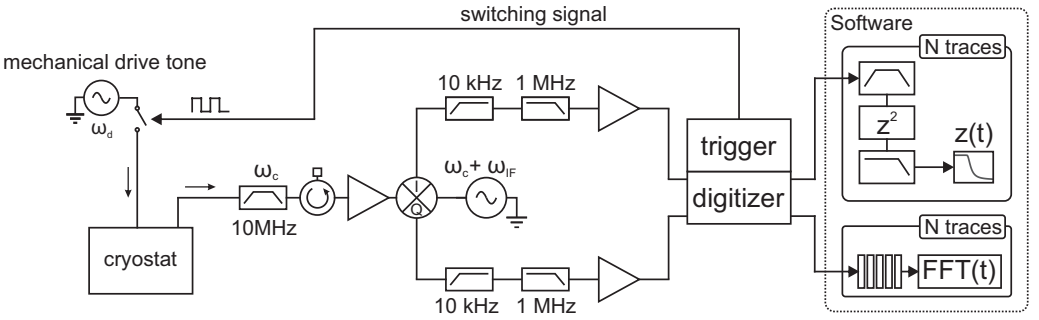

Figure 8.10: **Detailed energy decay measurement setup.**

switch from Mini-Circuits. The switch is triggered with a square-wave signal generated with a NI PXI 5451 AWG from National Instruments. Because of the optomechanical coupling, the mechanical response is frequency up-converted to the cavity resonance frequency ω_c. At the output of the cryostat, the signal at the pump frequency is attenuated with a tunable bandpass-filter WBCQV 7000/8000-6SSSD from Wainwright Instruments. This is to avoid saturation during amplification of the signal with the subsequent low-noise amplifiers AMF-4F-04000800-07-10P and AMF-3F-04000800-07-10P from MITEQ. To damp reflections from the amplifiers, isolators D3I6012 from Ditom are used in front of the amplifiers. The signal is down-mixed using an I-Q mixer IQ-4509LXP from Marki Microwave to the intermediate frequency $\omega_{IF} = 500$ kHz. The mixing tone is generated by a ZVB-14 from Rhode and Schwarz. The I and Q quadratures are independently filtered with a 1.9 MHz lowpass filter BLP 1.9+ from Mini-Circuits and amplified by a SR-560 preamplifier from Stanford Research. The preamplifier has an additional high pass filter at 10 kHz and a low pass filter at 1 MHz. We record the two quadratures using a two channel digitizer NI PXI 5114 from National Instruments. The digitizer and the trigger generator are synchronized with the internal PXI bus.

To record energy decay measurements we pump the cavity with an electromagnetic field with frequency $\omega_p = \omega_c - \omega_d$. Here, $\omega_c \approx 7.5$ GHz and $\omega_d \approx \omega_m$. The optomechanical coupling leads to an anti-Stokes scattered field around frequency ω_c. The signal is then down-mixed from ω_c to 500 kHz using an I/Q frequency mixer. The down-mixed signal is then digitized, digitally band-pass filtered around 500 kHz with bandwidth BW, squared and eventually low pass filtered with bandwidth $BW/2$. We set $BW \approx 2$ kHz for measurements with low vibrational amplitudes (Fig. 8.2), and $BW = 150 - 400$ kHz for measurements with large vibrational amplitudes in order to account for changes in the vibrational frequency of the mechanical resonator (Figs. 8.5 and 8.7). In order to subtract the amplifier noise contribution from the mechanical signal, we compute the time-averaged signal at the end of each decay traces (when the vibration amplitude is suppressed to zero). This noise subtraction has been applied for all amplitude ring-down measurements presented throughout this chapter.

The vibration frequency during the decay is obtained with short time Fourier transform (STFT). This method is suitable for the analysis of signals with time-varying frequency spectrum. We use a Hamming apodization function to segment the signal in temporal windows. Such a process allows us to reduce spectral components that are due to the temporal window itself, while keeping a good frequency resolution of the analyzed signal.

For a time varying signal $z(t)$, its STFT is expressed as

$$Z(t,\omega) = \int_{-\infty}^{+\infty} z(t') \cdot \mathrm{Ham}(t-t') \cdot e^{-j\cdot\omega\cdot t'} dt'. \tag{8.3}$$

We use a Hamming apodization function $\mathrm{Ham}(t)$ with a window width of 200 μs. The STFT is calculated with a frequency resolution of 610 Hz. The plotted STFT at time t is the average of the STFT of 1000 individual energy decay traces (Fig. 8.5(c)).

8.6.3 Calibration of cavity transmission

We formally treat cavities that contain a weakly coupled input port and a strongly coupled output port as cavities with a single port, because we do not have the possibility to determine precisely the coupling rate κ_{weak} of the weak port. To justify this treatment, we make use of the fact that the external cavity loss over the weak port is negligible $\kappa_{\mathrm{weak}} < 2\pi \cdot 60\,\mathrm{kHz} \ll \kappa_{\mathrm{strong}}$, which is determined by prior measurement of the respective cavity at $T = 4\,\mathrm{K}$. In this case, $\kappa_{\mathrm{ext}} = \kappa_{\mathrm{weak}} + \kappa_{\mathrm{strong}}$ can be approximated by $\kappa_{\mathrm{ext}} \approx \kappa_{\mathrm{strong}}$ and we can extract the cavity parameters from a reflection measurement using only the strongly coupled port.

In Fig. 8.11 we plot the reflected $|S_{11}|^2$ and transmitted $|S_{12}|^2$ power as well as the phase shift of the reflected signal at $T = 15\,\mathrm{mK}$ of device B. To extract the internal loss rate κ_{int} and the external coupling rate κ_{ext} we fit the line shape expected for a single-port reflection cavity (see cf. 4.25)

$$S_{11} = \frac{\kappa_{\mathrm{int}} - \kappa_{\mathrm{ext}} - 2i(\omega - \omega_{\mathrm{c}})}{\kappa_{\mathrm{int}} + \kappa_{\mathrm{ext}} - 2i(\omega - \omega_{\mathrm{c}})} \tag{8.4}$$

to the reflected power and to the phase shift of the reflected signal, respectively. We obtain $\kappa_{\mathrm{int}} = 0.8\,\mathrm{MHz}$ and $\kappa_{\mathrm{ext}} = 1.7\,\mathrm{MHz}$.

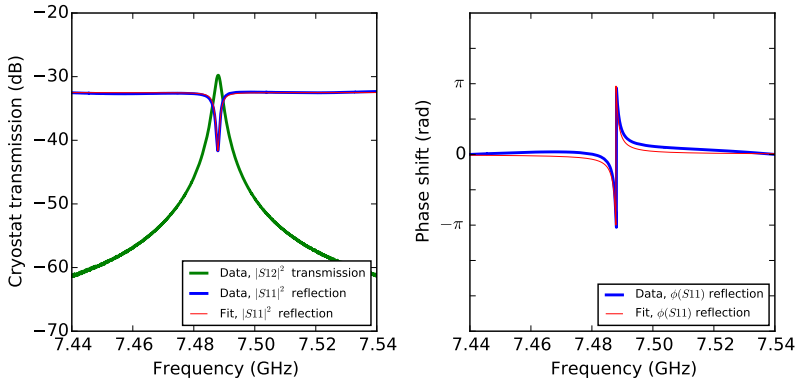

Figure 8.11: **Transmission and reflection measurement of the superconducting cavity in device A.** The measurements include the cryostat wiring and the cryogenic HEMT amplifier. The strongly coupled port is denoted with 1 and the weakly coupled port with 2.

Regarding the estimation of the intra-cavity photon number, we calibrate the transmission measurement configuration against the reflection measurement configuration. To

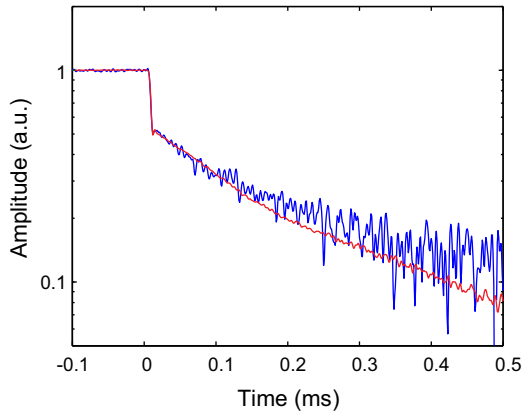

Figure 8.12: **Improvement of measurement quality with the Josephson parametric amplifier (JPA).** The figure shows the decay trace of Fig. 8.7(a) with the JPA turned on (red) and the measurement with the JPA pump switched off (blue).

estimate n_p in the transmission configuration, we use

$$n_\mathrm{p} = \frac{1}{\hbar\omega_\mathrm{p}} \cdot P_\mathrm{in} \cdot loss_\mathrm{weak} \cdot \frac{4\kappa_\mathrm{ext}}{\kappa^2 + 4(\omega_\mathrm{p} - \omega_\mathrm{c})^2} \tag{8.5}$$

where $loss_\mathrm{weak}$ is the effective loss coefficient when pumping the cavity at the weakly coupled port. We precisely determine $loss_\mathrm{weak} = loss + 2.5\,\mathrm{dB}$ with three different methods. All methods consist of comparing one particular output quantity for the two signal input configurations. In the first method, we measure the product $gain \cdot loss$ both for reflection and transmission. In transmission, we obtain $gain \cdot loss$ by measuring the transmitted power through the cryostat at ω_c (green curve in Fig. 8.11). This is compared with $gain \cdot loss$ from the reflection measurement at ω_p. The second and third methods compare the driven mechanical vibration amplitude and the total mechanical dissipation rate $\Gamma_\mathrm{eff}^\mathrm{decay}$ obtained from energy decay, respectively, when pumping the cavity red detuned, both for reflection and transmission.

8.6.4 Noise reduction with the JPA

The JPA significantly improves the detection efficiency of energy decay measurements, as illustrated in Fig. 8.12. The red trace is recorded with the JPA turned on, while the blue trace corresponds to the measurements with the JPA switched off (same measurement as Fig. 8.7(a)). For the chosen gain of 26 dB we observe a noise rise of 15 dB in spectral measurements when turning on the JPA. As a result, the effective system noise is dominated by the noise of the JPA with only a small contribution from the HEMT noise and cable losses after the JPA. The JPA used in our setup has been demonstrated to operate close to the quantum limit [184].

Chapter 9

Conclusions

9.1 Summary

In this dissertation, we investigated few-layer and multilayer graphene mechanical resonators capacitively coupled to superconducting microwave cavities. We showed that this coupling scheme is a very powerful approach to study graphene mechanical resonators, both in terms of the mechanical properties, but also for force and mass sensing applications.

In chapter 6, we presented the first proof-of-principle implementation of coupled graphene-cavity devices and confirmed that the optomechanical Hamiltonian can be applied to this system. Although the devices in this chapter suffered from high internal decay rate of the superconducting cavity, the obtained results demonstrate state-of-the-art readout of graphene nanomechanical motion. In particular, engineering of strongly clamped circular graphene membranes with a small distance to the cavity counter electrode allowed for the detection of high mechanical quality factors (10^5), comparatively large single-photon coupling, strong tunability of the static graphene equilibrium position, and for the demonstration of symmetry breaking in graphene mechanical resonators.

In chapter 7, we benchmarked multilayer graphene optomechanical systems by performing sideband cooling and force sensing experiments. We found that sideband cooling, with a minimum phonon occupation of 7.2, is limited by Joule heating of the graphene resonator at high microwave power, which is attributed to the finite resistance of graphene. Force sensing with a microwave pump on the red sideband revealed that the force sensitivity of coupled graphene-cavity devices has different limiting factors depending on the microwave pump power. The best force sensitivity, $390\,\mathrm{zN/Hz^{-1/2}}$ was achieved when balancing measurement imprecision, optomechanical damping, and heating. The obtained force sensitivity compares favorably with top-down nanoelectromechanical systems with the potential to be further improved.

In chapter 8, we studied the mechanical dissipation performing energy decay measurements in graphene. Energy decay measurements are immune from dephasing, which allowed for the detection of record high mechanical quality factors of $Q_\mathrm{m} \approx 10^6$, in the linear vibration regime. In the nonlinear regime, energy decay measurements revealed that energy is released discontinuously, that is, instead of a smooth exponential decay, sharp kinks were observed during the decay. These kinks indicate that certain dissipation

channels are suddenly switched off at some threshold energies. We attributed this phenomenon to nonlinear decay processes, as for instance, nonlinear mode-mode coupling of the fundamental mode to a higher order mode.

9.2 Outlook

The work presented in this thesis has substantially contributed to the understanding of the mechanical properties of graphene mechanical resonators. In particular, the implementation of energy decay measurements allowed for the investigation of mechanical dissipation with unprecedented accuracy. Our study lead to several interesting experimental results (linear temperature dependence of the dissipation at low temperatures potentially due to two-level fluctuators, motion-induced Joule dissipation, nonlinear mode-mode coupling) setting the basis for more involved experimental and theoretical investigations of the physics governing graphene mechanical resonators at low temperatures. For instance, covering the cavity counter electrode with a thin metal film would allow for the investigation of the influence of two-level fluctuators in the electrodes' oxide on the mechanical dissipation.

Regarding the optomechanical device performance, coupled graphene-cavity devices are promising for sensing applications. However, the finite graphene resistance poses limitations on the ability to sideband cool graphene membranes to the quantum ground state. Therefore, current device concepts and manipulation techniques have to be revised. One possible scenario relies on pulsed pumping schemes [196]. For this scheme to work, the rate for Joule heating of the mechanical resonator must be smaller than the rate associated to the optomechanical interaction. A second, and more promising, option consists of utilizing a mechanical heterostructure involving a monolayer superconductor such as $NbSe_2$ [197, 198]. Here, encapsulating $NbSe_2$ in between impermeable membranes is necessary since the monolayer superconductor is not stable in air. Possible devices may utilize the electrically insulating hexagonal boron nitride or graphene as the encapsulation material. In the latter, the superconducting proximity effect may lead to a very promising device realization, an all superconducting graphene-$NbSe_2$-graphene heterostructure.

In conclusion, the employed optomechanical readout and control of graphene NEMS in combination with energy decay measurements represents an extremely powerful tool to study motion at the ultimate two-dimensional limit. This is not restricted to graphene NEMS and can, in principle, be applied to any conducting 2D material.

Bibliography

[1] Richard Feynman. Plenty of Room at the Bottom, 1959.

[2] Gordon E Moore. Cramming more components onto integrated circuits, Reprinted from Electronics, volume 38, number 8, April 19, 1965, pp.114 ff. *Solid-State Circuits Newsletter, IEEE DOI - 10.1109/N-SSC.2006.4785860*, 20(3):33–35, 2006.

[3] Ioannis Tsioutsios. *Mechanical Resonators Based on Graphene and Carbon Nanotubes*. PhD thesis, Universitat de Autónoma de Barcelona, 2016.

[4] H. J. Mamin and D. Rugar. Sub-attonewton force detection at millikelvin temperatures. *Applied Physics Letters*, 79(20):3358–3360, 2001.

[5] D. Rugar, R. Budakian, H. J. Mamin, and B. W. Chui. Single spin detection by magnetic resonance force microscopy. *Nature*, 430(6997):329–332, 2004.

[6] M. S. Hanay, S. Kelber, A. K. Naik, D. Chi, S. Hentz, E. C. Bullard, E. Colinet, L. Duraffourg, and M. L. Roukes. Single-protein nanomechanical mass spectrometry in real time. *Nature Nanotechnology*, 7(9):602–8, 2012.

[7] A. D. O'Connell, M. Hofheinz, M. Ansmann, R. C. Bialczak, M. Lenander, E. Lucero, M. Neeley, D. Sank, H. Wang, M. Weides, J. Wenner, J. M. Martinis, and A. N. Cleland. Quantum ground state and single-phonon control of a mechanical resonator. *Nature*, 464(7289):697–703, 2010.

[8] M. Imboden and P. Mohanty. Dissipation in nanoelectromechanical systems. *Physics Reports*, 534(3):89–146, 2014.

[9] X. Li, W. Cai, J. An, S. Kim, J. Nah, D. Yang, R. Piner, A. Velamakanni, I. Jung, E. Tutuc, S. K. Banerjee, L. Colombo, and R. S. Ruoff. Large-area synthesis of high-quality and uniform graphene films on copper foils. *Science*, 324(5932):1312–4, 2009.

[10] K. Jensen, K. Kim, and A. Zettl. An atomic-resolution nanomechanical mass sensor. *Nature Nanotechnology*, 3(9):533–537, 2008.

[11] A. K. Geim and K. S. Novoselov. The rise of graphene. *Nature materials*, 6(3):183–191, 2007.

[12] Y. Wu, Y. M. Lin, A. A. Bol, K. A. Jenkins, F. Xia, D. B. Farmer, Y. Zhu, and P. Avouris. High-frequency, scaled graphene transistors on diamond-like carbon. *Nature*, 472(7341):74–78, 2011.

[13] L. Wang, I. Meric, P. Y. Huang, Q. Gao, Y. Gao, H. Tran, T. Taniguchi, K. Watanabe, L. M. Campos, D. A. Muller, J. Guo, P. Kim, J. Hone, K. L. Shepard, and C. R. Dean. One-Dimensional Electrical Contact to a Two-Dimensional Material. *Science*, 342(6158):614–617, 2013.

[14] R. R. Nair, P. Blake, A. N. Grigorenko, K. S. Novoselov, T. J. Booth, T. Stauber, N. M. R. Peres, and A. K. Geim. Fine structure constant defines visual transparency of graphene. *Science*, 320(5881):1308, 2008.

[15] Y. Zhu, Z. Sun, Z. Yan, Z. Jin, and J. M. Tour. Rational Design of Hybrid Graphene Films for High-Performance Transparent Electrodes. *ACS Nano*, 5(8):6472 – 6479, 2011.

[16] G. Konstantatos, M. Badioli, L. Gaudreau, J. Osmond, M. Bernechea, F. P. Garcia de Arquer, F. Gatti, and F. H. L. Koppens. Hybrid graphenequantum dot phototransistors with ultrahigh gain. *Nature Nanotechnology*, 7(6):363–368, 2012.

[17] M. Massicotte, P. Schmidt, F. Vialla, K. G. Schädler, A. Reserbat-Plantey, K. Watanabe, T. Taniguchi, K. J. Tielrooij, and F. H. L. Koppens. Picosecond photoresponse in van der Waals heterostructures. *Nature Nanotechnology*, 11(1):42–46, 2015.

[18] C. Lee, X. Wei, J. W. Kysar, and J. Hone. Measurement of the elastic properties and intrinsic strength of monolayer graphene. *Science*, 321(5887):385–388, 2008.

[19] J. Chaste, A. Eichler, J. Moser, G. Ceballos, R. Rurali, and A. Bachtold. A nanomechanical mass sensor with yoctogram resolution. *Nature Nanotechnology*, 7(5):301–304, 2012.

[20] J. Moser, J. Güttinger, A. Eichler, M. J. Esplandiu, D. E. Liu, M. I. Dykman, and A. Bachtold. Ultrasensitive force detection with a nanotube mechanical resonator. *Nature Nanotechnology*, 8:493–496, 2013.

[21] Y. M. Lin and P. Avouris. Strong Suppression of Electrical Noise in Bilayer Graphene Nanodevices. *Nano Letters*, 8(8):2119–2125, 2008.

[22] A. Eichler, J. Moser, J. Chaste, M. Zdrojek, I. Wilson-Rae, and A. Bachtold. Nonlinear damping in mechanical resonators made from carbon nanotubes and graphene. *Nature Nanotechnology*, 6(6):339–342, 2011.

[23] X. Song, M. Oksanen, M. A. Sillanpää, H. G. Craighead, J. M. Parpia, and P. J. Hakonen. Stamp Transferred Suspended Graphene Mechanical Resonators for Radio Frequency Electrical Readout. *Nano Letters*, 12(1):198–202, 2011.

[24] C. Chen, S. Rosenblatt, K. I. Bolotin, W. Kalb, P. Kim, I. Kymissis, H. L. Stormer, T. F. Heinz, and J. Hone. Performance of monolayer graphene nanomechanical resonators with electrical readout. *Nature Nanotechnology*, 4(12):861–867, 2009.

[25] A. M. van ver Zande, R. A. Barton, J. S. Alden, C. S. Ruiz-Vargas, W. S. Whitney, P. H. Q. Pham, J. Park, J. M. Parpia, H. G. Craighead, and P. L. McEuen. Large-Scale Arrays of Single-Layer Graphene Resonators. *Nano letters*, 10(12):4869–4873, 2010.

[26] Y. Xu, C. Chen, V. V. Deshpande, F. A. DiRenno, A. Gondarenko, D. B. Heinz, S. Liu, P. Kim, and J. Hone. Radio frequency electrical transduction of graphene mechanical resonators. *Applied Physics Letters*, 97(24):243111, 2010.

[27] J. S. Bunch, A. M. van der Zande, S. S. Verbridge, I. W. Frank, D. M. Tanenbaum, J. M. Parpia, H. G. Craighead, and P. L. McEuen. Electromechanical resonators from graphene sheets. *Science*, 315(5811):490–493, 2007.

[28] R. A. Barton, I. R. Storch, V. P. Adiga, R. Sakakibara, B. R. Cipriany, B. Ilic, S. P. Wang, P. Ong, P. L. McEuen, J. M. Parpia, and H. G. Craighead. Photothermal Self-Oscillation and Laser Cooling of Graphene Optomechanical Systems. *Nano Letters*, 12(9):4681–4686, 2012.

[29] C. Chen and J. Hone. Graphene nanoelectromechanical systems. *Proceedings of the IEEE*, 101(7):1766–1779, 2013.

[30] J. Moser, A. Eichler, J. Güttinger, M. Dykman, and A. Bachtold. Nanotube mechanical resonators with quality factors of up to 5 million. *Nature Nanotechnology*, 9(12):1007–1011, 2014.

[31] O. Arcizet, P. F. Cohadon, T. Briant, M. Pinard, and A. Heidmann. Radiation-pressure cooling and optomechanical instability of a micromirror. *Nature*, 444(7115):71–74, 2006.

[32] S. Gröblacher, J. B. Hertzberg, M. R. Vanner, G. D. Cole, S. Gigan, K. C. Schwab, and M. Aspelmeyer. Demonstration of an ultracold micro-optomechanical oscillator in a cryogenic cavity. *Nature Physics*, 5(7):485–488, 2009.

[33] K. Brown, J. Britton, R. Epstein, J. Chiaverini, D. Leibfried, and D. Wineland. Passive Cooling of a Micromechanical Oscillator with a Resonant Electric Circuit. *Physical Review Letters*, 99(13):137205, 2007.

[34] C. A. Regal, J. D. Teufel, and K. W. Lehnert. Measuring nanomechanical motion with a microwave cavity interferometer. *Nature Physics*, 4(7):555–560, 2008.

[35] J. B. Hertzberg, T. Rocheleau, T. Ndukum, M. Savva, A. A. Clerk, and K. C. Schwab. Back-action-evading measurements of nanomechanical motion. *Nature Physics*, 6(3):213–217, 2009.

[36] T. Rocheleau, T. Ndukum, C. Macklin, J. B. Hertzberg, A. A. Clerk, and K. C. Schwab. Preparation and detection of a mechanical resonator near the ground state of motion. *Nature*, 463(7277):72–75, 2010.

[37] F. Massel, T. T. Heikkilä, J. M. Pirkkalainen, S. U. Cho, H. Saloniemi, P. J. Hakonen, and M. A. Sillanpää. Microwave amplification with nanomechanical resonators. *Nature*, 480(7377):351–354, 2011.

[38] J. D. Teufel, T. Donner, D. Li, J. W. Harlow, M. S. Allman, K. Cicak, A. J. Sirois, J. D. Whittaker, K. W. Lehnert, and R. W. Simmonds. Sideband cooling of micromechanical motion to the quantum ground state. *Nature*, 475(7356):359–63, 2011.

[39] X. Zhou, F. Hocke, A. Schliesser, A. Marx, H. G. Huebl, R. Gross, and T. J. Kippenberg. Slowing, advancing and switching of microwave signals using circuit nanoelectromechanics. *Nature Physics*, 9:179–184, 2013.

[40] E. Verhagen, S. Deléglise, S. Weis, A. Schliesser, and T. J. Kippenberg. Quantum-coherent coupling of a mechanical oscillator to an optical cavity mode. *Nature*, 482(7383):63–7, 2012.

[41] J. Chan, T. P. Mayer Alegre, A. H. Safavi-Naeini, J. T Hill, A. Krause, S. Gröblacher, M. Aspelmeyer, and O. Painter. Laser cooling of a nanomechanical oscillator into its quantum ground state. *Nature*, 478(7367):89–92, 2011.

[42] J. D. Thompson, B. M. Zwickl, A. M. Jayich, F. Marquardt, S. M. Girvin, and J. G. E. Harris. Strong dispersive coupling of a high-finesse cavity to a micromechanical membrane. *Nature*, 452(7183):72–75, 2008.

[43] J. Gieseler, B. Deutsch, R. Quidant, and L. Novotny. Subkelvin Parametric Feedback Cooling of a Laser-Trapped Nanoparticle. *Physical Review Letters*, 109(10):103603, sep 2012.

[44] K. W. Murch, K. L. Moore, S. Gupta, and D. M. Stamper-Kurn. Observation of quantum-measurement backaction with an ultracold atomic gas. *Nature Physics*, 4(7):561–564, 2008.

[45] M. Aspelmeyer, T. J. Kippenberg, and F. Marquardt. Cavity optomechanics. *Review Modern Physics*, 86(4):1391–1452, 2014.

[46] J. D. Teufel, T. Donner, M. A. Castellanos-Beltran, J. W. Harlow, and K. W. Lehnert. Nanomechanical motion measured with an imprecision below that at the standard quantum limit. *Nature Nanotechnology*, 4(12):820–823, 2009.

[47] G. Anetsberger, E. Gavartin, O. Arcizet, Q. P. Unterreithmeier, E. M. Weig, M. L. Gorodetsky, J. P. Kotthaus, and T. J. Kippenberg. Measuring nanomechanical motion with an imprecision below the standard quantum limit. *Physical Review A*, 82(6):61804, 2010.

[48] T. P. Purdy, R. W. Peterson, and C. A. Regal. Observation of Radiation Pressure Shot Noise on a Macroscopic Object. *Science*, 339(6121):801–804, 2013.

[49] E. E. Wollman, C. U. Lei, A. J. Weinstein, J. Suh, A. Kronwald, F. Marquardt, A. A. Clerk, and K. C. Schwab. Quantum squeezing of motion in a mechanical resonator. *Science*, 349(6251):952–955, 2015.

[50] B. P. Abbott et al. (LIGO Scientific Collaboration Collaboration) and Virgo. Observation of Gravitational Waves from a Binary Black Hole Merger. *Physical Review Letters*, 116(6):061102, 2016.

[51] J. M. Pirkkalainen, E. Damskägg, M. Brandt, F. Massel, and M. A. Sillanpää. Squeezing of Quantum Noise of Motion in a Micromechanical Resonator. *Physical Review Letters*, 115(24):243601, 2015.

[52] F. Lecocq, J. B. Clark, R. W. Simmonds, J. Aumentado, and J. D. Teufel. Quantum Nondemolition Measurement of a Nonclassical State of a Massive Object. *Physical Review X*, 5(4):041037, dec 2015.

[53] T. A. Palomaki, J. W. Harlow, J. D. Teufel, R. W. Simmonds, and K. W. Lehnert. Coherent state transfer between itinerant microwave fields and a mechanical oscillator. *Nature*, 495(7440):210–214, 2013.

[54] T. A. Palomaki, J. D. Teufel, R. W. Simmonds, and K. W. Lehnert. Entangling Mechanical Motion with Microwave Fields. *Science*, 342(6159):710–713, 2013.

[55] R. Riedinger, S. Hong, R. A. Norte, J. A. Slater, J. Shang, A. G. Krause, V. Anant, M. Aspelmeyer, and S. Gröblacher. Non-classical correlations between single photons and phonons from a mechanical oscillator. *Nature*, 530(7590):313–316, 2016.

[56] T. Bagci, A. Simonsen, S. Schmid, L. G. Villanueva, E. Zeuthen, J. Appel, J. M. Taylor, A. Sørensen, K. Usami, A. Schliesser, and E. S. Polzik. Optical detection of radio waves through a nanomechanical transducer. *Nature*, 507(7490):81–85, 2014.

[57] R. W. Andrews, R. W. Peterson, T. P. Purdy, K. Cicak, R. W. Simmonds, C. A. Regal, and K. W. Lehnert. Bidirectional and efficient conversion between microwave and optical light. *Nature Physics*, 10:321–326, 2014.

[58] L. D. Landau. Zur Theorie der phasenumwandlungen II. *Phys. Z. Sowjetunion*, 11:26 – 35, 1937.

[59] K. S. Novoselov, A. K. Geim, S. V. Morozov, D. Jiang, Y. Zhang, S. V. Dubonos, I. V. Grigorieva, and A. A. Firsov. Electric field effect in atomically thin carbon films. *Science*, 306(5696):666–669, 2004.

[60] P. R. Wallace. The Band Theory of Graphite. *Physical Review*, 71(9):622, 1947.

[61] R. Saito, G. Dresselhaus, and M. Dresselahus. *Physical Properties of Carbon Nanotubes*. Imperial College Press (London), 1998.

[62] J. Dauber. Transport in Graphene Nanoribbons. *Diploma Thesis*, 2011.

[63] R. Waser. *Nanoelectronics and Information Technology*. Wiley-VCH, 2005.

[64] L. Banszerus, M. Schmitz, S. Engels, M. Goldsche, K. Watanabe, T. Taniguchi, B. Beschoten, and C. Stampfer. Ballistic Transport Exceeding 28 μm in CVD Grown Graphene. *Nano Letters*, 16(2):1387–1391, 2016.

[65] B. Partoens and F. M. Peeters. From graphene to graphite: Electronic structure around the K point. *Physical Review BB*, 74(7):75404, 2006.

[66] J. S. Bunch, S. S. Verbridge, J. S. Alden, A. M. van der Zande, J. M. Parpia, H. G. Craighead, and P. L. McEuen. Impermeable Atomic Membranes from Graphene Sheets. *Nano Letters*, 8(8):2458–2462, 2008.

[67] W. Bao, K. Myhro, Z. Zhao, Z. Chen, W. Jang, L. Jing, F. Miao, H. Zhang, C. Dames, and C. N. Lau. In situ observation of electrostatic and thermal manipulation of suspended graphene membranes. *Nano Letters*, 12(11):5470–5474, 2012.

[68] R. A. Barton, B. Ilic, A. M. van der Zande, W. S. Whitney, P. L. McEuen, J. M. Parpia, and H. G. Craighead. High, Size-Dependent Quality Factor in an Array of Graphene Mechanical Resonators. *Nano Letters*, 11(3):1232–1236, 2011.

[69] A. M. van der Zande. *The Structure and Mechanics of Atomically-Thin Graphene Membranes*. PhD thesis, Cornell University, 2011.

[70] M. Poot and H. S. J. van der Zant. Nanomechanical properties of few-layer graphene membranes. *Applied Physics Letters*, 92(6):063111, 2008.

[71] V. Singh, S. Sengupta, H. S. Solanki, R. Dhall, A. Allain, S. Dhara, P. Pant, and M. M. Deshmukh. Probing thermal expansion of graphene and modal dispersion at low-temperature using graphene nanoelectromechanical systems resonators. *Nanotechnology*, 21(16):165204, 2010.

[72] X. L. Feng, C. J. White, A. Hajimiri, and M. L. Roukes. A self-sustaining ultrahigh-frequency nanoelectromechanical oscillator. *Nature Nanotechnology*, 3(6):342–346, 2008.

[73] L. G. Villanueva, R. B. Karabalin, M. H. Matheny, E. Kenig, M. C. Cross, and M. L. Roukes. A nanoscale parametric feedback oscillator. *Nano Letters*, 11(11):5054–9, 2011.

[74] A. Eichler, J. Chaste, J. Moser, and A. Bachtold. Parametric amplification and self-oscillation in a nanotube mechanical resonator. *Nano Letters*, 11(7):2699–2703, 2011.

[75] C. Chen, S. Lee, V. Deshpande, G. H. Lee, M. Lekas, K. Shepard, and J. Hone. Graphene mechanical oscillators with tunable frequency. *Nature Nanotechnology*, 8(12):923–927, 2013.

[76] H. B. Callen and T. A. Welton. Irreversibility and Generalized Noise. *Physical Review*, 83(1):34–40, 1951.

[77] L.D. Landau and E.M. Lifschitz. *Statistical Physics, Part 1, Vol. 34*. 1981.

[78] R. Lifshitz and M. C. Cross. Nonlinear dynamics of nanomechanical and micromechanical resonators. *Reviews of nonlinear dynamics and complexity*, 1:1–48, 2008.

[79] M. Imboden, O. Williams, and P. Mohanty. Nonlinear dissipation in diamond nanoelectromechanical resonators. *Applied Physics Letters*, 102(10):103502, 2013.

[80] S. Zaitsev, O. Shtempluck, E. Buks, and O. Gottlieb. Nonlinear damping in a micromechanical oscillator. *Nonlinear Dynamics*, 67(1):859–883, 2012.

[81] L. D. Landau, E. M. Lifshitz, J. B. Sykes, W. H. Reid, and E. H. Dill. *Theory of elasticity: Vol. 7 of course of theoretical physics*. Pergamon Press, 2 edition, 1970.

[82] R. Al-Jishi and G. Dresselhaus. Lattice-dynamical model for graphite. *Physical Review B*, 26(8):4514–4522, 1982.

[83] S. Timoshenko. *Vibration problems in engineering*. WILEY-VCH Verlag, 1974.

[84] F. Marquardt, J. P. Chen, A. A. Clerk, and S. M. Girvin. Quantum Theory of Cavity-Assisted Sideband Cooling of Mechanical Motion. *Physical Review Letters*, 99(9):93902, 2007.

[85] I Wilson-Rae, N Nooshi, W Zwerger, and T J Kippenberg. Theory of Ground State Cooling of a Mechanical Oscillator Using Dynamical Backaction. *Physical Review Letters*, 99(9):93901, 2007.

[86] P. K. Day, H. G. LeDuc, B. A. Mazin, A. Vayonakis, and J. Zmuidzinas. A broadband superconducting detector suitable for use in large arrays. *Nature*, 425(6960):817–821, 2003.

[87] P. Goy, J. M. Raimond, M. Gross, and S. Haroche. Observation of Cavity-Enhanced Single-Atom Spontaneous Emission. *Physical Review Letters*, 50(24):1903–1906, 1983.

[88] A. Wallraff, D. I. Schuster, A. Blais, L. Frunzio, R. S. Huang, J. Majer, S. Kumar, S. M. Girvin, and R. J. Schoelkopf. Strong coupling of a single photon to a superconducting qubit using circuit quantum electrodynamics. *Nature*, 431(7005):162–167, 2004.

[89] R. J. Schoelkopf and S. M. Girvin. Wiring up quantum systems. *Nature*, 451(7179):664–9, 2008.

[90] J. Clarke and F. K. Wilhelm. Superconducting quantum bits. *Nature*, 453(7198):1031–1042, 2008.

[91] M. R. Delbecq, V. Schmitt, F. D. Parmentier, N. Roch, J. J. Viennot, G. Fève, B. Huard, C. Mora, A. Cottet, and T. Kontos. Coupling a Quantum Dot, Fermionic Leads, and a Microwave Cavity on a Chip. *Physical Review Letters*, 107(25):256804, 2011.

[92] T. Frey, P. J. Leek, M. Beck, A. Blais, T. Ihn, K. Ensslin, and A. Wallraff. Dipole Coupling of a Double Quantum Dot to a Microwave Resonator. *Physical Review Letters*, 108(4):46807, 2012.

[93] D. I. Schuster, A. P. Sears, E. Ginossar, L. DiCarlo, L. Frunzio, J. J. L. Morton, H. Wu, G. A. D. Briggs, B. B. Buckley, D. D. Awschalom, and R. J. Schoelkopf. High-Cooperativity Coupling of Electron-Spin Ensembles to Superconducting Cavities. *Physical Review Letters*, 105(14):140501, 2010.

[94] J. D. Teufel, J. W. Harlow, C. A. Regal, and K. W. Lehnert. Dynamical Backaction of Microwave Fields on a Nanomechanical Oscillator. *Physical Review Letters*, 101(19):197203, 2008.

[95] R. E. Collin. *Foundations for Microwave Engineering.* Wiley-IEEE Press, 1992.

[96] D. M. Pozar. *Microwave Engineering.* Wiley, 2012.

[97] J. B. Hertzberg. *Back-action evading measurements of nanomechanical motion approaching quantum limits.* PhD thesis, Univ. of Maryland, College Park, 2009.

[98] Xi. Zhou. *Superconducting cavity nanoelectromechanics*. Phd thesis, École Polytechnique Fédérale de Lausanne, 2013.

[99] F. Marquardt, A. A. Clerk, and S. M. Girvin. Quantum theory of optomechanical cooling. *Journal of Modern Optics*, 55(19-20):3329–3338, 2008.

[100] C. K. Law. Interaction between a moving mirror and radiation pressure: A Hamiltonian formulation. *Physical Review A*, 51(3):2537–2541, 1995.

[101] T. Bagci, A. Simonsen, S. Schmid, L. G. Villanueva, E. Zeuthen, J. Appel, J. M. Taylor, A. Sørensen, K. Usami, and A. Schliesser. Optical detection of radio waves through a nanomechanical transducer. *Nature*, 507:81–85, 2013.

[102] C. Eichler, D. Bozyigit, C Lang, M Baur, L Steffen, J M Fink, S Filipp, and A Wallraff. Observation of Two-Mode Squeezing in the Microwave Frequency Domain. *Physical Review Letters*, 107(11):113601, 2011.

[103] E. Flurin, N. Roch, F. Mallet, M. H. Devoret, and B. Huard. Generating Entangled Microwave Radiation Over Two Transmission Lines. *Physical Review Letters*, 109(18):183901, 2012.

[104] R. W. Peterson, T. P. Purdy, N. S. Kampel, R. W. Andrews, P.-L. Yu, K. W. Lehnert, and C. A. Regal. Laser Cooling of a Micromechanical Membrane to the Quantum Backaction Limit. *Physical Review Letters*, 116(6):063601, 2016.

[105] M. A. Castellanos-Beltran and K. W. Lehnert. Widely tunable parametric amplifier based on a superconducting quantum interference device array resonator. *Applied Physics Letters*, 91(8):083509, 2007.

[106] N. Bergeal, F. Schackert, M. Metcalfe, R. Vijay, V. E. Manucharyan, L. Frunzio, D. E. Prober, R. J. Schoelkopf, S. M. Girvin, and M. H. Devoret. Phase-preserving amplification near the quantum limit with a Josephson ring modulator. *Nature*, 465(7294):64–68, 2010.

[107] M. A. Castellanos-Beltran, K. D. Irwin, G. C. Hilton, L. R. Vale, and K. W. Lehnert. Amplification and squeezing of quantum noise with a tunable Josephson metamaterial. *Nature Physics*, 4(12):929–931, 2008.

[108] J. D. Teufel, D. Li, M. S. Allman, K. Cicak, A. J. Sirois, J. D. Whittaker, and R. W. Simmonds. Circuit cavity electromechanics in the strong-coupling regime. *Nature*, 471(7337):204–208, 2011.

[109] Z. Wang and P. X. L. Feng. Dynamic range of atomically thin vibrating nanomechanical resonators. *Applied Physics Letters*, 104(10):103109, 2014.

[110] M. Göppl. *Engineering Quantum Electronic Chips - Realization and Characterization of Circuit Quantum Electrodynamics Systems*. Phd thesis, ETH Zurich, 2009.

[111] J. M. Fink. *Quantum Nonlinearities in Strong Coupling Circuit QED*. Phd thesis, ETH Zurich, 2010.

[112] M. Göppl, A. Fragner, M. Baur, R. Bianchetti, S. Filipp, J. M. Fink, P. J. Leek, G. Puebla, L. Steffen, and A. Wallraff. Coplanar waveguide resonators for circuit quantum electrodynamics. *Journal of Applied Physics*, 104(11):113904, 2008.

[113] C. R. Dean, A. F. Young, I. Meric, C. Lee, L. Wang, S. Sorgenfrei, K. Watanabe, T. Taniguchi, P. Kim, K. L. Shepard, and J. Hone. Boron nitride substrates for high-quality graphene electronics. *Nature Nanotechnology*, 5(10):722–726, 2010.

[114] P. Blake, E. W. Hill, A. H. Castro Neto, K. S. Novoselov, D. Jiang, R. Yang, T. J. Booth, and A. K. Geim. Making graphene visible. *Applied Physics Letters*, 91(6):063124, 2007.

[115] Z. H. Ni, H. M. Wang, J. Kasim, H. M. Fan, T. Yu, Y. H. Wu, Y. P. Feng, and Z. X. Shen. Graphene Thickness Determination Using Reflection and Contrast Spectroscopy. *Nano Letters*, 7(9):2758–2763, 2007.

[116] S. Cartamil. *Graphene Resonators with High Quality Factor Using a Substrate Independent Transfer Technique*. Master thesis, Universidad Autónoma de Barcelona, 2012.

[117] S. Lee, C. Chen, V. V. Deshpande, G. H. Lee, I. Lee, M. Lekas, A. Gondarenko, Y. J. Yu, K. Shepard, P. Kim, and J. Hone. Electrically integrated SU-8 clamped graphene drum resonators for strain engineering. *Applied Physics Letters*, 102(15):153101, 2013.

[118] A. Reserbat-Plantey, K. G. Schädler, L. Gaudreau, G. Navickaite, J. Güttinger, D. E. Chang, C. Toninelli, A. Bachtold, and F. H. L. Koppens. Electromechanical control of nitrogen-vacancy defect emission using graphene NEMS. *Nature Communications*, 7:10218, jan 2016.

[119] H.Y. Chiu, P. Hung, H. W. C. Postma, and M. Bockrath. Atomic-Scale Mass Sensing Using Carbon Nanotube Resonators. *Nano Letters*, 8(12):4342–4346, 2008.

[120] S. Stapfner, L. Ost, D. Hunger, J. Reichel, I. Favero, and E. M. Weig. Cavity-enhanced optical detection of carbon nanotube Brownian motion. *Applied Physics Letters*, 102(15):151910, 2013.

[121] A. Ayari, P. Vincent, S. Perisanu, M. Choueib, V. Gouttenoire, M. Bechelany, D. Cornu, and S. T. Purcell. Self-Oscillations in Field Emission Nanowire Mechanical Resonators: A Nanometric dc-ac Conversion. *Nano Letters*, 7(8):2252–2257, 2007.

[122] M. Poot and H. S. J. van der Zant. Mechanical systems in the quantum regime. *Physics Reports*, 511(5):273–335, 2012.

[123] D. E. Chang, C. A. Regal, S. B. Papp, D. J. Wilson, J. Ye, O. Painter, H. J. Kimble, and P. Zoller. Cavity opto-mechanics using an optically levitated nanosphere. *Proceedings of the National Academy of Sciences*, 107(3):1005–1010, 2010.

[124] N. Kiesel, F. Blaser, U. Delić, D. Grass, R. Kaltenbaek, and M. Aspelmeyer. Cavity cooling of an optically levitated submicron particle. *Proceedings of the National Academy of Sciences*, 110(35):14180–14185, 2013.

[125] J. Gieseler, L. Novotny, and R. Quidant. Thermal nonlinearities in a nanomechanical oscillator. *Nature Physics*, 9:806–810, 2013.

[126] K. K. Ni, R. Norte, D. J. Wilson, J. D. Hood, D. E. Chang, O. Painter, and H. J. Kimble. Enhancement of Mechanical Q-Factors by Optical Trapping. *Physical Review Letters*, 108(21):214302, 2012.

[127] A. G. Kuhn, M. Bahriz, O. Ducloux, C. Chartier, O. Le Traon, T. Briant, P. F. Cohadon, A. Heidmann, C. Michel, L. Pinard, and R. Flaminio. A micropillar for cavity optomechanics. *Applied Physics Letters*, 99(12):121103, 2011.

[128] L. Ding, C. Baker, P. Senellart, A. Lemaitre, S. Ducci, G. Leo, and I. Favero. High Frequency GaAs Nano-Optomechanical Disk Resonator. *Physical Review Letters*, 105(26):263903, 2010.

[129] I. Yeo, P. L. de Assis, A. Gloppe, E. Dupont-Ferrier, P. Verlot, N. S. Malik, E. Dupuy, J. Claudon, J. M. Gérard, A. Auffèves, G. Nogues, S. Seidelin, J. P. Poizat, O. Arcizet, and M. Richard. Strain-mediated coupling in a quantum dot-mechanical oscillator hybrid system. *Nature Nanotechnology*, 9:106–110, 2013.

[130] K. D. Petersson, L. W. McFaul, M. D. Schroer, M. Jung, J. M. Taylor, A. A. Houck, and J. R. Petta. Circuit quantum electrodynamics with a spin qubit. *Nature*, 490(7420):380–383, 2012.

[131] A. M. Eriksson, D. Midtvedt, A. Croy, and A. Isacsson. Frequency tuning, nonlinearities and mode coupling in circular mechanical graphene resonators. *Nanotechnology*, 24(39):395702, 2013.

[132] D. Garcia-Sanchez, A. M. van der Zande, A. San Paulo, B. Lassagne, P. L. McEuen, and A. Bachtold. Imaging Mechanical Vibrations in Suspended Graphene Sheets. *Nano Letters*, 8(5):1399–1403, 2008.

[133] I. Kozinsky, H. W. Ch. Postma, I. Bargatin, and M. L. Roukes. Tuning nonlinearity, dynamic range, and frequency of nanomechanical resonators. *Applied Physics Letters*, 88(25):253101, 2006.

[134] M. A. Sillanpää, R. Khan, T. T. Heikkilä, and P. J. Hakonen. Macroscopic quantum tunneling in nanoelectromechanical systems. *Physical Review B*, 84(19):195433, 2011.

[135] M. I. Younis and A. H. Nayfeh. A Study of the Nonlinear Response of a Resonant Microbeam to an Electric Actuation. *Nonlinear Dynamics*, 31(1):91–117, 2003.

[136] A. Eichler, J. Moser, M. I. Dykman, and A. Bachtold. Symmetry breaking in a mechanical resonator made from a carbon nanotube. *Nature Communications*, 4:2843, 2013.

[137] A. H. Nayfeh and D. T. Mook. *Nonlinear oscillations*. John Wiley & Sons, 2008.

[138] A. Eichler, M. del Álamo Ruiz, J. A. Plaza, and A. Bachtold. Strong Coupling between Mechanical Modes in a Nanotube Resonator. *Physical Review Letters*, 109(2):25503, 2012.

[139] T. T. Heikkilä, F. Massel, J. Tuorila, R. Khan, and M. A. Sillanpää. Enhancing Optomechanical Coupling via the Josephson Effect. *Physical Review Letters*, 112(20):203603, 2014.

[140] A. J. Rimberg, M. P. Blencowe, A. D. Armour, and P. D. Nation. A cavity-Cooper pair transistor scheme for investigating quantum optomechanics in the ultra-strong coupling regime. *New Journal of Physics*, 16(5):055008, 2014.

[141] A. Voje, J. M. Kinaret, and A. Isacsson. Generating macroscopic superposition states in nanomechanical graphene resonators. *Physical Review B*, 85(20):205415, 2012.

[142] S. Rips and M. J. Hartmann. Quantum Information Processing with Nanomechanical Qubits. *Physical Review Letters*, 110(12):120503, 2013.

[143] S. Rips, I. Wilson-Rae, and M. J. Hartmann. Nonlinear nanomechanical resonators for quantum optoelectromechanics. *Physical Review A*, 89(1):13854, 2014.

[144] X. Y. Lü, J. Q. Liao, L. Tian, and F. Nori. Steady-state mechanical squeezing in an optomechanical system via Duffing nonlinearity. *Physical Review A*, 91(1):013834, 2015.

[145] V. Sazonova, Y. Yaish, H. Üstünel, D. Roundy, T. A. Arias, and P. L. McEuen. A tunable carbon nanotube electromechanical oscillator. *Nature*, 431(7006):284–287, 2004.

[146] B. Lassagne, Y. Tarakanov, J. Kinaret, D. Garcia-Sanchez, and A. Bachtold. Coupling Mechanics to Charge Transport in Carbon Nanotube Mechanical Resonators. *Science*, 325(5944):1107–1110, 2009.

[147] G. A. Steele, A. K. Hüttel, B. Witkamp, M. Poot, H. B. Meerwaldt, L. P. Kouwenhoven, and H. S. J. van der Zant. Strong Coupling Between Single-Electron Tunneling and Nanomechanical Motion. *Science*, 325(5944):1103–1107, 2009.

[148] V. Gouttenoire, T. Barois, S. Perisanu, J. L. Leclercq, S. T. Purcell, P. Vincent, and A. Ayari. Digital and FM Demodulation of a Doubly Clamped Single-Walled Carbon-Nanotube Oscillator: Towards a Nanotube Cell Phone. *Small*, 6(9):1060–1065, 2010.

[149] M. Ganzhorn, S. Klyatskaya, M. Ruben, and W. Wernsdorfer. Strong spin-phonon coupling between a single-molecule magnet and a carbon nanotube nanoelectromechanical system. *Nature Nanotechnology*, 8(3):165–169, 2013.

[150] A. Benyamini, A. Hamo, S. V. Kusminskiy, F. von Oppen, and S. Ilani. Real-space tailoring of the electron-phonon coupling in ultraclean nanotube mechanical resonators. *Nature Physics*, 10(2):151–156, 2014.

[151] P. Häkkinen, A. Isacsson, A. Savin, J. Sulkko, and P. Hakonen. Charge Sensitivity Enhancement via Mechanical Oscillation in Suspended Carbon Nanotube Devices. *Nano Letters*, 15(3):1667–1672, 2015.

[152] E. Gil-Santos, D. Ramos, J. Martinez, M. Fernandez-Regulez, R. Garcia, A. San Paulo, M. Calleja, and J. Tamayo. Nanomechanical mass sensing and stiffness spectrometry based on two-dimensional vibrations of resonant nanowires. *Nature Nanotechnology*, 5(9):641–645, 2010.

[153] O. Arcizet, V. Jacques, A. Siria, P. Poncharal, P. Vincent, and S. Seidelin. A single nitrogen-vacancy defect coupled to a nanomechanical oscillator. *Nature Physics*, 7(11):879–883, 2011.

[154] J. M. Nichol, E. R. Hemesath, L. J. Lauhon, and R. Budakian. Nanomechanical detection of nuclear magnetic resonance using a silicon nanowire oscillator. *Physical Review B*, 85(5):54414, 2012.

[155] J. M. Nichol, T. R. Naibert, E. R. Hemesath, L. J. Lauhon, and R. Budakian. Nanoscale Fourier-Transform Magnetic Resonance Imaging. *Physical Review X*, 3(3):31016, 2013.

[156] M. Sansa, M. Fernández-Regúlez, J. Llobet, Á. San Paulo, and F. Pérez-Murano. High-sensitivity linear piezoresistive transduction for nanomechanical beam resonators. *Nature Communications*, 5:4313, 2014.

[157] A. Gloppe, P. Verlot, E. Dupont-Ferrier, A. Siria, P. Poncharal, G. Bachelier, P. Vincent, and O. Arcizet. Bidimensional nano-optomechanics and topological backaction in a non-conservative radiation force field. *Nature Nanotechnology*, 9(11):920–926, 2014.

[158] M. Montinaro, G. Wüst, M. Munsch, Y. Fontana, E. Russo-Averchi, M. Heiss, A. Fontcuberta i Morral, R. J. Warburton, and M. Poggio. Quantum Dot Opto-Mechanics in a Fully Self-Assembled Nanowire. *Nano Letters*, 14(8):4454–4460, 2014.

[159] J. P. Mathew, R. Patel, A. Borah, C. B. Maliakkal, T. S. Abhilash, and M. M. Deshmukh. Nanoscale Electromechanics To Measure Thermal Conductivity, Expansion, and Interfacial Losses. *Nano Letters*, 15(11):7621–7626, 2015.

[160] A. Nigues, A. Siria, and P. Verlot. Dynamical backaction cooling with free electrons. *Nature Communications*, 6:8104, 2015.

[161] T. Miao, S. Yeom, P. Wang, B. Standley, and M. Bockrath. Graphene Nanoelectromechanical Systems as Stochastic-Frequency Oscillators. *Nano Letters*, 14(6):2982–2987, 2014.

[162] V. Singh, S. J. Bosman, B. H. Schneider, Y. M. Blanter, A. Castellanos-Gomez, and G. A. Steele. Optomechanical coupling between a multilayer graphene mechanical resonator and a superconducting microwave cavity. *Nature Nanotechnology*, 9(10):820–824, 2014.

[163] X. Song, M. Oksanen, J. Li, P. J. Hakonen, and M. A. Sillanpää. Graphene Optomechanics Realized at Microwave Frequencies. *Physical Review Letters*, 113(2):27404, 2014.

[164] P. Weber, J. Güttinger, I. Tsioutsios, D. E. Chang, and A. Bachtold. Coupling Graphene Mechanical Resonators to Superconducting Microwave Cavities. *Nano Letters*, 14(5):2854–2860, 2014.

[165] R. van Leeuwen, A. Castellanos-Gomez, G. A. Steele, H. S. J. van der Zant, and W. J. Venstra. Time-domain response of atomically thin MoS2 nanomechanical resonators. *Applied Physics Letters*, 105(4):041911, 2014.

[166] A. C. Bleszynski-Jayich, W. E. Shanks, B. Peaudecerf, E. Ginossar, F. von Oppen, L. Glazman, and J. G. E. Harris. Persistent Currents in Normal Metal Rings. *Science*, 326(5950):272–275, 2009.

[167] C. Chen, V. V. Deshpande, M. Koshino, S. Lee, A. Gondarenko, A. H. MacDonald, P. Kim, and J. Hone. Modulation of mechanical resonance by chemical potential oscillation in graphene. *Nature Physics*, 12:240–244, 2016.

[168] X. Wang and H. Dai. Etching and narrowing of graphene from the edges. *Nature Chemistry*, 2:611–665, 2010.

[169] A. Tavernarakis, J. Chaste, A. Eichler, G. Ceballos, M. C. Gordillo, J. Boronat, and A. Bachtold. Atomic Monolayer Deposition on the Surface of Nanotube Mechanical Resonators. *Physical Review Letters*, 112(19):196103, 2014.

[170] S. Gigan, H. R. Bohm, M. Paternostro, F. Blaser, G. Langer, J. B. Hertzberg, K. C. Schwab, D. Bauerle, M. Aspelmeyer, and A. Zeilinger. Self-cooling of a micromirror by radiation pressure. *Nature*, 444(7115):67–70, 2006.

[171] S. M. Meenehan, J. D. Cohen, S. Gröblacher, J. T. Hill, A. H. Safavi-Naeini, M. Aspelmeyer, and O. Painter. Silicon optomechanical crystal resonator at millikelvin temperatures. *Physical Review A*, 90(1):11803, 2014.

[172] Y. Zhang, J. Moser, J. Güttinger, A. Bachtold, and M. I. Dykman. Interplay of Driving and Frequency Noise in the Spectra of Vibrational Systems. *Physical Review Letters*, 113(25):255502, 2014.

[173] J. Moser, A. Verdaguer, D. Jiménez, A. Barreiro, and A. Bachtold. The environment of graphene probed by electrostatic force microscopy. *Applied Physics Letters*, 92(12), 2008.

[174] R. M. Cole, G. A. Brawley, V. P. Adiga, R. De Alba, J. M. Parpia, B. Ilic, H. G. Craighead, and W. P. Bowen. Evanescent-Field Optical Readout of Graphene Mechanical Motion at Room Temperature. *Physical Review Applied*, 3(2):24004, feb 2015.

[175] M. Dykman, editor. *Fluctuating Nonlinear Oscillators*. Oxford, 2012.

[176] K. C. Fong, E. E. Wollman, H. Ravi, W. Chen, A. A. Clerk, M. D. Shaw, H. G. Leduc, and K. C. Schwab. Measurement of the Electronic Thermal Conductance Channels and Heat Capacity of Graphene at Low Temperature. *Physical Review X*, 3(4):41008, 2013.

[177] N. Samkharadze, A. Bruno, P. Scarlino, G. Zheng, D. P. DiVincenzo, L. DiCarlo, and L. M. K. Vandersypen. High-Kinetic-Inductance Superconducting Nanowire Resonators for Circuit QED in a Magnetic Field. *Physical Review Applied*, 5(4):044004, 2016.

[178] A. Cleland. *Foundations of Nanomechanics - From Solid-State Theory to Device Applications*. Springer, 2003.

[179] M. I. Dykman and M. Krivoglaz. Theory of nonlinear oscillator interacting with a medium. *Soviet Scientific Reviews, Section A, Physics Reviews*, 5(265), 1984.

[180] M. Sansa, E. Sage, E. C. Bullard, M. Gély, T. Alava, E. Colinet, A. K. Naik, Luis Guillermo Villanueva, Laurent Duraffourg, Michael L. Roukes, Guillaume Jourdan, and Sébastien Hentz. Frequency fluctuations in silicon nanoresonators. *Nature Nanotechnology*, 11:552–558, 2016.

[181] M. I. Dykman and M. A. Krivoglaz. Classical theory of nonlinear oscillators interacting with a medium. *Physica Status Solidi (B)*, 48:497–512, 1971.

[182] A. W. Barnard, V. Sazonova, A. M. van der Zande, and P. L. McEuen. Fluctuation broadening in carbon nanotube resonators. *Proceedings of the National Academy of Sciences of the United States of America*, 109(47):19093–6, 2012.

[183] Ben H Schneider, Vibhor Singh, Warner J Venstra, Harold B Meerwaldt, and Gary A Steele. Observation of decoherence in a carbon nanotube mechanical resonator. *Nature Commun*, 5:5819, 2014.

[184] C. Eichler, Y. Salathe, J. Mlynek, S. Schmidt, and A. Wallraff. Quantum-Limited Amplification and Entanglement in Coupled Nonlinear Resonators. *Physical Reviev Letters*, 113(11):110502, 2014.

[185] R. N. Kleiman, G. Agnolet, and D. J. Bishop. Two-level systems observed in the mechanical properties of single-crystal silicon at low temperatures. *Physical Review Letters*, 59(18):2079–2082, 1987.

[186] R. Rivière, S. Deléglise, S. Weis, E. Gavartin, O. Arcizet, A. Schliesser, and T. J. Kippenberg. Optomechanical sideband cooling of a micromechanical oscillator close to the quantum ground state. *Physical Review A*, 83(6):063835, 2011.

[187] K. J. Lulla, M. Defoort, C. Blanc, O. Bourgeois, and E. Collin. Evidence for the Role of Normal-State Electrons in Nanoelectromechanical Damping Mechanisms at Very Low Temperatures. *Physical Review Letters*, 110(17):177206, 2013.

[188] R. S. Gonnelli, F. Paolucci, E. Piatti, K. Sharda, A. Sola, M. Tortello, J. R. Nair, C. Gerbaldi, M. Bruna, and S. Borini. Temperature Dependence of Electric Transport in Few-layer Graphene under Large Charge Doping Induced by Electrochemical Gating. *Scientific Reports*, 5:9554, 2015.

[189] M. Imboden, O. A. Williams, and P. Mohanty. Observation of Nonlinear Dissipation in Piezoresistive Diamond Nanomechanical Resonators by Heterodyne Down-Mixing. *Nano Letters*, 13(9):4014–4019, 2013.

[190] I. Mahboob, N. Perrissin, K. Nishiguchi, D. Hatanaka, Y. Okazaki, A. Fujiwara, and H. Yamaguchi. Dispersive and Dissipative Coupling in a Micromechanical Resonator Embedded with a Nanomechanical Resonator. *Nano Letters*, 15(4):2312–2317, 2015.

[191] A. Croy, D. Midtvedt, A. Isacsson, and J. M. Kinaret. Nonlinear Damping in Graphene Resonators. *Physical Review B*, 86:235435, 2012.

[192] D. Antonio, D. H. Zanette, and D. Lopez. Frequency stabilization in nonlinear micromechanical oscillators. *Nature Communications*, 3:806, 2012.

[193] J. Güttinger, A. Noury, P. Weber, A. Eriksson, C. Lagoin, J. Moser, C. Eichler, A. Wallraff, A. Isacsson, and A. Bachtold. Switching off energy decay channels in nanomechanical resonators. *To be published*, 2016.

[194] T. Faust, J. Rieger, M. J. Seitner, J. P. Kotthaus, and E. M. Weig. Coherent control of a classical nanomechanical two-level system. *Nature Physics*, 9(8):485–488, 2013.

[195] H. Okamoto, A. Gourgout, C. Y. Chang, K. Onomitsu, I. Mahboob, E. Y. Chang, and H. Yamaguchi. Coherent phonon manipulation in coupled mechanical resonators. *Nature Physics*, 9(8):480–484, 2013.

[196] S. M. Meenehan, J. D. Cohen, G. S. MacCabe, F. Marsili, M. D. Shaw, and O. Painter. Pulsed Excitation Dynamics of an Optomechanical Crystal Resonator near Its Quantum Ground State of Motion. *Physical Review X*, 5(4):041002, 2015.

[197] Y. Cao, A. Mishchenko, G. L. Yu, E. Khestanova, A. P. Rooney, E. Prestat, A. V. Kretinin, P. Blake, M. B. Shalom, C. Woods, J. Chapman, G. Balakrishnan, I. V. Grigorieva, K. S. Novoselov, B. A. Piot, M. Potemski, K. Watanabe, T. Taniguchi, S. J. Haigh, A. K. Geim, and R. V. Gorbachev. Quality Heterostructures from Two-Dimensional Crystals Unstable in Air by Their Assembly in Inert Atmosphere. *Nano Letters*, 15(8):4914–4921, 2015.

[198] X. Xi, L. Zhao, Z. Wang, H. Berger, L. Forró, J. Shan, and K. F. Mak. Strongly enhanced charge-density-wave order in monolayer NbSe2. *Nature Nanotechnology*, 10(9):765–769, 2015.